



저작자표시-비영리-변경금지 2.0 대한민국

이용자는 아래의 조건을 따르는 경우에 한하여 자유롭게

- 이 저작물을 복제, 배포, 전송, 전시, 공연 및 방송할 수 있습니다.

다음과 같은 조건을 따라야 합니다:



저작자표시. 귀하는 원저작자를 표시하여야 합니다.



비영리. 귀하는 이 저작물을 영리 목적으로 이용할 수 없습니다.



변경금지. 귀하는 이 저작물을 개작, 변형 또는 가공할 수 없습니다.

- 귀하는, 이 저작물의 재이용이나 배포의 경우, 이 저작물에 적용된 이용허락조건을 명확하게 나타내어야 합니다.
- 저작권자로부터 별도의 허가를 받으면 이러한 조건들은 적용되지 않습니다.

저작권법에 따른 이용자의 권리는 위의 내용에 의하여 영향을 받지 않습니다.

이것은 [이용허락규약\(Legal Code\)](#)을 이해하기 쉽게 요약한 것입니다.

[Disclaimer](#)

이학박사학위논문

한반도에서 발생한 집중호우 모의를 위한
수반모형 기반의 레이더 자료 동화

Radar Data Assimilation for the Simulation of
Heavy Rainfall Cases over the Korean
Peninsula Using Adjoint-based Methods

2013년 2월

서울대학교 대학원

지구환경과학부

최 용 한

한반도에서 발생한 집중호우 모의를 위한 수반모형 기반의 레이더 자료 동화

Radar Data Assimilation for the Simulation of
Heavy Rainfall Cases over the
Korean Peninsula Using Adjoint-based Methods

지도교수 임 규 호

이 논문을 이학박사 학위논문으로 제출함
2012년 10월

서울대학교 대학원

지구환경과학부

최 용 한

최용한의 박사학위논문을 인준함
2012년 12월

위 원 장 _____ ①

부위원장 _____ ①

위 원 _____ ①

위 원 _____ ①

위 원 _____ ①

Abstract

Radar Data Assimilation for the Simulation of Heavy Rainfall Cases over the Korean Peninsula Using Adjoint-based Methods

Yonghan Choi

School of Earth and Environmental Sciences

The Graduate School

Seoul National University

In the first part of this study, I selected a heavy rainfall case over the Korean Peninsula, which was characterized by two localized rainfall maxima. This rainfall was caused by an air-mass thunderstorm related to surface heating. The atmosphere over the southwestern and east coast of the Korean Peninsula was convectively unstable with a large Convective Available Potential Energy

(CAPE) value, and lower-level convergence acted as a lifting forcing. Neither of two maxima is simulated accurately when no radar data are assimilated, or when radar data are assimilated using the Three Dimensional Variational (3D-Var) method. Using the Four Dimensional Variational (4D-Var) method partially improves the simulated rainfall over the southwestern part of the Korean Peninsula. In order to obtain further improvements in the rainfall forecast, outer loops and the Quasi Static Variational Assimilation (QSVA) method are used. In the QSVA method, the length of the assimilation window is increased gradually, and the starting point of the current minimization task comes from the minimizer of the previous minimization task.

The minimization of the cost function in the 4DVAR, OUTER, and QSVA experiments converges successfully after several iterations. The ending value of the cost function and Root Mean Square Error (RMSE) of O-A (observation minus analysis) for the OUTER and QSVA experiments are smaller than those for the 4DVAR experiment. This implies that the analysis of the OUTER and QSVA experiments is better than (i.e., closer to the observations) the 4DVAR experiment. RMSE of O-B (observation minus background) and RMSD of analysis increment (analysis minus background) for the OUTER and QSVA experiments are less than those for the 4DVAR experiment. Therefore, the

improved analysis of the OUTER and QSVA experiments is owing to a better background estimate (or first guess) of those experiments. Furthermore, more observations (maybe, critical in improving the rainfall forecast) get into the assimilation in the OUTER and QSVA experiments by reducing innovation (O-B) value.

The gap between nonlinear and linear growth (or the nonlinearity of the original minimization problem) is reduced in the OUTER and QSVA experiments compared to the 4DVAR experiment. This is because the background estimate and nonlinear model trajectory are progressively updated in those experiments. It should be also noted that the nonlinearity of the nonlinear minimization problem is increased with increasing length of the assimilation window in the minimization tasks of the QSVA experiment.

Incremental wind in the 4DVAR (or OUTER) experiment is cyclonic and convergent over the southwestern part of the Korean Peninsula, and this modification leads to an improved rainfall forecast in the 4DVAR (or OUTER) experiment compared to the CONTROL or 3DVAR experiment. However, the simulated rainfall amount over the southwestern part of the Korean Peninsula is overestimated, and the rainfall distribution wrongly extends to the central part of South Korea in the 4DVAR (or OUTER) experiment. In the QSVA

experiment, the analysis increment of CAPE is negative over the western part of the Korean Peninsula, which results in a better rainfall forecast than in the 4DVAR or OUTER experiment. The nonlinearity of the original minimization problem is increased gradually with increasing length of the assimilation window in the QSVA experiment. This quasi-static adjustment guarantees that the computed minimum at the current minimization is the global minimum and the starting point for the next minimization lies within the basin of the global minimum. Computational cost of the QSVA method is much cheaper than that of using multiple outer loops, and it can be reduced further via the use of a loose stopping criterion for the inner-loop minimization.

The conclusion from one heavy rainfall case is convinced by analyzing additional heavy rainfall cases over the Korean Peninsula. Quality of the analysis (and background estimate) can be improved through the use of the multiple outer-loops or QSVA method compared to the 4D-Var method. Especially, the QSVA method is more effective than the outer-loop method when the nonlinearity of the original minimization problem is relatively high. It is expected that the QSVA method will be more useful when the length of the assimilation window is increased, or when horizontal resolution is enhanced, which is usually related to the high degree of nonlinearity.

In the second part of this study, I selected a heavy rainfall case over the Korean Peninsula, which occurred on 1800 UTC 26 July 2006. This case caused torrential rainfall over the central part of the Korean Peninsula. Synoptic environments related to the case were favorable for the development of Mesoscale Convective Systems (MCSs). The MCS related to the heavy rainfall can be classified as Training Line/Adjoining Stratiform (TL/AS)-type for the period of 1800 UTC 26 to 0600 UTC 27 July 2006 and Back Building (BB)-type for the period after 0600 UTC 27 July 2006 based on the morphological analyses of radar reflectivity. Prolonged heavy convective rainfall was observed along the surface boundary, which was defined by large Equivalent Potential Temperature (EPT) gradient, and stratiform rainfall was adjacent to the convective rainfall during the TL/AS-type period. The Mesoscale Convective Vortex (MCV) induced by prior convective rainfall interacted with vertical wind shear, and this interaction destabilized the atmosphere by lifting conditionally-unstable air to its saturation level during the BB-type period.

The Adjoint Sensitivity-based Data Assimilation (ASDA) method is proposed to evade high computational cost of the 4D-Var method, retaining the advantages of the 4D-Var method. In the ASDA method, an adjoint model is run backwards with forecast-error gradient as an input, and adjoint sensitivity of

forecast error to initial condition is scaled by an optimal scaling factor. The optimal scaling factor is determined by minimizing observational cost function of the 4D-Var method, and the scaled sensitivity is added to the original first guess (or background estimate). Finally, the observations at the analysis time are assimilated using the 3D-Var method with the improved first guess.

The simulated rainfall distribution is shifted northeastward compared to the observations when no radar data are assimilated, or when radar data are assimilated using the 3D-Var method. The rainfall distribution and time series of hourly rainfall are improved through the 4D-Var method or ASDA method. In addition, simulated meteorological fields such as zonal wind, meridional wind, temperature, and water vapor mixing ratio are closer to the observations when the 4D-Var or ASDA method is used, based on the analyses of verification results.

Negative increments of EPT, especially of water vapor mixing ratio, over the Yellow Sea enhance meridional gradient of EPT (i.e., baroclinic instability) in the 4DVAR and ASDA experiments, and simultaneously, this corrects the location of the surface boundary related to TL/AS-type MCS development. Due to the improvement of the analysis, subsequent forecasts appropriately simulate the observed features of TL/AS-and BB-type MCSs and the corresponding

rainfall in the 4DVAR and ASDA experiments. In CONTROL experiment, simulated rainfall related to TL/AS-type MCS is displaced northeastward compared to the observations. The interaction between MCV associated with prior rainfall and vertical wind shear occurs over the northern part of the Korean Peninsula, where transport of warm and moist air is not active. Therefore, rainfall related to BB-type MCS is not simulated well in the CONTROL experiment. However, in the 4DVAR and ASDA experiments, rainfall related to TL/AS-type MCS is properly simulated, and finally, rainfall related to BB-type MCS is also simulated well. It should be also noted that computational cost of the ASDA method is relatively low (not related to iterative minimization of cost function; one adjoint-model run, two 3D-Var analyses, scaling-factor determination) compared to the 4DVAR method, and the first-guess and observations errors are not correlated with each other.

Key words: Radar data assimilation, Heavy rainfall, 4D-Var, QSVa method, Adjoint sensitivity, ASDA method

Student Number: 2006-30788

Contents

Chapter 1. Introduction	1
1.1. General aspects.....	1
1.2. Review of previous studies	6
1.2.1. An alternative implementation method for 4D-Var	6
1.2.2. Adjoint sensitivity as a means of improving initial condition	9
1.3. Objectives of this study	14
Chapter 2. Algorithms	17
2.1. The Quasi Static Variational Assimilation (QSVA) algorithm	17
2.2. The Adjoint Sensitivity-based Data Assimilation (ASDA) algorithm	21
Chapter 3. Numerical model, data assimilation system, and radar data	31
3.1. The Weather Research and Forecasting (WRF) model	31
3.2. The WRF Data Assimilation (WRFDA) system	33
3.3. Radar data.....	35
Chapter 4. The QSVA method and its comparison to outer-loop method.....	37
4.1. Case description	37
4.2. Experimental design.....	45
4.3. Results and discussion.....	50

4.4. Extension to heavy rainfall cases in 2006 and 2008	88
Chapter 5. The ASDA method and its comparison to variational methods	117
5.1. Case description	117
5.2. Experimental design	130
5.3. Results and discussion.....	135
Chapter 6. Summary and conclusion	168
References.....	177
국문 초록.....	190

List of Tables

Table 4.1. Convective Available Potential Energy (CAPE, J kg ⁻¹), Convective Inhibition (CIN, J kg ⁻¹), Lifting Condensation Level (LCL, m), and Level of Free Convection (LFC, m) computed from sounding observations of Gwangju at 0000 UTC and 0600 UTC 6 August 2006.	43
Table 4.2. Brief description for each numerical experiment.....	48
Table 4.3. Root Mean Square Errors (RMSEs, m s ⁻¹) of O-B and O-A for radar radial velocity and the number of assimilated observations for the 3DVAR, 4DVAR, OUTER, and QSVA experiments. The number in parenthesis in the OUTER experiment means the number of outer loops applied and that in the QSVA experiment means the length of the assimilation window (in minute) for each assimilation task.	58
Table 4.4. Summary of heavy rainfall cases in 2006 and 2008.	94
Table 4.5. Percentage error in linearization (%) at the end of an assimilation window for 4DVAR, OUTER, and QSVA experiments.	116
Table 5.1. Brief descriptions of numerical experiments.	134

List of Figures

- Figure 4.1. (a) Observed 6-h accumulated rainfall ($\text{mm } 6\text{h}^{-1}$) distribution over South Korea from 0600 UTC to 1200 UTC 6 August 2006. Time series of hourly rainfall (mm h^{-1}) from 0600 UTC to 1200 UTC 6 August 2006 for the observations (black), CONTROL (blue), 3DVAR (yellow), 4DVAR (green), QSVa (orange), and OUTER (red) experiments at (b) Namwon and (c) Taebaek. In the case of numerical experiments, hourly rainfalls at the grid points corresponding to Namwon and Taebaek are shown.41
- Figure 4.2. (a) Skew T-log p diagram computed from radiosonde observations of Gwangju at 0000 UTC (blue) and 0600 UTC (red) 6 August 2006. (b) Vertical profile of potential temperature (K, solid line) and equivalent potential temperature (K, dashed line) for Gwangju at 0000 UTC (blue) and 0600 UTC (red) 6 August 2006.42
- Figure 4.3. Radar analyses near Namwon area at 0900 UTC 6 August 2006. (a) Horizontal distribution of divergence (10^{-4} s^{-1} , shading) and winds (m s^{-1} , vector) at 4-km height. (b) Vertical cross section along the line shown in (a) of vertical wind (m s^{-1} , shading) and divergence (10^{-4} s^{-1} , negative values are denoted by dashed contours).44
- Figure 4.4. Domain configuration. (a) Geographical area for domains 1, 2, and 3 and (b) model terrain height (m) for domain 3. Locations of Namwon, Taebaek, and Gwangju cities are also indicated.49
- Figure 4.5. Cost-function values as a function of iteration number for the (a) 3DVAR, (b) 4DVAR, and (c) OUTER experiments. In the OUTER experiment, a total of 4 outer loops are used, and cost-function values for the first- (blue), second- (green), third- (orange), and fourth-outer-loop (red) are shown. Maximum and minimum values of cost function are indicated

at the maximum/minimum points of each curve.....	56
Figure 4.6. Cost-function values as a function of iteration number for assimilation tasks of the QSVA experiment with assimilation window of (a) 0 minute, (b) 10 minutes, (c) 20 minutes, and (d) 30 minutes. Maximum and minimum values of cost function are indicated at the maximum/minimum points of each curve.	57
Figure 4.7. Vertical distribution of RMSD of analysis increment for the 4DVAR (green), QSVA (orange), and OUTER (red) experiments. (a) Zonal wind (m s^{-1}) and (b) meridional wind (m s^{-1}). For the QSVA experiment, original first guess (solid) and updated first guesses from analysis of assimilation task with 0-min (dashed), 10-min (dotted), and 20-min (dash-dotted) assimilation window are used in calculating analysis increment. Likewise, for the OUTER experiment, original first guess (solid) and updated first guesses from analysis of the first (dashed) and second (dotted) outer loop are used.	59
Figure 4.8. (a) Percentage error in linearization (%) and (b) pattern correlation as a function of forecast length for the 4DVAR (green solid line), QSVA_10 (orange dotted line), QSVA_20 (orange dashed line), QSVA_30 (orange solid line), and OUTER (red solid line) experiments.	68
Figure 4.9. Computing time (hour) for the 4DVAR, OUTER, QSVA, and QSVA_LC experiments. In the OUTER experiment, computing times for the first, second, and third outer loop are shown. In the QSVA and QSVA_LC experiments, computing times for assimilation tasks with assimilation window of 10, 20, and 30 minutes are shown. Note that computing time for assimilation task with assimilation window of 0 minute is less than one minute.	69
Figure 4.10. 6-h accumulated rainfall (mm 6h^{-1}) distribution over South Korea from 0600 UTC to 1200 UTC 6 August 2006 for the (a) observations, (b) CONTROL, (c) 3DVAR, (d) 4DVAR, (e) QSVA, and (f) OUTER experiments. Note that different color scales are used for the QSVA and	

OUTER experiments.....	81
Figure 4.11. Root Mean Square Errors (RMSEs) of rainfall ($\text{mm } 6\text{h}^{-1}$) as a function of forecast time for the CONTROL (blue), 3DVAR (yellow), 4DVAR (green), QSVa (orange), and OUTER (red) experiments. Surface observations from 76 observation sites over South Korea are used.	82
Figure 4.12. Root Mean Square Errors (RMSEs) of radial velocity (m s^{-1}) as a function of forecast time for the CONTROL (blue), 3DVAR (yellow), 4DVAR (green), QSVa (orange), and OUTER (red) experiments. Radial velocity observations from 13 radar observation sites over the Korean Peninsula are used.	83
Figure 4.13. Vertical distribution of fit to the observations using sounding observations over the Korean Peninsula at 1200 UTC 6 August 2006 for the CONTROL (blue), 3DVAR (yellow), 4DVAR (green), QSVa (orange), and OUTER (red) experiments. (a) Zonal wind (m s^{-1}), (b) meridional wind (m s^{-1}), (c) temperature (K), and (d) water vapor mixing ratio (kg kg^{-1}).....	84
Figure 4.14. (a) Convective Available Potential Energy (CAPE, J kg^{-1} , shading), divergence (10^{-5} s^{-1} , negative values are denoted by dashed contours), and winds (m s^{-1} , vector) of 850 hPa at 0600 UTC 6 August 2006 for the CONTROL experiment. Analysis increments of CAPE (J kg^{-1} , shading), divergence (10^{-5} s^{-1} , negative values are denoted by dashed contours), and winds (m s^{-1} , vector) at 850 hPa for the (b) 4DVAR and (c) QSVa experiments.	85
Figure 4.15. Vertical cross section along the line in Fig. 4.10d of (a) vertical wind (m s^{-1} , shading) and divergence (10^{-4} s^{-1} , negative values are denoted by dashed contours) and (b) reflectivity (dBZ, shading) and equivalent potential temperature (K, contour interval of 5 K) at 0900 UTC 6 August 2006. (c) Skew T-log p diagram of Gwangju for the QSVa experiment at 0900 UTC 6 August 2006.	86

Figure 4.16. Observed 24-h accumulated rainfall distribution ($\text{mm } 24\text{h}^{-1}$) for (a) Case 1, (b) Case 2, (c) Case 3, and (d) Case 5.	95
Figure 4.17. Observed 24-h accumulated rainfall distribution ($\text{mm } 24\text{h}^{-1}$) for (a) Case 6, (b) Case 7, (c) Case 8, (d) Case 9, and (e) Case 10.	97
Figure 4.18. Normalized cost function as a function of iteration number for Case 1 (blue), Case 2 (green), Case 3 (orange), Case 4 (yellow), and Case 5 (red). (a) 4DVAR, (b) OUTER, and (c) QSVA experiments.	98
Figure 4.19. Same as Figure 4.18 but for Case 6 (blue), Case 7 (green), Case 8 (orange), Case 9 (yellow), and Case 10 (red).	99
Figure 4.20. RMSEs of O-B and O-A for radial velocity (m s^{-1}) computed from 4DVAR (green), OUTER (red), and QSVA (orange) experiments. Results for (a) Case 1, (b) Case 2, (c) Case 3, (d) Case 4, and (e) Case 5 are shown. In case of OUTER experiment, results for the second and third outer loops are shown, and in case of QSVA experiment, results for assimilation window of 0, 10, 20, and 30 minutes are shown. (f) The number of total assimilated observations in 4DVAR (green), OUTER (red), and QSVA (orange) experiments.	104
Figure 4.21. Same as Figure 4.20 but for Cases 6, 7, 8, 9, and 10.	106
Figure 4.22. Computing time (hour) on Linux cluster with 24 CPUs for 4DVAR (green), OUTER (red), and QSVA (orange) experiments. (a) Cases 1-5 and (b) cases 6-10. The number of total iterations for each experiment is indicated.	107
Figure 4.23. (a) Threat score and (b) bias score of 24-h (or 6-h) accumulated rainfall for threshold value of 20 mm in CONTROL (blue), 4DVAR (green), OUTER (red), and QSVA (orange) experiments. Results for Cases 1, 2, 3, 4, and 5 are shown.	113
Figure 4.24. Same as Figure 4.23 but for Cases 6, 7, 8, 9, and 10.	114
Figure 4.25. RMSE of radial velocity (m s^{-1}) for CONTROL (blue), 4DVAR	

(green), OUTER (red), and QSVa (orange) experiments. (a) Cases 1-5 and (b) cases 6-10. RMSEs of radial velocity during 24-h (or 6-h) forecast are averaged.	115
Figure 5.1. Observed 18-h accumulated rainfall ($\text{mm } 18\text{h}^{-1}$) distribution from 1800 UTC 26 to 1200 UTC 27 July 2006.	120
Figure 5.2. Synoptic environments at 0000 UTC 27 July 2006. (a) geopotential height (black solid, contour interval of 30 m), temperature (red dashed, contour interval of 3°C), water vapor mixing ratio (shaded, greater than 0.012 kg kg^{-1}), and wind vector (knot) at 850 hPa, (b) geopotential height (black solid, contour interval of 30 m), wind speed (red solid, contour interval of 5 knots), and divergence (shaded, 10^{-5} s^{-1} , only negative values are plotted) at 850 hPa, (c) geopotential height (black solid, contour interval of 60 m), temperature (red dashed, contour interval of 5°C), relative vorticity (shaded, 10^{-5} s^{-1} , only positive values are plotted), and wind vector (knot) at 500 hPa, (d) geopotential height (black solid, contour interval of 120 m), wind speed (green solid, contour interval of 25 knots), and divergence (shaded, 10^{-5} s^{-1} , only positive values are plotted) at 200 hPa.	121
Figure 5.3. Observed radar reflectivities (dBZ) at 4-km height from 1900 UTC 26 to 1200 UTC 27 July 2006 with an interval of one hour.	123
Figure 5.4. Horizontal distribution of 850-hPa equivalent potential temperature (shaded, K) and vertical wind shear vector (knot hPa^{-1}) between (a) surface and 925 hPa and (b) 925 hPa and 500 hPa at 1800 UTC 26 July 2006. ..	127
Figure 5.5. (a) Hodograph and (b) skew T-log p diagram of Osan at 0600 UTC 27 July 2006.	128
Figure 5.6. Surface analyses of (a) relative humidity (black solid, contour interval of 5%) and wind vector (m s^{-1}), and (b) pressure (black solid, contour interval of 1 hPa) and temperature (red dashed, contour interval of 2°C) at 0600 UTC 27 July 2006.	129

Figure 5.7. (a) Geographical areas of domains 1, 2, and 3 and (b) locations of radar observation sites operated by Korea Meteorological Administration (black), Korea Air Force (red), and United States of America Air Force (blue). Locations of Automatic Weather Station observation sites over South Korea are also indicated with crosses.	133
Figure 5.8. 18-h accumulated rainfall ($\text{mm } 18\text{h}^{-1}$) distributions from 1800 UTC 26 to 1200 UTC 27 July 2006 for (a) CONTROL, (b) 3DVAR, (c) 4DVAR, and (d) ASDA experiments.	142
Figure 5.9. Time series of hourly rainfall amount (mm h^{-1}) at (a) Seoul and (b) Hongcheon (or the corresponding grid points in case of model experiment) for the observations (black), CONTROL (blue), 3DVAR (green), 4DVAR (yellow), and ASDA (red) experiments. Maximum hourly rainfall amount is also indicated.	143
Figure 5.10. Quantitative precipitation forecast skill of CONTROL (blue), 3DVAR (green), 4DVAR (yellow), and ASDA (red) experiments for threshold values of 5, 10, 25, and 50 mm. (a) Threat score and (b) bias score.	144
Figure 5.11. Root Mean Square Errors (RMSEs) of rainfall ($\text{mm } 6\text{h}^{-1}$ or $\text{mm } 18\text{h}^{-1}$) as a function of forecast time for CONTROL (blue), 3DVAR (green), 4DVAR (yellow), and ASDA (red) experiments.	145
Figure 5.12. Root Mean Square Differences (RMSDs) against FNL data of (a) zonal wind (m s^{-1}), (b) meridional wind (m s^{-1}), (c) temperature (K), and (d) water vapor mixing ratio (kg kg^{-1}) as a function of forecast length for CONTROL (blue), 3DVAR (green), 4DVAR (yellow), and ASDA (red) experiments.	150
Figure 5.13. Vertical distributions of fit to the observations using sounding observations over South Korea at 0000 UTC 27 July 2006 for CONTROL (blue), 3DVAR (green), 4DVAR (yellow), and ASDA (red) experiments. (a) Zonal wind (m s^{-1}), (b) meridional wind (m s^{-1}), (c) temperature (K), and (d)	

water vapor mixing ratio (kg kg^{-1}).	151
Figure 5.14. RMSEs of radial velocity (m s^{-1}) as a function of forecast length for CONTROL (blue), 3DVAR (green), 4DVAR (yellow), and ASDA (red) experiments. Radar radial velocity data from 14 radar observation sites over the Korean Peninsula are used.	152
Figure 5.15. Horizontal distributions of 850-hPa equivalent potential temperature (contour interval of 4 K) at 1800 UTC 26 July 2006 for (a) CONTROL, (b) 4DVAR, and (c) ASDA experiments. In case of data assimilation experiments, analysis increments of equivalent potential temperature (shaded, K) are also shown.	156
Figure 5.16. 850-hPa analysis increment of wind vector and speed (shaded, m s^{-1}) for (a) 4DVAR and (b) ASDA experiments.....	157
Figure 5.17. Horizontal distributions of Sea Level Pressure (SLP, contour interval of 1 hPa) at 1800 UTC 26 July 2006 for (a) CONTROL, (b) 4DVAR, and (c) ASDA experiments. In case of data assimilation experiments, analysis increments of SLP (shaded, hPa) are superimposed on the corresponding analysis fields.	158
Figure 5.18. Radar reflectivities (dBZ) of 4-km height from 0300 UTC to 1200 UTC 27 July 2006 with 3-hour interval for CONTROL (top), 4DVAR (middle), and ASDA (bottom) experiments.	164
Figure 5.19. Horizontal distributions of 500-hPa absolute vorticity (shaded, 10^{-5} s^{-1}) and vertical wind shear vector between 500 hPa and 800 hPa ($\text{m s}^{-1} \text{ hPa}^{-1}$) at 0600 UTC 27 July 2006 for (a) CONTROL, (b) 4DVAR, and (c) ASDA experiments.	165
Figure 5.20. Simulated hodographs of Osan at 0600 UTC 27 July 2006 for (a) 4DVAR and (b) ASDA experiments. Simulated skew T-log p diagrams of Osan at 0600 UTC 27 July 2006 for (c) 4DVAR and (d) ASDA experiments.	166

Figure 5.21. Vertical cross sections of vertical wind (shaded, m s^{-1}) and relative humidity (contour interval of 2.5%) along the line shown in Figs. 5.19b and c at 0600 UTC 27 July 2006 for (a) 4DVAR and (b) ASDA experiments.167

Chapter 1. Introduction

1.1. General aspects

The predictability of Numerical Weather Prediction (NWP) is limited to a finite value due to uncertainties in the initial conditions although the numerical model is perfect. Bjerknes (1904) noted that enough information on the current state of the atmosphere is essential for predicting the future state of the atmosphere using the numerical model in his first attempt of NWP. The initial condition for NWP can be improved through the process called ‘data assimilation’. Talagrand (1997) pointed out that the purpose of data assimilation is using all the available information to determine the current state of the atmospheric flow as accurately as possible. The available information includes the observations, background (usually from short-range forecast), their error statistics, and physical laws which govern the evolution of the flow. Through data assimilation, all the available information is combined in a statistically-optimal way to produce the improved initial condition. In most NWP centers,

data assimilation is used to reduce uncertainties in the initial conditions and to improve the quality of the subsequent forecasts.

Data assimilation methods can be divided into two groups: sequential methods and variational methods. Sequential methods are based on the minimum-variance approach, and examples are the Optimal Interpolation (OI; Gandin, 1963), Extended Kalman Filter (EKF), and Ensemble Kalman Filter (EnKF; Evensen, 1994) methods. Variational methods are based on the maximum-likelihood approach, and examples are the Three Dimensional Variational (3D-Var) and Four Dimensional Variational (4D-Var; Lewis and Derber, 1985; Le Dimet and Talagrand, 1986) methods. The 4D-Var method has been studied extensively over the past two decades, and now it is one of the most sophisticated data assimilation methods. Several operational centers implemented the 4D-Var method in their data assimilation systems, including the European Centre for Medium-Range Weather Forecasts (ECMWF; Rabier et al., 2000), the Met Office (Rawlins et al., 2007), Météo France (Gauthier and Thépaut, 2001), the Japan Meteorological Agency (JMA; Honda et al., 2005), Environment Canada (Gauthier et al., 2007), the High-Resolution Limited-Area Model (HIRLAM; Huang et al., 2002), and the Naval Research Laboratory Atmospheric Variational Data Assimilation System (NAVDAS-AR; Xu et al.,

2005).

The 4D-Var method is superior to its predecessor, the 3D-Var method in the following respects. First, the observations can be assimilated at the time of their measurement, which suits most asynoptic data (e.g., radar observations). Second, flow-dependent background error covariance is used implicitly (static background error covariance in the 3D-Var method), which is of vital importance in fast-developing weather systems. Third, a forecast model is used as a constraint in the 4D-Var method, which enhances dynamic balance of the analysis (Huang et al., 2009). In spite of many advantages of the 4D-Var method, the 4D-Var method has limitations in its operational implementation, namely a huge amount of computational time, due to the iterative nature of its minimization algorithm. Furthermore, it is difficult to develop and maintain tangent linear and adjoint models required for the 4D-Var method, and solution to the minimization problem can be sub-optimal.

In recent decades, assimilation of radar radial velocity/reflectivity data has shown potential for very-short-range numerical prediction of rapidly developing convective systems. Xiao et al. (2005) assimilated radar radial velocity data using the fifth-generation Pennsylvania State University-National Center for Atmospheric Research Mesoscale Model (MM5; Grell et al., 1994) and its 3D-

Var system (Barker et al., 2004). In order to assimilate radial velocity data, vertical velocity increments were included through Richardson's balance equation, and an observation operator for the Doppler radial velocity was developed. Xiao et al. (2007) used the MM5 3D-Var system to assimilate radar reflectivity data. The total water mixing ratio was selected as the control variable for moisture, and the warm-rain process was incorporated into the system to partition the water vapor and the other hydrometeor increments. Moreover, an observation operator for radar reflectivity was developed. The MM5 and its 3D-Var system have been replaced by the Weather Research and Forecasting (WRF) model (Skamarock et al., 2008) and its 3D-Var system. Multiple-Doppler radar data were assimilated using the WRF 3D-Var data assimilation system in order to improve the forecast of the squall-line convective system in Xiao and Sun (2007). More recently, Wang et al. (2013) assimilated radar data into the WRF model using the 4D-Var method in order to improve short-term precipitation prediction. The new development for the WRF 4D-Var radar data assimilation system included the tangent-linear and adjoint models of a Kessler warm rain microphysics scheme and the new control variable of cloud water and rain water.

Park and Županski (2003) reviewed the status and progress of the 4D-Var

method focusing on application to prediction of meso- and storm-scale meteorological phenomena. An overview of controversial issues on meso- and storm-scale 4D-Var, especially radar data assimilation using the 4D-Var method, were presented. They include high-resolution observations, nonlinearity and discontinuity problem, model error, treatment of lateral boundary condition, and precipitation assimilation. Additionally, practical strategies for implementation of the 4D-Var method were introduced. Examples are incremental 4D-Var, poor man's 4D-Var, inverse 3D-Var, and hybrid approach. Sun (2005) reviewed techniques used in convective-scale radar data assimilation such as successive correction, nudging, 3D-Var, 4D-Var, and ensemble Kalman filter. She also mentioned the recent progresses in convective-scale radar data assimilation such as estimation of observation error, quality control/pre-processing of radar data, and development of observation operator. Finally, future challenges in convective-scale data assimilation were discussed. Especially, the operational implementation of the 4D-Var method at high resolution poses a number of challenges such as computational resources and nonlinearity. In this study, of a number of issues on radar data assimilation using the 4D-Var, issues related to the nonlinearity of the minimization problem and computational cost will be discussed.

1.2. Review of previous studies

1.2.1. An alternative implementation method for 4D-Var

In the 4D-Var method, an analysis is obtained by minimizing a cost function that measures the sum of distances between the observations and the solution of the model during an assimilation window, and between the background and the solution at the beginning of the assimilation window. Generally, the 4D-Var is implemented using an incremental formulation, which approximates the minimization of the nonlinear cost function by a sequence of minimizations of linear least-squares cost functions (Courtier et al., 1994; Haben et al., 2011). The incremental formulation has the advantage of allowing further approximations in the solution procedure, such as lower-resolution inner loop and simplified tangent linear and adjoint models, to make the minimization problem computationally feasible. An iterative method such as the conjugate gradient or quasi Newton technique is used to solve each linearized minimization problem.

In the incremental formulation, the linearized cost function is minimized in an inner loop, and the nonlinear model trajectory (or basic state), which is for linearization of the nonlinear model and observation operator, and background estimate (or first guess) are updated in an outer loop. Nonlinearities related to the model and the observation operator can be taken into account in the outer loop because the nonlinear model trajectory for linearization is consistently updated. The quality of the analysis can be improved and more observations can be utilized by using more-than-one outer loops (Rizvi et al., 2008). Outer loops have been implemented by a number of operational centers such as the ECMWF, Météo-France, the Met Office, and Environment Canada in spite of the increased computational cost.

The cost function may have multiple minima when the original minimization problem involves highly nonlinear processes (Sneider, 1998). The nonlinearity of the original minimization problem increases as the time interval for the minimization increases. Multiple-minima problem related to the lengthening of the assimilation window was studied for the Lorenz model (Stensrud and Bao, 1992; Miller et al., 1994), the model based on a barotropic vorticity equation (Tanguay et al., 1995), and a multilevel general circulation model (Thépaut and Courtier, 1991; Rabier and Courtier, 1992; Li et al., 1994; Rabier et al., 1998).

The nonlinearity of the minimization problem is also dependent on the horizontal resolution of the model (Tanguay et al., 1995) and the atmospheric phenomena considered (Gauthier, 1992).

Pires et al. (1996) investigated how the accuracy of the state obtained at the end of the assimilation window varies when the length of the assimilation window is theoretically increased back to infinity using the three-variable system introduced by Lorenz (1963) under the assumption of a perfect model. In the limit of infinitely long assimilation periods, the chaotic nature of the system produces a number of local (or secondary) minima. The Quasi Static Variational Assimilation (QSVA) algorithm was proposed to determine the global (or absolute) minimum and to avoid getting trapped near a local minimum, which is based on successive small increments of the assimilation window and quasi-static adjustments of the minimizing solution. The algorithm was also applied to a quasi-geostrophic model, and it was effective in solving the minimization problem with the assimilation window of the order of 5-10 days.

The computational cost in the 4D-Var is usually concentrated just after the so-called ‘cut-off-time’, i.e., after the end of the assimilation period. Järvinen et al. (1996) proposed an alternative implementation of the 4D-Var, the quasi-

continuous variational assimilation approach (similar to the QSVa algorithm), to reduce the peak computational requirements of the 4D-Var after the cut-off-time and to accelerate the convergence of the minimization of the cost function. The feasibility of the approach was first validated with a low-resolution barotropic grid-point model using synthetic observations, and the results were then confirmed with a multi-level primitive equation model using real observations. The QSVa algorithm was used by Swanson and Vautard (1998) to study the performance of 4D-Var assimilation of noisy observations in a multi-layer quasi-geostrophic model within both perfect and imperfect model settings. Song et al. (2009) proposed a Retrospective Optimal Interpolation (ROI) system based on the QSVa algorithm, and the QSVa algorithm was also used to fit a nonlinear oceanographic model to altimeter observations for a lengthy assimilation window (Luong et al., 1998).

1.2.2. Adjoint sensitivity as a means of improving initial condition

The sensitivity gradient of 48-h forecast error with respect to the initial condition was calculated by using the adjoint method in Rabier et al. (1996).

The forecast error was defined as the difference between the 48-h forecast and the verifying analysis, which was considered as the truth, and the dry total energy norm was used. This gradient was multiplied by a scaling factor to make a perturbation, and the perturbation was added to the original initial condition. In their study, the scaling factor was derived by trial and error, and the order of magnitude was around 0.01. The forecast starting from the perturbed initial condition, the so-called ‘sensitivity integration’ was more accurate than the original forecast not only in the short-range but also in the medium-range. However, the sensitivity integration was not better than the forecast with the latest initial condition (i.e., two days later than the initial condition for the sensitivity integration or the original forecast). Therefore, the sensitivity integration had limitations in being used in an operational mode, and it was recommended as a diagnostic tool.

The short-range forecast error was minimized by using an iterative procedure, and after some iterations, that procedure led to the so-called ‘key analysis error’ in Klinker et al. (1998). A scaled gradient computed from the first step of the minimization procedure was similar to the sensitivity gradient of Rabier et al. (1996). In a case study, it was shown that the increment after the third iteration was the closest to the key analysis error which, when added to the analysis, both

significantly improved the fit to the observations and substantially improved the subsequent forecast. It was also found that more iterations were not beneficial because of the uncertainty in the definition of the forecast error, and approximations in the tangent-linear and adjoint models. Adjoint sensitivity-based perturbations, such as the sensitivity gradient of Rabier et al. (1996) and the key analysis error of Klinker et al. (1998), minimizing the two-day forecast error were computed in Isaksen et al. (2005). It was found that forecasts starting from the perturbed analyses were further away from the observations than forecasts from control analyses during the first approximately 12 h of forecasts, and this feature was enhanced as the number of iterations increased.

The adjoint sensitivity of short-range forecast error to the initial condition can be used as the perturbation which, when scaled appropriately and added to the original initial condition, improves the subsequent forecast and its consistency. However, the forecast from the perturbed initial condition is not better than the forecast starting from the initial condition at the time of the verifying analysis. In order to overcome these limitations, Huang et al. (1997) proposed the Poorman's variational assimilation (PMV) system. The system was a hybrid one based on both an intermittent data assimilation method, an OI scheme and a variational data assimilation method, a 4D-Var scheme. The main idea of the

PMV is using the adjoint model to produce an improved first guess, which leads to an improved OI analysis. From five-day data assimilation experiments, it was shown that the analysis increments of the PMV were reduced (i.e., closer to the observations) and the subsequent forecasts of the PMV were improved compared to the OI. However, the PMV violates the basic assumption, that the first-guess error and the observational error should be uncorrelated, although the orthogonality between the barotropic OI analysis and the baroclinic PMV analysis alleviates the problem related to the violation. In Huang (1999), a generalized version of the PMV (GPV), which had implementation flexibility due to its incremental nature, was proposed. Running the variational component on lower resolutions and with a different model formulation did not alter the conclusion of Huang et al. (1997). In other words, the GPV led to smaller analysis increments, modified baroclinic structures at upper levels, and improved forecasts. Pu et al. (1997) proposed an ‘iterated cycle’ technique, in which the perturbed one- or two-day old analysis was used as an improved starting point for a repetition of the regular analysis cycle until the current analysis time was reached. This technique improved the future forecast skill, but it had the same problem as that of the GPV (or PMV).

Hello et al. (2000) proposed an analysis correction method in which the

perturbation to the original analysis came from the adjoint sensitivity to the initial condition, and its sign and magnitude were determined by minimizing the distance to the available observations at the locations where the sensitivity was of significance. In their approach, the response (or objective) function was the mean sea-level pressure, and hence the verifying analysis acting as the truth was not necessary. However, if the forecast from the original analysis are far away from the truth, it is difficult to expect a significant improvement of the analysis.

Kalnay et al. (2000) proposed an alternative data assimilation method using the quasi-inverse model, the inverse 3D-Var (I3D-Var) method. The quasi-inverse model is simply the model integrated backward but changing the sign of dissipative terms in order to avoid computational blow-up. In the I3D-Var method, the background term is estimated at the end of the assimilation window, and multiple time-level data can be assimilated by averaging increments corresponding to the different time-levels. The I3D-Var does not need to compute the Hessian or gradient, and hence computational cost is significantly reduced compared to the 4D-Var. However, in general, dynamics and physics of a model may not be written in a reversible fashion. Park and Kalnay (2004) suggested the I3D-Var as a preconditioner for carrying out minimization in the

4D-Var framework. By using the initial conditions (a kind of first guess) obtained through the I3D-Var, the minimization of the 4D-Var cost function was converged much faster.

1.3. Objectives of this study

Radar radial velocity data are assimilated for a heavy rainfall case over the Korean Peninsula, which occurred on 6 August 2006, by using the Weather Research and Forecasting Data Assimilation (WRFDA) system (Huang et al., 2009). The WRFDA system includes 3D-Var and 4D-Var capabilities, and outer loop can be used within the 4D-Var capability. The QSVA algorithm is implemented to the WRF 4D-Var, and it is compared with single outer-loop 4D-Var (i.e., normal 4D-Var) and multiple outer-loop 4D-Var. Despite the usefulness of the outer loop, there have been few studies on its effect on the analysis and subsequent forecast. The QSVA algorithm is known to be effective in finding optimal solution to minimization problem when the nonlinearity of the minimization problem is high. The first objective of this study is to compare the QSVA method with the 4D-Var and outer-loop methods, focusing on the

quality of the first guess (or background estimate) and the nonlinearity of the minimization problem. In addition, a strategy for the implementation of the QSVA method in an operational environment is suggested. The QSVA method is also applied to a variety of heavy rainfall cases over the Korean Peninsula in order to get robustness for the single-case results.

Forecast of a heavy rainfall case, which occurred on 26 July 2006, is improved by assimilating radar radial velocity data using the 4D-Var method of the WRFDA system. However, computational cost, including CPU and memory requirements, is high in the 4D-Var due to its iterative minimization of the cost function. A new data assimilation method based on the adjoint sensitivity of forecast error to the initial condition is proposed: Adjoint Sensitivity-based Data Assimilation (ASDA) method. In the ASDA method, the adjoint sensitivity of forecast error is calculated by running the adjoint model backwards, and this sensitivity is used to improve the original first guess. The forecast error is defined as the difference between the forecast from the original analysis and the verifying 3D-Var analysis at the forecast time, and the sensitivity is rescaled using a scaling factor determined by minimizing the observational part of the 4D-Var cost function. Finally, the scaled sensitivity is added to the original first guess to make an improved first guess, and an improved analysis is produced by

performing the 3D-Var with the improved first guess and the observations at the analysis time. The second objectives of this study are to suggest a new data assimilation method, namely the ASDA method and to compare the ASDA method with the existing data assimilation methods such as the 3D-Var and 4D-Var methods for a heavy rainfall case over the Korean Peninsula. In the ASDA method, the first-guess error and the observational error are not correlated with each other unlike the PMV (or GPV), and the computational cost is significantly reduced compared to the 4D-Var, maintaining the merits of the 4D-Var method.

Chapter 2. Algorithms

2.1. The Quasi Static Variational Assimilation (QSVA) algorithm

In the 4D-Var method, the cost function is a measure of the weighted sum of squared distances to the background and to the observations distributed over the assimilation window, and it is minimized to find the analysis.

$$J(x_0) = \frac{1}{2} (x_0 - x_0^b)^T B_0^{-1} (x_0 - x_0^b) + \frac{1}{2} \sum_{n=0}^N [y_n^o - H_n(M_n(x_0))]^T R_n^{-1} [y_n^o - H_n(M_n(x_0))]$$

, (1)

where x_0 is a control variable of the above minimization problem, the subscript 0 denotes the time $t=t_0$, x^b is the background state defined at $t=t_0$, and B_0 is the

background error covariance also defined at $t=t_0$. y^o is the observations at $t=t_n$, the subscript n varies from 0 to N , and R_n is the observation error covariance. H_n is the nonlinear observation operator and M_n is the nonlinear model operator, which evolves over time from x_0 to x_n valid at $t=t_n$.

When an analysis increment is defined as the difference between x_0 and the first guess, the cost function can be rewritten, after some manipulation, as follows.

$$\begin{aligned}
J(\delta x_0) &= \frac{1}{2} [\delta x_0 - (x_0^b - x_0^g)]^T B_0^{-1} [\delta x_0 - (x_0^b - x_0^g)] \\
&\quad + \frac{1}{2} \sum_{n=0}^N [d_n - \mathbf{H}_n(\mathbf{M}_n(\delta x_0))]^T R_n^{-1} [d_n - \mathbf{H}_n(\mathbf{M}_n(\delta x_0))] \\
\delta x_0 &= x_0 - x_0^g \\
d_n &= y_n^o - H_n(M_n(x_0^g)) \\
H_n(M_n(x_0)) - H_n(M_n(x_0^g)) &\approx \mathbf{H}_n(\mathbf{M}_n(\delta x_0))
\end{aligned}
\tag{2}$$

where δx_0 is the analysis increment, x^g is the first guess defined at $t=t_0$, and d_n is the innovation. \mathbf{H}_n and \mathbf{M}_n are the linearized observation and model operators, respectively.

In the QSVA algorithm, the time interval of an assimilation window is gradually increased from $[t_0, t_0]$ to $[t_0, t_N]$. If we define the cost function of 4D-Var with simplified notation,

$$J_N = J^b + J_N^o$$

$$J^b = \frac{1}{2} [\delta x_0 - (x_0^b - x_0^g)]^T B_0^{-1} [\delta x_0 - (x_0^b - x_0^g)]$$

$$J_i^o = \frac{1}{2} \sum_{n=0}^i [d_n - \mathbf{H}_n(\mathbf{M}_n(\delta x_0))]^T R_n^{-1} [d_n - \mathbf{H}_n(\mathbf{M}_n(\delta x_0))]$$

, (3)

the cost function for each step of the QSVA algorithm can be written as follows.

$$\begin{aligned}
A_0: J_0 &= J^b + J_0^o \\
A_1: J_1 &= J^b + J_1^o \\
&\vdots \\
A_n: J_n &= J^b + J_n^o \\
&\vdots \\
A_{N-1}: J_{N-1} &= J^b + J_{N-1}^o \\
A_N: J_N &= J^b + J_N^o
\end{aligned}
, (4)$$

where A_n is the n^{th} minimization task of the QSVA algorithm. It is noted that for the n^{th} minimization task, A_n , the starting point for the minimization of the cost function comes from the minimizer of the previous minimization task, A_{n-1} . In other words, in the QSVA algorithm, the first guess, not the background, is updated, which is similar to an outer-loop in 4D-Var.

2.2. The Adjoint Sensitivity-based Data Assimilation (ASDA) algorithm

A nonlinear evolution of a state vector can be expressed by using a nonlinear model:

$$\mathbf{x}_t = \mathbf{M}(\mathbf{x}_0) \quad , (5)$$

where \mathbf{x}_t and \mathbf{x}_0 are the state vectors at time t (i.e., final time) and 0 (i.e., initial time), and \mathbf{M} is a nonlinear model. A linear evolution of a small perturbation for the state vector can be described by a tangent linear model, the first-order derivative of the nonlinear model (operator):

$$\delta \mathbf{x}_t = \left. \frac{\partial \mathbf{M}}{\partial \mathbf{x}} \right|_{\mathbf{x}=\mathbf{x}_0} \delta \mathbf{x}_0 = \mathbf{L} \delta \mathbf{x}_0$$

, (6)

where δx_t and δx_0 are the perturbations at time t and 0 , and L is a tangent linear model.

A response function (or objective function), R is defined as a function of the state vector at time t , and it is differentiable to the state vector.

$$R = f(x_t)$$

, (7)

Variation of the response function at time t can be derived from Taylor expansion:

$$\Delta R \approx \delta R = \left\langle \frac{\partial R}{\partial x_t}, \delta x_t \right\rangle = \left\langle \frac{\partial R}{\partial x_t}, L \delta x_0 \right\rangle$$

, (8)

where \langle , \rangle denotes an inner product, and the definition of the tangent linear model (operator) is used for the last equality. By using an adjoint relationship,

$$\Delta R \approx \delta R = \langle L^* \frac{\partial R}{\partial x_t}, \delta x_0 \rangle, \quad (9)$$

where L^* is an adjoint model (operator).

Variation of the response function at time 0 is as follows:

$$\Delta R \approx \delta R = \langle \frac{\partial R}{\partial x_0}, \delta x_0 \rangle, \quad (10)$$

Consequently, an equation for adjoint sensitivity to initial condition is derived by equating the right-hand sides of Eqs. (9) and (10):

$$\frac{\partial R}{\partial x_0} = L^* \frac{\partial R}{\partial x_t}$$

, (11)

The above equation implies that sensitivity gradient of the response function at the initial time can be obtained by running the adjoint model with the sensitivity gradient of the response function at the final time as an input.

In this study, forecast error at time t measured in dry total energy is selected as the response function, and the forecast error is defined as the difference between the forecast from time 0 to t and the verifying 3D-Var analysis at time t .

$$R = \frac{1}{2} \langle P(x_t - x_t^{\text{ref}}), AP(x_t - x_t^{\text{ref}}) \rangle$$

, (12)

where x_t is the forecast obtained by running the nonlinear model with x_0 as an

initial condition, x^{ref} is the verifying analysis, A is the matrix defining the dry total energy norm, and P is a local projection matrix. The above response function can be rewritten as follows.

$$R = \frac{1}{2} \iiint_{\eta, \Sigma} [u'^2 + v'^2 + \left(\frac{g}{NT_r}\right)^2 T'^2 + \left(\frac{1}{\rho c_s}\right)^2 p'^2] d\Sigma d\eta, \quad (13)$$

where u , v , T , and p are zonal wind, meridional wind, temperature, and pressure components of the state vector, and prime denotes a perturbation. Gravitational acceleration, Brunt-Väisälä frequency, density of air, and speed of sound are denoted by g , N , ρ , and c_s , respectively, and T_r is a reference temperature. Horizontal integration domain defined by the local projection matrix is denoted by Σ , and η is a vertical coordinate.

The adjoint sensitivity of forecast error to initial condition given in Eq. (11) with the response function of Eq. (12) or (13) can be used as a perturbation to improve the original first guess.

$$\delta x_0^{\text{for fg}} = \alpha A^{-1} \frac{\partial R}{\partial x_0}$$

, (14)

where α is a scaling factor, and A^{-1} is for a unit conversion from the adjoint sensitivity to the state vector.

In order to determine the optimal value of the scaling factor, observational part of the cost function for 4D-Var is minimized using the observations to the final time. It should be noted that the observations at the initial time are excluded in determining the scaling factor.

$$J^o(\alpha) = \frac{1}{2} \sum_{i=1}^t [H_i' L(t_0, t_i) \alpha A^{-1} \frac{\partial R}{\partial x_0} - d_i^o]^T R_i^{-1} [H_i' L(t_0, t_i) \alpha A^{-1} \frac{\partial R}{\partial x_0} - d_i^o]$$

$$d_i^o = y_i^o - H_i(M(x_0))$$

, (15)

where J^o denotes observational part of the cost function, H' is a linearized version of an observation operator, H . The observation operator computes model equivalents to the observations through a transform from model space to observation space. d^o is an innovation, y^o is an observation, R is an observation error covariance matrix, and subscript i is for time dimension.

The above cost function is a quadratic function of the scaling factor:

$$J^o(\alpha) = \frac{1}{2} \sum_{i=1}^t \left[\alpha^2 \left\{ H_i' L(t_0, t_i) A^{-1} \frac{\partial R}{\partial x_0} \right\}^T R_i^{-1} \left\{ H_i' L(t_0, t_i) A^{-1} \frac{\partial R}{\partial x_0} \right\} \right. \\ \left. - 2\alpha \left\{ H_i' L(t_0, t_i) A^{-1} \frac{\partial R}{\partial x_0} \right\}^T R_i^{-1} d_i^o + d_i^{oT} R_i^{-1} d_i^o \right] , (16)$$

The optimal value of the scaling factor, α_{opt} , which corresponds to the minimum of the cost function, can be found by equating the first-order derivative of the cost function to zero:

$$\begin{aligned}
J^{o'}(\alpha) &= \sum_{i=1}^t [\alpha \left\{ H_i' L(t_0, t_i) A^{-1} \frac{\partial R}{\partial x_0} \right\}^T R_i^{-1} \left\{ H_i' L(t_0, t_i) A^{-1} \frac{\partial R}{\partial x_0} \right\} \\
&\quad - \left\{ H_i' L(t_0, t_i) A^{-1} \frac{\partial R}{\partial x_0} \right\}^T R_i^{-1} d_i^o] \\
\alpha_{\text{opt}} &= \frac{\sum_{i=1}^t \{ H_i' L(t_0, t_i) A^{-1} \frac{\partial R}{\partial x_0} \}^T R_i^{-1} d_i^o}{\sum_{i=1}^t \{ H_i' L(t_0, t_i) A^{-1} \frac{\partial R}{\partial x_0} \}^T R_i^{-1} \{ H_i' L(t_0, t_i) A^{-1} \frac{\partial R}{\partial x_0} \}}
\end{aligned}
\tag{17}$$

Finally, the adjoint sensitivity of forecast error scaled by the optimal scaling factor is added to the original first guess to make the improved first guess, and 3D-Var analysis is carried out using the improved first guess and the observations at the initial time to make the improved analysis.

$$x_0^{\text{new fg}} = x_0 + \delta x_0^{\text{for fg}} = x_0 + \alpha_{\text{opt}} A^{-1} \frac{\partial R}{\partial x_0}
\tag{18}$$

$$\begin{aligned}\delta x_0^{\text{ASDA}} &= \text{minimizer of } J^{\text{3dvar}}(\delta x) \\ J^{\text{3dvar}}(\delta x) &= \frac{1}{2}(\delta x)^T B^{-1} \delta x + \frac{1}{2}(H' \delta x - d^0)^T R^{-1}(H' \delta x - d^0) \\ d^0 &= y^0 - H(x_0^{\text{new fg}}) \\ &, (19)\end{aligned}$$

$$\begin{aligned}x_0^{\text{ASDA}} &= x_0^{\text{new fg}} + \delta x_0^{\text{ASDA}} \\ &, (20)\end{aligned}$$

where $x^{\text{new fg}}$ is the improved first guess for 3D-Var analysis at the initial time, J^{3dvar} is a cost function for 3D-Var at the initial time, and x^{ASDA} is the final initial condition (analysis) of ASDA method.

In the ASDA method, the original first guess is improved through the adjoint sensitivity-based perturbation, and the amplitude of the perturbation is determined objectively using the observations. By using the ASDA method, radar data can be assimilated effectively owing to its characteristics such as

flow-dependency. Unlike the PMV method, first-guess and observation errors are not correlated with each other in the ASDA method. In contrast to the 4D-Var method, the computational cost of the ASDA method is not high because it is not involved in iterative minimization of cost function.

Chapter 3. Numerical model, data assimilation system, and radar data

3.1. The Weather Research and Forecasting (WRF) model

The Weather Research and Forecasting (WRF) model is a flexible, state-of-the-art numerical weather prediction and atmospheric simulation system designed for both operational and research applications. The development of the WRF model has been a collaborative one among the National Center for Atmospheric Research (NCAR) Mesoscale and Microscale Meteorology (MMM) Division, the National Oceanic and Atmospheric Administration (NOAA)'s National Centers for Environmental Prediction (NCEP) and Earth System Research Laboratory (ESRL), Department of Defense's Air Force Weather Agency (AFWA) and Naval Research Laboratory (NRL), the Center for Analysis and Prediction of Storms (CAPS) at University of Oklahoma, and the Federal Aviation Administration (FAA). The WRF model is suitable for use in a broad range of applications across scales ranging from meters to thousands

of kilometers (from large eddy to global simulations), including idealized simulations, regional and global applications, real-time NWP, parameterization research, forecast research, data assimilation research, hurricane research, regional climate simulations, air quality modeling, and atmosphere-ocean coupling.

Governing equations are fully compressible, Euler nonhydrostatic, and scalar-conserving flux form for prognostic variables. Prognostic variables are horizontal velocity components, vertical velocity, perturbation potential temperature, perturbation geopotential, and perturbation surface pressure of dry air. Optionally, water vapor mixing ratio, rain/snow mixing ratio, cloud water/ice mixing ratio, turbulent kinetic energy, and chemical species are included as prognostic variables. Terrain-following, dry hydrostatic-pressure is a vertical coordinate, and horizontal grid system is an Arakawa C-grid staggering. Time-split integration based on the second- or third-order Runge-Kutta scheme with smaller time step for acoustic- and gravity-wave modes is used as a time integration scheme. The second- to sixth-order advection options are available in horizontal and vertical directions. Full Coriolis and curvature terms are included, and one-way, two-way, and moving nest options are available. A number of sophisticated physics schemes are provided, including

microphysics, cumulus parameterization, planetary boundary layer, surface physics, and atmospheric radiation schemes.

3.2. The WRF Data Assimilation (WRFDA) system

The WRF Data Assimilation (WRFDA) system has both 3D-Var and 4D-Var capabilities (variational components), and it also includes the capability of hybrid data assimilation (i.e., combined use of variational and ensemble methods). It can be used for both global and regional applications. The variational problem can be summarized as the iterative minimization of the cost function to find the analysis. The solution to the minimization problem represents the *a posteriori* maximum likelihood estimate of the current state of the atmosphere. The WRF Variational data assimilation (WRFVAR) system is based on a model-space and incremental formulation (Barker et al., 2004). In this approach, observations, background, their errors, and physical laws are combined to produce analysis increments, which are added to the first guess to provide an improved analysis (compared to the background estimate). The conjugate-gradient or Lanczos method is utilized to minimize the cost function

in the control variable space, and a variational analysis is performed on an unstaggered Arakawa A grid. Analysis increments on Arakawa A grid are interpolated to staggered Arakawa C grid, and they are added to the first guess to obtain the final analysis.

There are three inputs to the WRFVAR system: the first guess, observations (and the corresponding errors), and background error covariances. In cold-start mode, the first guess is typically from WRF preprocessing system. In cycling mode (e.g., in an operational system), the first guess is a short-range WRF forecast. Currently, conventional observations, radar radial velocity/reflectivity observations, satellite radiance observations, and precipitation can be assimilated in the WRFDA system.

Preconditioning of the background part of the cost function is done through the control variable transform, U defined as $B=UU^T$. Horizontal component of the background error is represented by a recursive filter (for regional application) or power spectrum (for global application). The vertical component is applied via projections on climatologically-generated averaged eigenvectors and its corresponding eigenvalues. Horizontal and vertical background errors are non-separable. In other words, each eigenvector has its own horizontal climatologically-determined length scale. Finally, multivariate covariances are

modeled by computing regression coefficients between velocity potential and streamfunction, temperature and streamfunction, and surface pressure and streamfunction (optionally, moisture variables can be included). Climatological background error covariances are estimated through the NMC method of averaged forecast differences or suitably averaged ensemble perturbations.

3.3. Radar data

In South Korea, a total of 18 operational radars have been operated since the summer of 2006, all of which have Doppler capability. The radars are separated by a distance of approximately 120 km on average, and their unambiguous ranges are greater than 100 km; hence, most areas over the Southern Korean Peninsula are overlapped by the coverage of two or more radars. The United States Air Force (USAF) radars (RKSG and RKJK) are the Weather Surveillance Radars-1988 Doppler (WSR-88D) and operated near 10.0-cm wavelength. The Korea Air Force (KAF) radars (RKWJ, RSCN, RTAG, RYCN, and RWNJ) are operated near 5.5-cm wavelength. The other radars are operated near 5.5- or 10.0-cm wavelength and by Korea Meteorological Administration

(KMA). Details on radar network over the Southern Korean Peninsula can be found in Park and Lee (2009).

Radar data used in data assimilation experiments are preprocessed by the method given in Park and Lee (2009). Noises and errors embedded in the radar measurements were processed, and the remaining ground clutter signals and anomalous echoes were eliminated. Further, the radial velocity measurements were processed in terms of the aliasing effect and the dual-Pulse Repetition Frequency (PRF) velocity error. After the quality-control procedures for the radar measurements, the radar data were interpolated and thinned to Cartesian grids at a resolution that is compatible with the analysis system by the Sorted Position Radar INTERpolation (SPRINT; Mohr and Vaughan, 1979; Miller et al., 1986) and Custom Editing and Display of Reduced Information in Cartesian coordinate (CEDRIC; Mohr et al., 1986) packages from the NCAR. The radar data were finally hole-filled and smoothed by the CEDRIC package and then converted to the WRFDA input ASCII format. The final radar data have a horizontal resolution of approximately 6 km, vertical resolution of 0.5 km above a height of about 3 km, and temporal resolution of approximately 10 minutes.

Chapter 4. The QSVA method and its comparison to outer-loop method

4.1. Case description

The heavy rainfall case for this study can be categorized as an air-mass thunderstorm that developed as a result of daytime solar heating. Figure 4.1 shows the 6-h accumulated rainfall distribution over South Korea and the time series of hourly rainfall at Taebaek and Namwon for the period of 0600 UTC to 1200 UTC 6 August 2006. Rainfall was concentrated over the east coast and the southwestern part of the Korean Peninsula. Over the east coast, hourly rainfall at Taebaek peaked at 0800 UTC 6 August 2006 and the 6-h accumulated rainfall was 37.5 mm. Over the southwestern part, the 6-h accumulated rainfall at Namwon was 33.5 mm and it peaked at 1000 UTC 6 August 2006. Note that rainfall was localized over a small area and it was concentrated near the peak time.

In this case, the atmosphere over the Korean Peninsula was unstable because

the Korean Peninsula was located along the edge of a North Pacific high-pressure system. Warm and moist air was transported to the Korean Peninsula along the edge of the North Pacific high at the 850 hPa level. In contrast, cold air surged into the Korean Peninsula by a northwesterly flow related to a cold trough at the 200 hPa level (figures not shown). This synoptic environment caused the atmosphere over the Korean Peninsula to be convectively (conditionally) unstable.

Figure 4.2a shows skew T-log p diagrams for Gwangju, which is approximately 50-km southwest of Namwon, at 0000 UTC and 0600 UTC 6 August 2006. The thermodynamic quantities obtained by analyzing the diagrams are given in Table 4.1. Convective Available Potential Energy (CAPE) and Convective Inhibition (CIN) at 0000 UTC 6 August 2006 were 124 J kg^{-1} and 217 J kg^{-1} , respectively. Cold air was supplied continuously at upper levels by an upper-level trough, and after sunrise, the land surface was heated by solar heating. This destabilized the atmosphere near Gwangju and raised (lowered) CAPE (CIN) to $1970 \text{ (6)} \text{ J kg}^{-1}$ at 0600 UTC 6. During the same period, the Level of Free Convection (LFC) was lowered from 3836 m to 1456 m. It can be also found that winds below 700 hPa were weak, and hence, wind shear did not play an important role in the development of the storm in this case.

The vertical structures of the potential temperature and equivalent potential temperature for Gwangju at 0000 UTC and 0600 UTC 6 August 2006 are shown in Fig. 4.2b. Both at 0000 UTC and 0600 UTC, the atmosphere at Gwangju was statically stable based on the analysis of the potential temperature. At 0000 UTC 6, the atmosphere was also conditionally stable, except for the very shallow layer near the 850 hPa level. The decrease in the equivalent potential temperature from the 850 hPa to 700 hPa level was approximately 10 K at 0600 UTC 6 August 2006, and thus the mid atmosphere at Gwangju was conditionally unstable.

Figure 4.3 shows the horizontal cross section of the horizontal wind and divergence at a height of 4 km and the vertical cross section of the vertical wind and divergence along the line in the horizontal cross section. At Namwon, the hourly rainfall from 0900 UTC to 1000 UTC 6 August 2006 was greatest, and therefore the cross sections for 0900 UTC are shown. As previously mentioned, the atmosphere near Namwon was conditionally unstable. In other words, if there is a forcing for lifting of the air parcel to its LFC, a strong upward motion and (if there is enough moisture) a large amount of rainfall can be induced. A northerly or northwesterly flow and a southwesterly flow met near Namwon, and this formed a convergence zone (Fig. 4.3a). This convergence acted as a

lifting forcing, and there was torrential rainfall near Namwon, lasting approximately one hour from 0900 UTC. The updraft related to the convective instability extended to near the tropopause with a maximum value of approximately 2 m s^{-1} at a height of 7 km. There was also a compensating downdraft beside the updraft, which was related to upper-level convergence and lower-level divergence (Fig. 4.3b). It should be noted that Jiri Mountain, which is southeast of Namwon, may play an important role in the initiation and development of the storm.

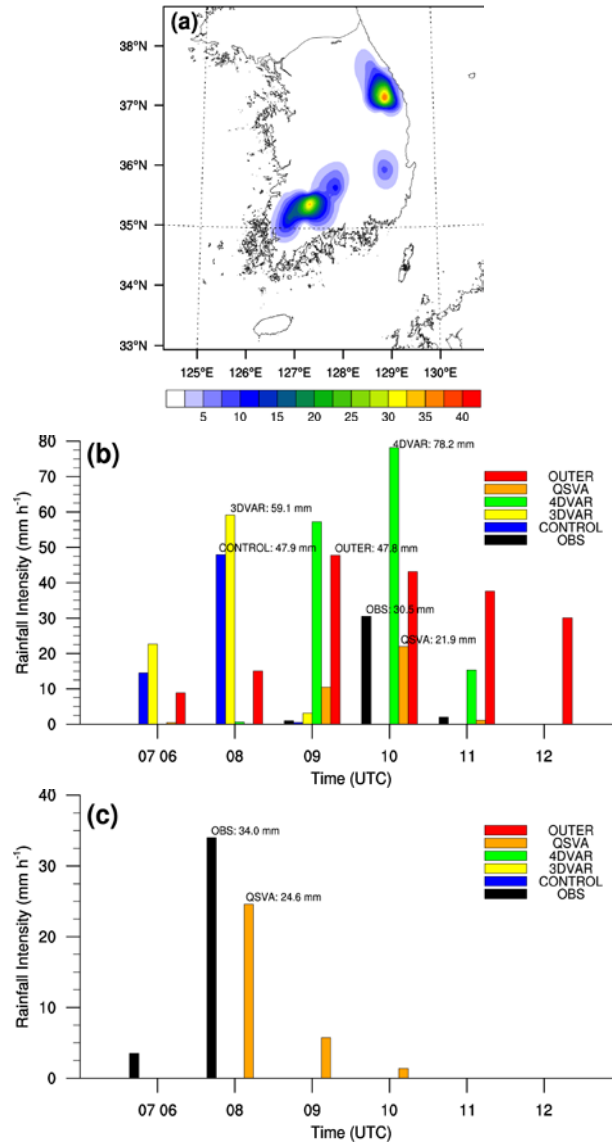


Figure 4.1. (a) Observed 6-h accumulated rainfall ($\text{mm } 6\text{h}^{-1}$) distribution over South Korea from 0600 UTC to 1200 UTC 6 August 2006. Time series of hourly rainfall ($\text{mm } \text{h}^{-1}$) from 0600 UTC to 1200 UTC 6 August 2006 for the observations (black), CONTROL (blue), 3DVAR (yellow), 4DVAR (green), QSVA (orange), and OUTER (red) experiments at (b) Namwon and (c) Taebaek. In the case of numerical experiments, hourly rainfalls at the grid points corresponding to Namwon and Taebaek are shown.

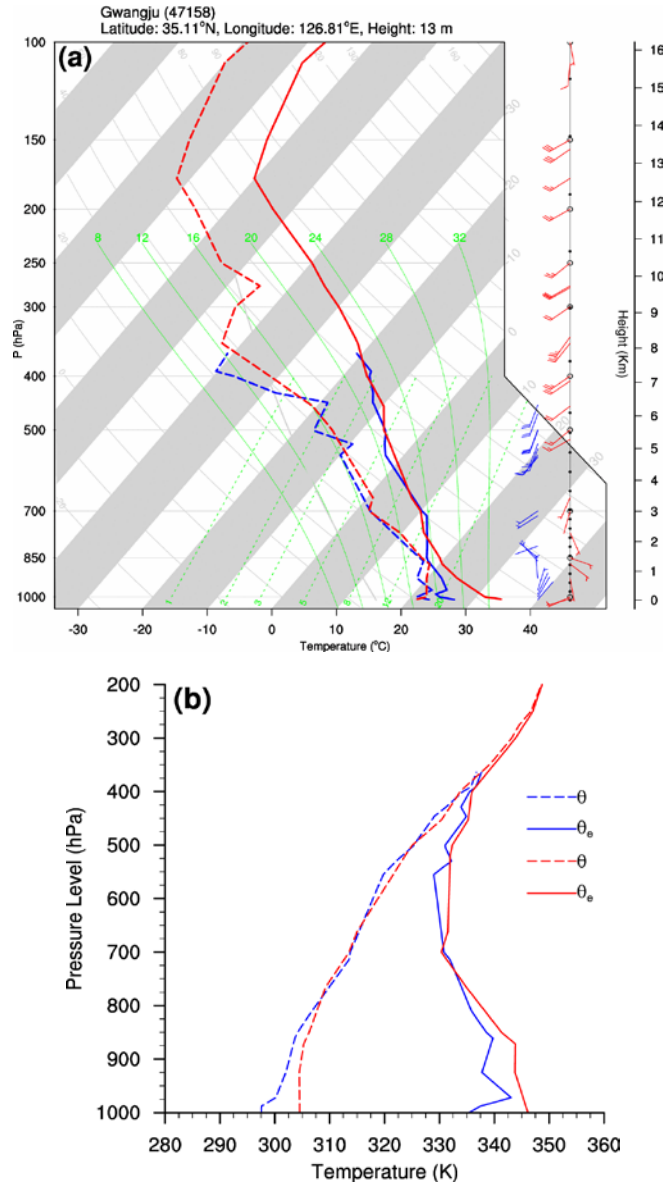


Figure 4.2. (a) Skew T-log p diagram computed from radiosonde observations of Gwangju at 0000 UTC (blue) and 0600 UTC (red) 6 August 2006. (b) Vertical profile of potential temperature (K, solid line) and equivalent potential temperature (K, dashed line) for Gwangju at 0000 UTC (blue) and 0600 UTC (red) 6 August 2006.

Table 4.1. Convective Available Potential Energy (CAPE, J kg⁻¹), Convective Inhibition (CIN, J kg⁻¹), Lifting Condensation Level (LCL, m), and Level of Free Convection (LFC, m) computed from sounding observations of Gwangju at 0000 UTC and 0600 UTC 6 August 2006.

	CAPE	CIN	LCL	LFC
0000 UTC 6 August 2006	124	217	451	3836
0600 UTC 6 August 2006	1970	6	1152	1456

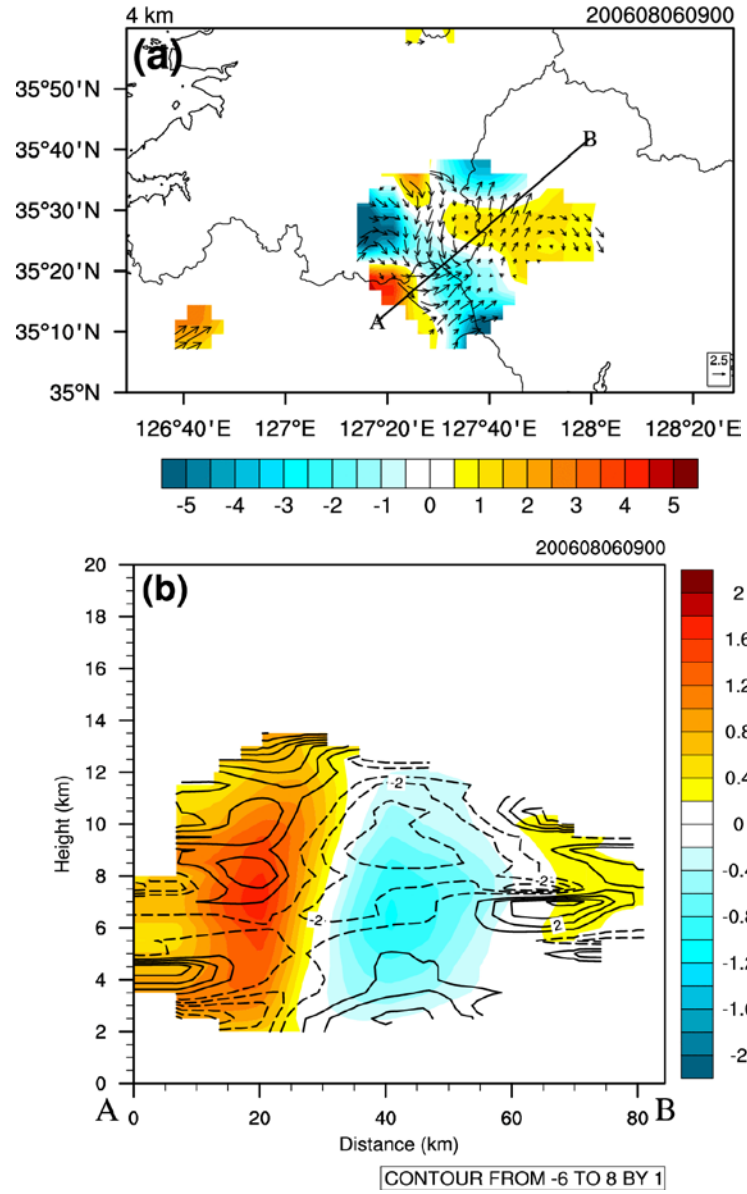


Figure 4.3. Radar analyses near Namwon area at 0900 UTC 6 August 2006. (a) Horizontal distribution of divergence (10^{-4} s^{-1} , shading) and winds (m s^{-1} , vector) at 4-km height. (b) Vertical cross section along the line shown in (a) of vertical wind (m s^{-1} , shading) and divergence (10^{-4} s^{-1} , negative values are denoted by dashed contours).

4.2. Experimental design

In this study, the Advanced Research Weather Research and Forecasting (ARW-WRF) model (Skamarock et al., 2008) was used as a forecasting model. A total of six experiments are carried out, and details of the experiments are given in Table 4.2. Triply-nested domains, focusing on South Korea, with horizontal resolutions of 54 km (domain 1), 18 km (domain 2), and 6 km (domain 3) are employed (Fig. 4.4). The number of horizontal grid points for each domain is 120×102 , 121×103 , and 121×127 , respectively, and the number of vertical levels for all of the domains is 35 with the model top at 50 hPa. The selected physics schemes are the WRF Single-Moment 6-class (WSM6) with graupel microphysics scheme (Hong and Lim, 2006), the Kain-Fritsch cumulus parameterization scheme (Kain, 2004), the Yonsei University (YSU) planetary boundary layer scheme (Hong et al., 2006), the Rapid Radiative Transfer Model (RRTM) longwave radiation scheme (Mlawer et al., 1997), and the Dudhia shortwave radiation scheme (Dudhia, 1989). The global final analysis (FNL) data from the National Center for Environmental Prediction (NCEP) with a horizontal resolution of approximately 100 km are

used to create initial and boundary conditions. Initial time for domain 1, domain 2, and domain 3 is 1200 UTC 5, 0000 UTC 6, and 0600 UTC 6 August 2006, respectively, and only the 6-h forecast of domain 3 is considered in this study.

The WRFDA system version 3.4 (Huang et al., 2009) is used for all the data assimilation experiments, and the data assimilation experiments are conducted only on domain 3. The WRFDA system has both 3D-Var and 4D-Var (and outer loop) capabilities, and the QSVa algorithm introduced in section 2.1 is implemented. Background for all the data assimilation experiments is the initial condition of the CONTROL experiment (i.e., cold start), and the 6-h forecast from 0600 UTC to 1200 UTC 6 August 2006 is made using the analysis of each data assimilation experiment. The background error covariance is calculated using the National Meteorological Center (NMC) method (Parrish and Derber, 1992), in which the background error statistics are derived from the differences between 24- and 12-h forecasts for the one-month period of August 2006.

Radar radial velocity data from 13 radar observation sites over the Korean Peninsula are assimilated in this study. A detailed description of the radar data over the Korean Peninsula can be found in Park and Lee (2009). In advance of being assimilated, radar data are preprocessed using the methods given by Park and Lee (2009). The preprocessing includes quality control,

interpolation/thinning to Cartesian grids by the Sorted Position Radar INTerpolation (SPRINT; Mohr and Vaughan, 1979; Miller et al., 1986) and Custom Editing and Display of Reduced Information in Cartesian coordinate (CEDRIC; Mohr et al., 1986) packages, and hole-filling/smoothing by the CEDRIC package. Finally, radar data are converted to the WRFDA input format. The radar data have a horizontal resolution of approximately 6 km and a vertical resolution of about 0.5 km. The assimilation window covers the period from 0600 UTC to 0630 UTC 6 August 2006, and radar data are provided every 10 minutes within the assimilation window.

Table 4.2. Brief description for each numerical experiment.

Experiment name	Description
CONTROL	No radar data are assimilated
3DVAR	Radar data are assimilated using the 3D-Var method
4DVAR	Radar data are assimilated using the 4D-Var method (with single outer loop)
OUTER	Radar data are assimilated using the 4D-Var method with 3 outer loops
QSVA	Radar data are assimilated using the QSVA method
QSVA_LC	Same as QSVA experiment except for loose inner- loop stopping criterion ($\text{eps} = 0.1$)

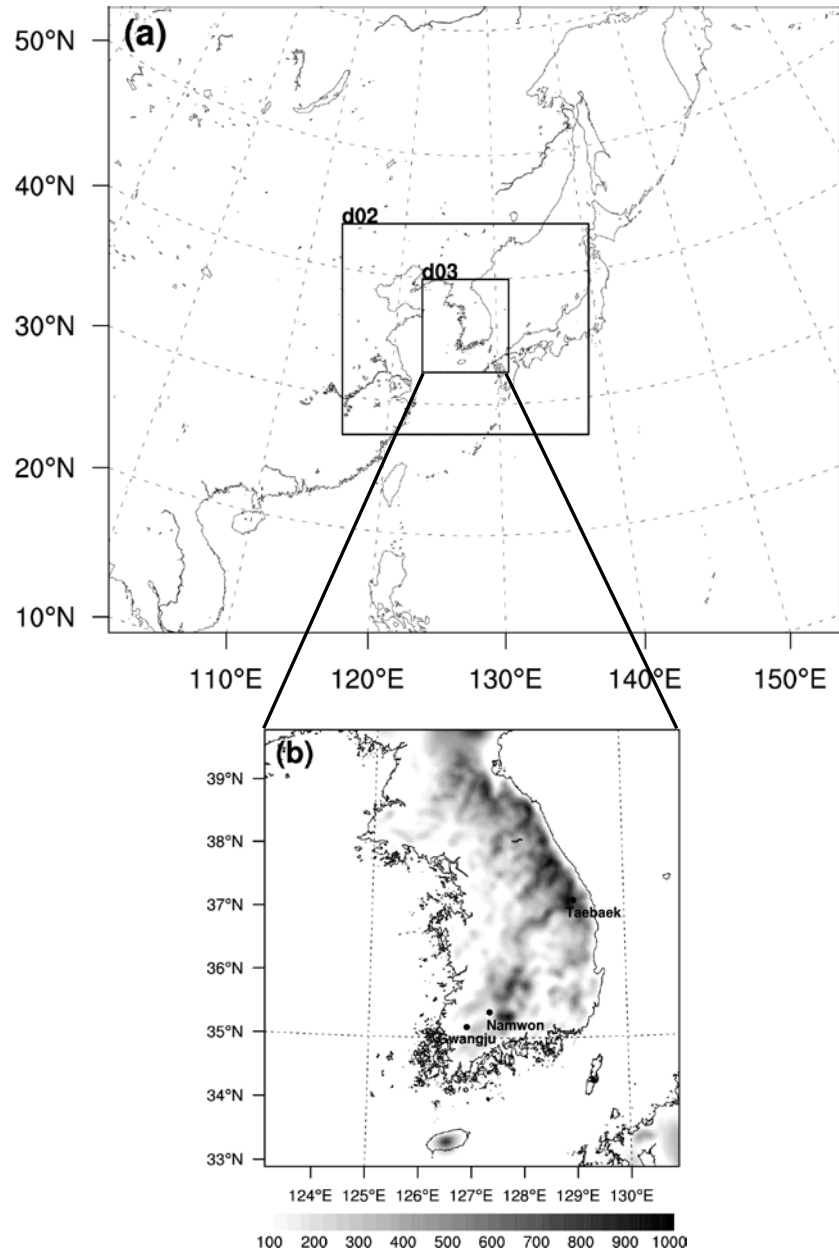


Figure 4.4. Domain configuration. (a) Geographical area for domains 1, 2, and 3 and (b) model terrain height (m) for domain 3. Locations of Namwon, Taebaek, and Gwangju cities are also indicated.

4.3. Results and discussion

Radar radial velocity data are assimilated to simulate the heavy rainfall described in section 4.1. The 3D-Var method shows no significant improvement in rainfall forecast. When radar data are assimilated using the 4D-Var method, the heavy rainfall is not simulated perfectly, but the rainfall forecast is partially improved compared to the 3D-Var method. In order to enhance the heavy rainfall forecast, more-than-one outer loops and the QSVA method are used. Figure 4.5 shows values of the cost function as a function of iteration number for the 3DVAR, 4DVAR, and OUTER experiments. The conjugate gradient method is used to solve a linearized minimization problem iteratively, and the minimization is terminated when the gradient norm decreases by two orders of magnitude (i.e., $\text{eps} = 0.01$), as suggested by Daley and Barker (2001). In the 3DVAR experiment, the minimization converges after 12 iterations, and the cost function decreases from 1735.87 to 976.95 (Fig. 4.5a). The minimization converges in 21 iterations in the 4DVAR experiment, and the cost function is reduced to approximately 46.2% of its starting value (from 7877.05 to 3640.80; Fig. 4.5b). Originally, a total of 4 outer loops are used in the OUTER

experiment. Inner-loop minimization for each outer loop converged after 21, 26, 26, and 29 iterations respectively. Through the inner-loop minimization, the cost function decreases from 7877.05 to 3640.80 (same as in the 4DVAR experiment) in the first outer loop, from 3789.28 to 3597.56 in the second outer loop, and from 3643.60 to 3561.16 in the third outer loop (Fig. 4.5c). When comparing the ending value of the cost function in the current outer loop with the starting value of the cost function in the following outer loop, there is a jump-up. This is attributed to two factors: the first is the nonlinearity of the forecast model and/or observation operator, and the second is additional observations getting into the assimilation, which are rejected in the previous outer loop (Table 4.3). In the fourth outer loop, the cost function is reduced from 3619.12 to 3565.03 (Fig. 4.5c). Although the cost function decreases to 98.5% of its starting value, its ending value is greater than that of the third outer loop. This implies that there is a divergence at the outer-loop level, and the divergence may be related to an inconsistency between the physics schemes in the nonlinear model and those in the linear model. In the remainder of this section, the OUTER experiment refers to the use of the 4D-Var method with 3 outer loops.

In the QSVA experiment, the length of the assimilation window for each

minimization task increases from 0 minute (equivalent to that of the 3DVAR experiment) to 30 minutes (equivalent to the 4DVAR experiment) in 10-minute interval, and the starting point of the current minimization comes from the minimizer of the previous minimization¹. The minimization for each assimilation window converges after 12, 20, 22, and 25 iterations, respectively. The cost function decreases from 1735.87 to 976.95 (same as in the 3DVAR experiment) for the 0-minute assimilation window, from 1971.65 to 1788.47 for the 10-minute assimilation window, and from 2961.01 to 2796.00 for the 20-minute assimilation window. When the length of the assimilation window is 30-minute, the cost function decreases from 3821.66 to 3563.56 (Fig. 4.6). It is noted that the ending value of the cost function in the final minimization of the QSVA experiment is less than that in the 4DVAR experiment, and it is similar to that in the third outer loop of the OUTER experiment.

Table 4.3 shows the Root Mean Square Errors (RMSEs) of O-B (observation minus background or first guess) and O-A (observation minus analysis) for the radial velocity and the number of assimilated observations. In all of the data

¹ In the OUTER and QSVA experiments, the first guess, not the background, is updated. One of basic assumptions in variational data assimilation is that there should be no correlation between background and observations errors. Updating the background violates this assumption.

assimilation experiments, the RMSE of O-A is smaller than that of O-B, which is a natural result of data assimilation. In the 4DVAR experiment, the RMSEs of O-B and O-A are 2.270 and 1.446, respectively. When more-than-one outer loops are employed, the RMSE of O-A is reduced to 1.431 (two outer loops) and 1.417 (three outer loops). In the QSVA experiment, as the length of the assimilation window increases, the RMSE of O-A is reduced consistently in spite of the increase in the number of assimilated observations. When the length of the assimilation window is 30-minute, the RMSEs of O-B and O-A are 1.508 and 1.424, respectively. The RMSEs of O-B and O-A for the OUTER or QSVA experiment are much smaller than those for the 4DVAR experiment. The number of assimilated observations in the OUTER and QSVA experiments is greater than that in the 4DVAR experiment although the difference is not significant.

Vertical distribution of the Root Mean Square Difference between the analysis and background estimate (RMSD of analysis increment) for the 4DVAR, OUTER, and QSVA experiments are shown in Fig. 4.7. For the OUTER experiment, analysis increments are calculated by using the analysis and the original first guess or updated first guesses from the analyses of the first and second outer-loops. Likewise, for the QSVA experiment, the original first guess

or updated first guesses from the analyses of assimilation tasks with 0, 10, and 20-minute assimilation window is used when analysis increments are calculated. In the 4DVAR experiment, analysis increments of both zonal and meridional wind are the largest at about 600 hPa, where radial velocity data are plentiful. In other words, analysis increments between 700 and 400 hPa (i.e., mid-levels) are large because more observations are assimilated at those levels. Analysis increments at lower or upper levels, where radial velocity data are relatively scarce, have some values greater than zero due to the spreading effect of background error covariance and model dynamics in assimilating radial velocity data. Analysis increments of the OUTER experiment are reduced progressively as more outer-loops are applied, especially at mid-levels. Similarly, analysis increments of the QSVA experiment are reduced progressively as the length of the assimilation window is increased. This indicates that the background estimates (or first guesses) of the OUTER and QSVA experiments become closer to the observations than the 4DVAR experiment as more outer-loops are applied, or the assimilation window is lengthened. It is also noted that overall structures of RMSDs of analysis increments for the OUTER and QSVA experiments are similar to the 4DVAR experiment when the original first guess is considered. This is consistent with

horizontal distribution of incremental wind shown in Fig. 4.14.

Based on analyses of the cost function, O-B/O-A statistics, and the RMSD of the analysis increment, it can be concluded that the background estimate and the analysis of the OUTER and QSVA experiments are better than those of the 4DVAR experiment. In detail, the ending value of the cost function and the RMSE of O-A for the OUTER and QSVA experiments are smaller than those for the 4DVAR experiment, and this implies that the analyses of the OUTER and QSVA experiments are closer to the observations than that of the 4DVAR experiment. These improved analyses of the OUTER and QSVA experiments are due to a better background estimate, which can be deduced from the RMSE of O-B and the RMSD of the analysis increment. Furthermore, the number of assimilated observations in the OUTER and QSVA experiments increases compared to the 4DVAR experiment because additional observations, which are rejected in the 4DVAR experiment, get into the assimilation in the OUTER and QSVA experiments. In the WRFDA system, the observations whose innovations (O-B) are larger than a threshold value (defined as a multiple of the observations error) are rejected. In the OUTER and QSVA experiments, the background estimate is improved consistently, and hence O-B decreases accordingly.

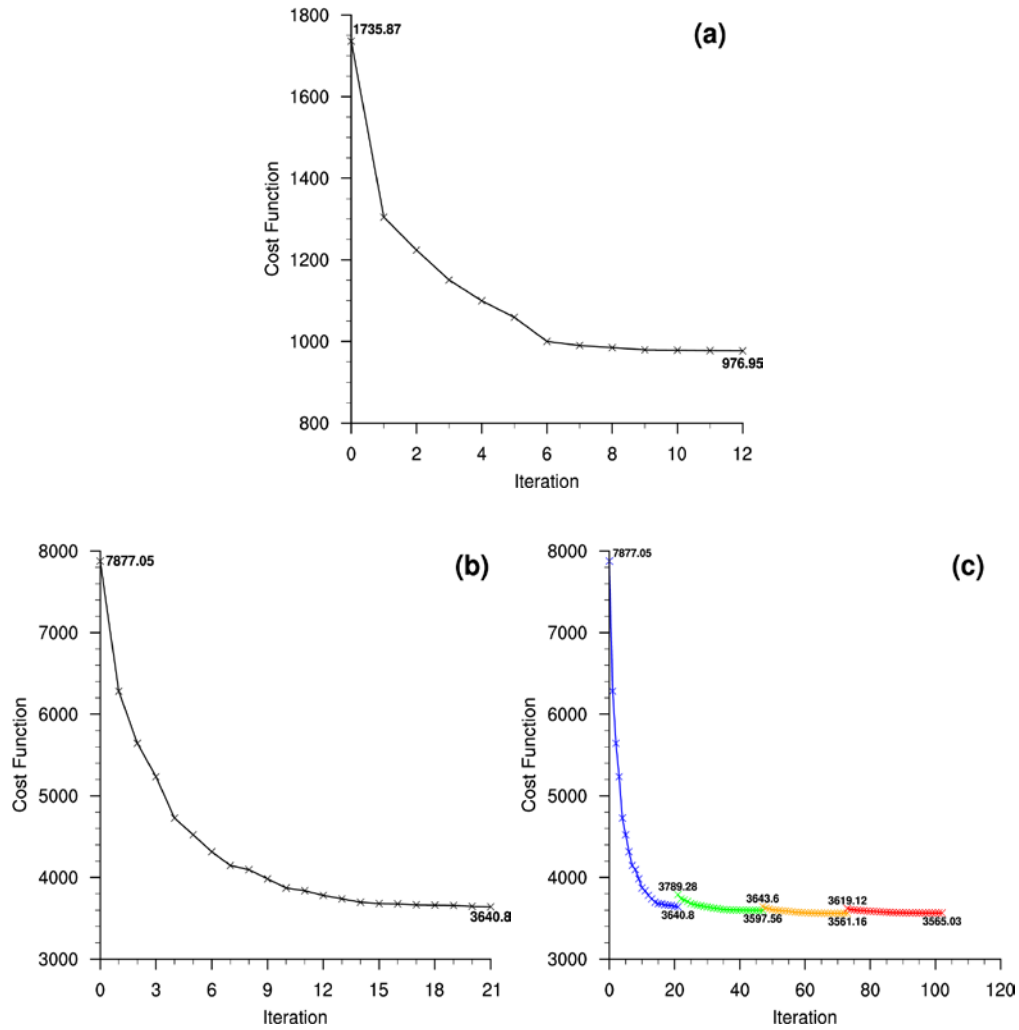


Figure 4.5. Cost-function values as a function of iteration number for the (a) 3DVAR, (b) 4DVAR, and (c) OUTER experiments. In the OUTER experiment, a total of 4 outer loops are used, and cost-function values for the first- (blue), second- (green), third- (orange), and fourth-outer-loop (red) are shown. Maximum and minimum values of cost function are indicated at the maximum/minimum points of each curve.

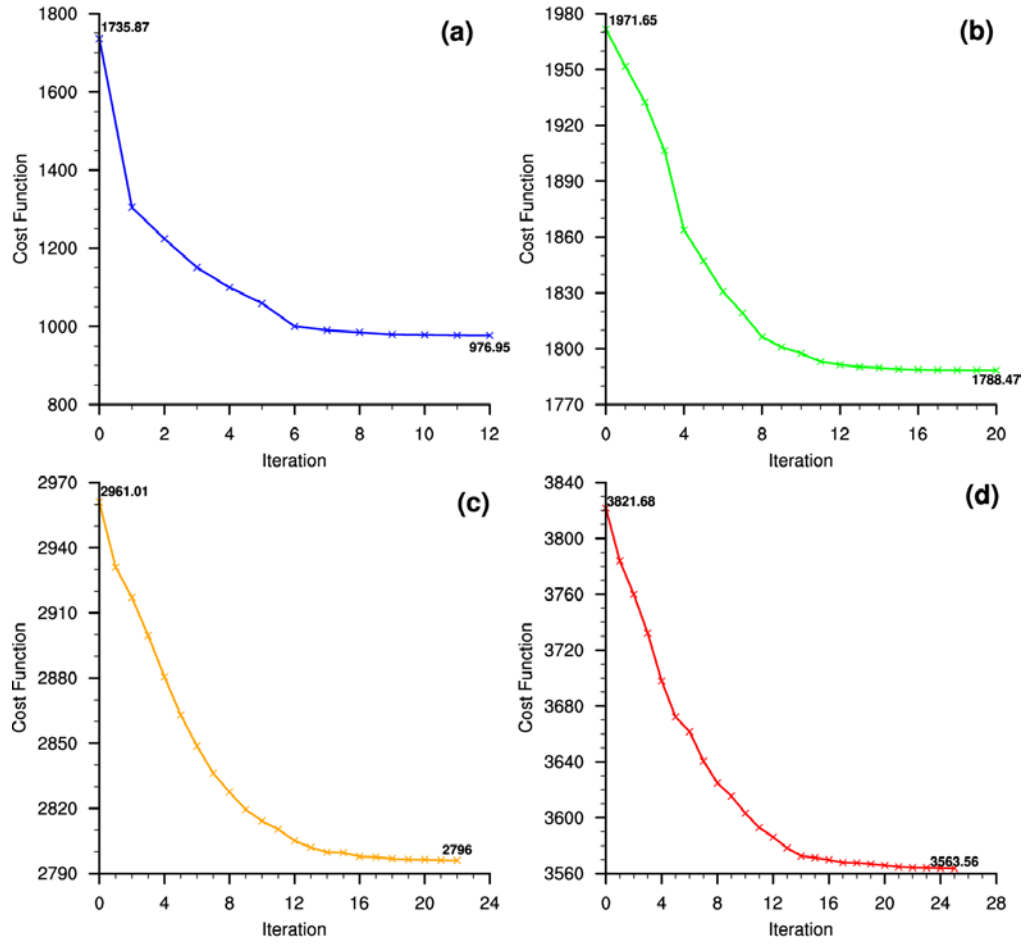


Figure 4.6. Cost-function values as a function of iteration number for assimilation tasks of the QSVa experiment with assimilation window of (a) 0 minute, (b) 10 minutes, (c) 20 minutes, and (d) 30 minutes. Maximum and minimum values of cost function are indicated at the maximum/minimum points of each curve.

Table 4.3. Root Mean Square Errors (RMSEs, m s^{-1}) of O-B and O-A for radar radial velocity and the number of assimilated observations for the 3DVAR, 4DVAR, OUTER, and QSVA experiments. The number in parenthesis in the OUTER experiment means the number of outer loops applied and that in the QSVA experiment means the length of the assimilation window (in minute) for each assimilation task.

	3DVAR	4DVAR	OUTER (2)	OUTER (3)	QSVA (0)	QSVA (10)	QSVA (20)	QSVA (30)
O-B	2.272	2.270	1.479	1.441	2.272	1.616	1.545	1.508
O-A	1.603	1.446	1.431	1.417	1.603	1.479	1.465	1.424
# of assimilated OBSs	2691	12226	12228	12228	2691	5694	9142	12228

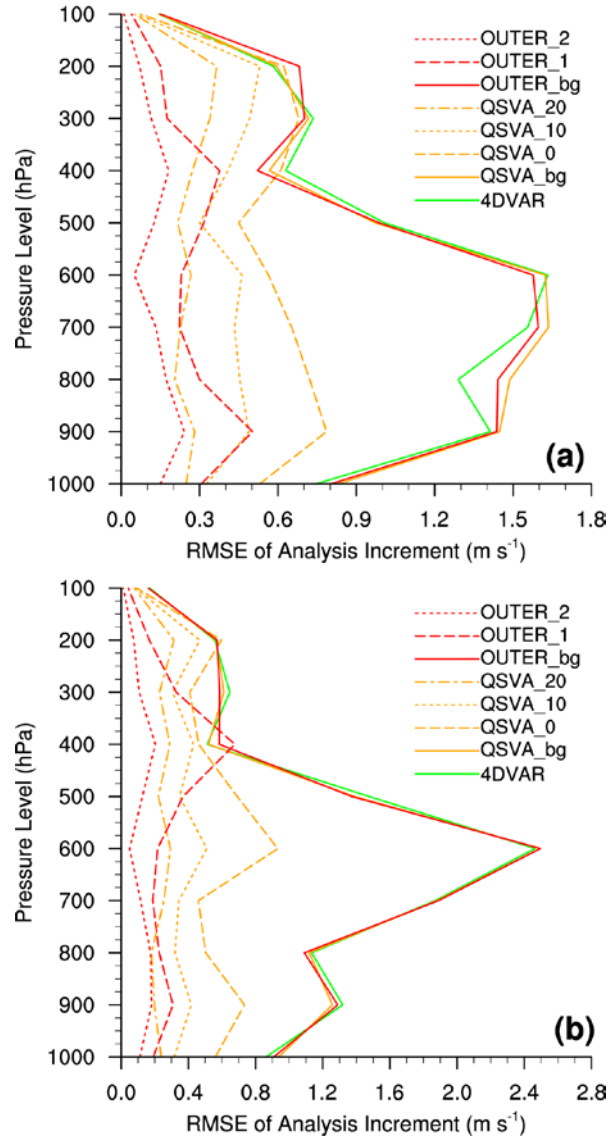


Figure 4.7. Vertical distribution of RMSD of analysis increment for the 4DVAR (green), QSVA (orange), and OUTER (red) experiments. (a) Zonal wind (m s^{-1}) and (b) meridional wind (m s^{-1}). For the QSVA experiment, original first guess (solid) and updated first guesses from analysis of assimilation task with 0-min (dashed), 10-min (dotted), and 20-min (dash-dotted) assimilation window are used in calculating analysis increment. Likewise, for the OUTER experiment, original first guess (solid) and updated first guesses from analysis of the first (dashed) and second (dotted) outer loop are used.

The nonlinearity of the original minimization problem is investigated using two measures, namely the percentage error in linearization and the pattern correlation. It should be noted that the linearized minimization problem is solved using an iterative method in the 4DVAR, OUTER, and QSVA experiments, and hence, the nonlinearity refers to that of the original nonlinear minimization problem, and the nonlinearity measures can be used to indicate the gap between nonlinear and linear growth (i.e., the nonlinearity can be interpreted as the gap). In order to compute these two measures, the nonlinear and linear growths of a perturbation are estimated according to Trémolet (2004) as follows. An analysis increment is used as the perturbation. The nonlinear growth of the perturbation is defined as the difference between two nonlinear-model runs, one from an unperturbed initial condition, and the other from a perturbed initial condition. The unperturbed initial condition is from the background estimate, and the perturbed initial condition is the sum of the unperturbed initial condition and the perturbation. The linear growth of the perturbation is from a linear-model run of the perturbation with nonlinear model trajectory for linearization coming from the nonlinear-model run of the unperturbed (perturbed) initial condition in the case of the 4DVAR (OUTER or QSVA) experiment. The typical maximum amplitude of the perturbation is of

the order of $7.6 \text{ m s}^{-1}/3.0 \text{ K}$, $0.63 \text{ m s}^{-1}/1.0 \text{ K}$, and $1.9 \text{ m s}^{-1}/3.0 \text{ K}$ for the 4DVAR, OUTER, and QSVA experiments, respectively. The percentage error in linearization is defined as follows:

$$\text{Error (\%)} = \frac{\text{NLG} - \text{LG}}{\text{LG}} \times 100$$

$$\text{DTE} = \frac{1}{2} \iiint_{\eta, \Sigma} [u'^2 + v'^2 + \left(\frac{g}{NT_r}\right)^2 T'^2 + \left(\frac{1}{\rho c_s}\right)^2 p'^2] d\Sigma d\eta$$

, (21)

where NLG stands for the nonlinear growth of the perturbation and LG stands for the linear growth of the perturbation. Each growth is calculated in terms of dry total energy (DTE) over the whole domain. u , v , T , and p are the zonal wind, meridional wind, temperature, and pressure components of the state vector, and a primed symbol denotes the evolved perturbation. The gravitational acceleration, Brunt-Väisälä frequency, density of air, and speed of sound are denoted by g , N , ρ , and c_s , respectively, and T_r is a reference temperature. The

pattern correlation between nonlinearly- and linearly-evolved fields is calculated for each component (u, v, T, and p), and the pattern correlations of all the components are averaged.

Figure 4.8 shows the percentage error in linearization and the pattern correlation within the assimilation window for the 4DVAR, OUTER, and QSVA experiments. The percentage error in linearization can be interpreted as follows. A value of zero indicates that there is no error in linearization; a positive value indicates that nonlinear growth is greater than linear growth; and a negative value indicates that linear growth is greater than nonlinear growth. During the assimilation window, the percentage errors for all of the experiments are negative, and hence linear growth is greater than nonlinear growth. From 0 to 15-minute into the forecast, the difference in the percentage errors among the 4DVAR, OUTER, and QSVA experiments is not large. However, the percentage error of the 4DVAR experiment increases abruptly for the next 15 minutes, and the percentage error of the 4DVAR experiment at 30-minute into the forecast is less than -20%, whereas the percentage errors of the OUTER and QSVA experiments remain close to zero (Fig. 4.8a). This implies that the gap between nonlinear and linear growth is reduced in the OUTER and QSVA experiments compared to that in the 4DVAR experiment because nonlinearity in the forecast

model and/or observation operator is taken into account by updating the nonlinear model trajectory. From 0 to 10-minute into the forecast, the percentage error of the minimization task with a 10-minute period is larger than those of minimization tasks with 20- and 30-minute periods in the QSVA experiment. Similarly, from 10 to 20-minute into the forecast, the percentage error of the minimization task with a 20-minute period is larger than that of the minimization task with a 30-minute period (Fig. 4.8a). This is because of the improved nonlinear model trajectory and background estimate with increasing length of the assimilation window in the QSVA experiment. However, the percentage error at the end of the assimilation window increases with increasing length of the assimilation window because a lengthy assimilation window is usually related to a greater degree of nonlinearity. Thus, the nonlinearity of the minimization problem is smallest for an assimilation window of 10-minute in the QSVA experiment.

The percentage error in linearization can be interpreted as a measure of the nonlinearity in terms of amplitude, and the pattern correlation can be interpreted as a measure of the nonlinearity in terms of phase. Roughly, the pattern correlation decreases as the forecast length increases. As in the analysis of the percentage error in linearization, the differences in the pattern correlation

among the 4DVAR, OUTER, and QSVA experiments increases after 15-minute into the forecast. The pattern correlation of the 4DVAR experiment decreases rapidly for the final 15 minutes, and at 30-minute into the forecast, it is less than 0.7. Contrastively, the pattern correlations of the OUTER and QSVA experiments are greater than 0.8 and 0.9, respectively, even at 30-minute into the forecast (Fig. 4.8b). As the length of the assimilation window increases in the QSVA experiment, the gap between nonlinear and linear growth in terms of pattern correlation decreases consistently owing to the improved nonlinear model trajectory and background estimate. It should be noted that the nonlinearity of the minimization problem, which is expressed as the pattern correlation at the end of each assimilation window, increases with increasing assimilation window in the QSVA experiment.

Based on the analyses of the percentage error in linearization and pattern correlation, it can be seen that the gap between nonlinear and linear growth is reduced in the OUTER and QSVA experiments. In the OUTER experiment, as more outer loops are applied, the background estimate and nonlinear model trajectory for linearization are updated. Similarly, in the QSVA experiment, as the length of the assimilation window increases, the background estimate and nonlinear model trajectory are updated. Improvement of the background

estimate and nonlinear model trajectory leads to a better analysis in the OUTER and QSVA experiments. Furthermore, as the length of the assimilation window increases in the QSVA experiment, the nonlinearity of the original minimization problem also increases because a high degree of nonlinearity usually results from a lengthy assimilation window, high resolution, etc.

Figure 4.9 shows the running time for the 4DVAR, OUTER, and QSVA experiments on a LINUX cluster with 8 Central Processing Units (CPUs) and 50-GB of memory². 21 iterations in the 4DVAR experiment take about 7.5 h of wall-clock time. In the OUTER experiment, 3 outer loops are used with 21, 26, and 26 inner-loop iterations, and a total of 73 iterations take approximately 27.25 h of wall-clock time. In the QSVA experiment, for each assimilation window, 12, 20, 22, and 25 iterations are required, respectively, with a total wall-clock time of approximately 12.95 h. The computational cost of the QSVA experiment is greater than that of the 4DVAR experiment, but it is much less

² In this study, data assimilation experiments are conducted on LINUX cluster system. This system contains Quad-Core AMD Opteron Processor 2376 HE, and it has a total of 8 CPUs. Its theoretical performance is about 73.6 GF (Giga Flops), and its memory is 8 GB. KMA's third supercomputer is based on CRAY XE6 system. It has a total of 90,240 CPUs (16-Core AMD Opteron Processor 6300) and 120-TB memory. Its theoretical performance is approximately 758 TF (Tera Flops), and hence the performance of the LINUX cluster system used in this study is not good compared to KMA's supercomputer. As another example, NCAR's supercomputer, Yellowstone has a total of 72,288 CPUs (8-Core Intel Xeon E5-2670 Processor), and its theoretical performance is about 1.5 PF (Peta Flops).

than that of the OUTER experiment, in which nonlinearity of the forecast model and observation operator is taken into account as in the QSVA experiment. This saving in computational time in the QSVA experiment is to the result of a shorter assimilation window of prior minimization tasks than in the 4DVAR or OUTER experiment. Generally, in operational environments, all the computations related to data assimilation are carried out after the so-called ‘cut-off-time’, i.e., after the end of the assimilation window. Therefore, the computational cost is concentrated near this cut-off-time. Through the QSVA method, some computations can be done before the cut-off-time, and hence the computational burden can be distributed efficiently (Järvinen et al., 1996). The computational cost required for the QSVA experiment can be reduced further by using different stopping-criterion in the minimization of the cost function in prior minimization tasks. In an additional experiment, QSVA_LC, the minimization of the cost function is finished when the gradient norm is reduced by just one order of magnitude when the length of the assimilation window is 0, 10, or 20 minutes. Since the final minimization task (i.e., when the length of the assimilation window is 30 minutes) is of main concern, the prior minimization tasks need not to be solved precisely, and hence this method to reduce the computational cost can be justified. It is known that the minimization process

acts on the largest scale first (Thépaut and Courtier, 1991; Navon et al., 1992; Tanguay et al., 1995), and hence this method enables the large scale to be resolved by prior minimization tasks, then the small scales to be sought for only during the final minimization task. In the QSVA_LC experiment, a total of $(6+12+12+25=)$ 55 iterations take about 12.05 h of wall-clock time, representing a saving of approximately 1-h compared to the QSVA experiment. Note that the quality of the analysis and subsequent forecast in the QSVA_LC experiment is very similar to those in the QSVA experiment (not shown).

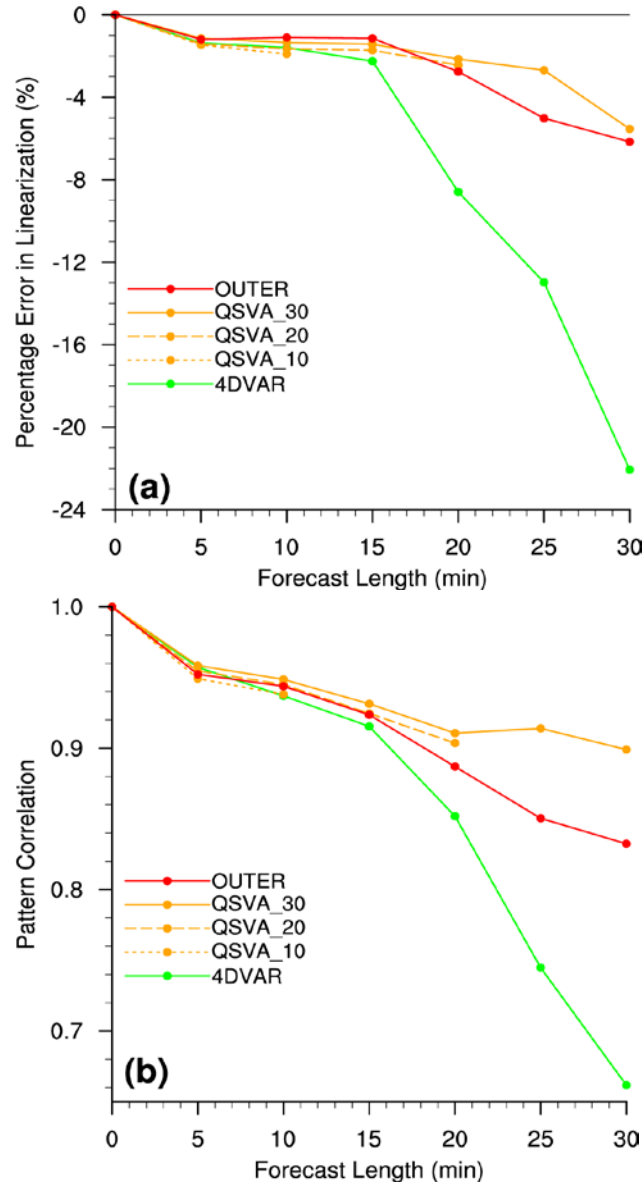


Figure 4.8. (a) Percentage error in linearization (%) and (b) pattern correlation as a function of forecast length for the 4DVAR (green solid line), QSVA_10 (orange dotted line), QSVA_20 (orange dashed line), QSVA_30 (orange solid line), and OUTER (red solid line) experiments.

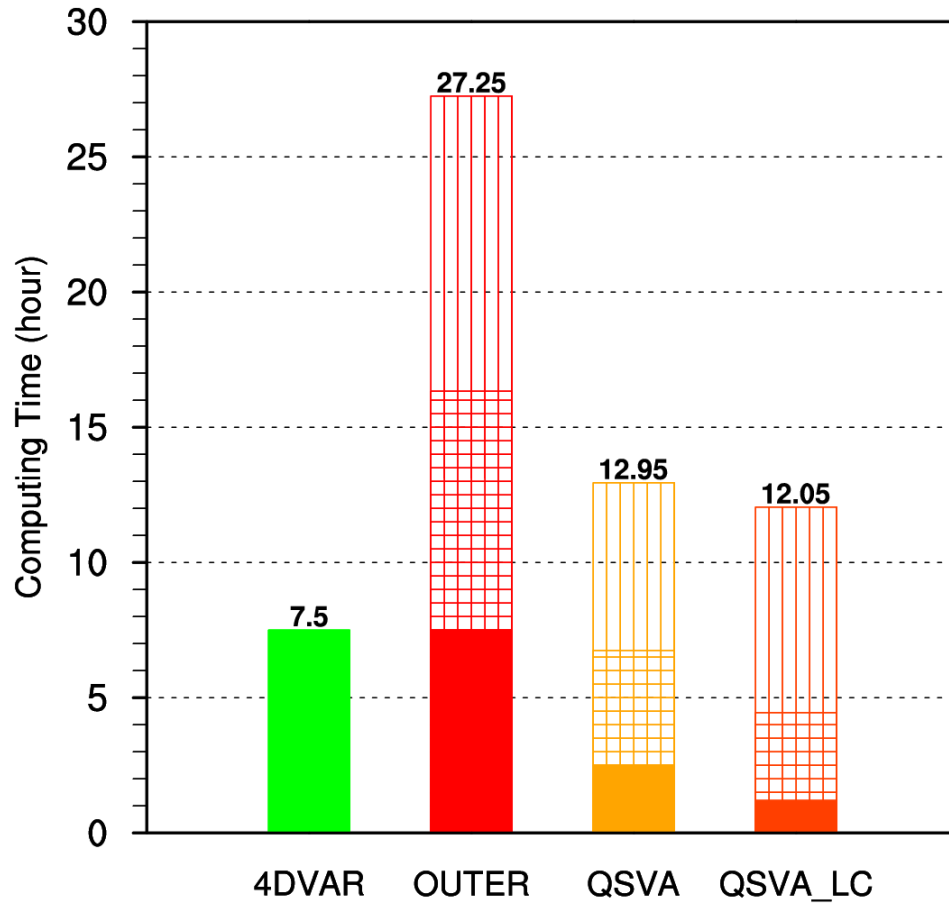


Figure 4.9. Computing time (hour) for the 4DVAR, OUTER, QSVA, and QSVA_LC experiments. In the OUTER experiment, computing times for the first, second, and third outer loop are shown. In the QSVA and QSVA_LC experiments, computing times for assimilation tasks with assimilation window of 10, 20, and 30 minutes are shown. Note that computing time for assimilation task with assimilation window of 0 minute is less than one minute.

Figure 4.10 shows the 6-h accumulated rainfall distributions from 0600 UTC to 1200 UTC 6 August 2006 for the CONTROL, 3DVAR, 4DVAR, OUTER, and QSVa experiments. In the observations, there were two localized rainfall maxima: one over the southwestern part of the Korean Peninsula and the other over the east coast, as mentioned in section 4.1. The 6-h accumulated rainfall amount was 33.5 mm at Namwon and it was 37.5 mm at Taebaek. In the CONTROL experiment, there is rainfall over the southwestern part of the Korean Peninsula with maximum rainfall amount of about 62.9 mm (Fig. 4.10a). However, rainfall distribution is too localized to be regarded as rainfall caused by an organized system, and the 6-h accumulated rainfall amount is overestimated compared to the observations. When the radar radial velocity data are assimilated using the 3D-Var method, no significant improvement in rainfall distribution can be found compared to the CONTROL experiment (Fig. 4.10b). In the 4DVAR experiment, rainfall distribution over the southwestern part of the Korean Peninsula is relatively well simulated compared to the CONTROL and 3DVAR experiments. However, the 6-h accumulated rainfall amount at the maximum rainfall point (~155.8 mm) is highly overestimated compared to the observations, and the rainfall distribution incorrectly extends to the central part of South Korea. In addition, rainfall over the east coast is not

simulated at all in the 4DVAR experiment (Fig. 4.10c). Rainfall distribution in the OUTER experiment is similar to that in the 4DVAR experiment, but the 6-h accumulated rainfall amount in the OUTER experiment is even greater than that in the 4DVAR experiment (Fig. 4.10d). The 6-h accumulated rainfall distribution in the QSVA experiment is similar to the observations. Both of the localized rainfall maxima in the observations are simulated in the QSVA experiment although the localized rainfall maximum over the east coast, which corresponds to Taebaek, is displaced eastward compared to the observations. The 6-h accumulated rainfall amount at the maximum point over the southwestern part of the Korean Peninsula, which corresponds to Namwon, is approximately 34.2 mm, and that over the east coast is approximately 31.7 mm in the QSVA experiment (Fig. 4.10e). Both of them are similar to the observations.

The time series of the hourly rainfall at Namwon and Taebaek (or at the grid points corresponding to Namwon and Taebaek in the case of the model experiments) from 0600 UTC to 1200 UTC 6 August 2006 for the CONTROL, 3DVAR, 4DVAR, OUTER, and QSVA experiments are shown in Figs. 4.1a and b along with the observations. At Namwon, the observed rainfall peaked at 1000 UTC with rainfall amount of 30.5 mm, and the rainfall was concentrated

around the peak time. In the CONTROL and 3DVAR experiments, the rainfall peak appears at 0800 UTC, and the rainfall amount at the peak time is approximately 47.9 mm and 59.1 mm, respectively. The peak time is earlier than the observations, and in these experiments the rainfall amount at the peak time is overestimated compared to the observations. In the 4DVAR experiment, the rainfall peaks at 1000 UTC with rainfall amount of about 78.2 mm. Although the peak time is well simulated, the rainfall amount at the peak time is highly overestimated compared to the observations. This is consistent with the result of the 6-h accumulated rainfall distribution shown in Fig. 4.10c. The simulated hourly rainfall amount in the OUTER experiment is greater than 20.0 mm after 0900 UTC, which is different from the observations. The rainfall peak appears at 0900 UTC (earlier than the observations) with rainfall amount of 47.8 mm (overestimated) in the OUTER experiment. In the QSVA experiment, hourly rainfall peaks at 1000 UTC, which is identical to the observations, although the rainfall amount at the peak time (~21.9 mm) is slightly underestimated compared to the observations. At Taebaek, in the observations, rainfall was concentrated around the peak time, 0800 UTC, with rainfall amount of about 34.0 mm. The rainfall maximum at Taebaek is simulated only in the QSVA experiment, as shown in Fig. 4.10. In the QSVA experiment,

rainfall peaks at 0800 UTC like the observations in spite of an underestimation of the rainfall amount at the peak time (~24.6 mm).

Figure 4.11 shows RMSEs of rainfall as a function of forecast time for CONTROL, 3DVAR, 4DVAR, OUTER, and QSVA experiments. For the first 2-h forecast, RMSEs of rainfall of 4DVAR and OUTER experiments are the largest because rainfall is wrongly simulated over the central part of South Korea in 4DVAR and OUTER experiments. Simulated rainfall over the southwestern part of the Korean Peninsula in CONTROL and 3DVAR experiments is earlier than the observations in timing, and hence RMSEs of CONTROL and 3DVAR experiments are also large during this period. For the second 2-h forecast, RMSEs of rainfall of 4DVAR and OUTER experiments are the largest due to the overestimation of rainfall over the southwestern part of the Korean Peninsula during this period. RMSEs of CONTROL and 3DVAR experiments are also large because the observed rainfall over the southwestern part of the Korean Peninsula is missed in CONTROL and 3DVAR experiments. In contrast, RMSE of QSVA experiment during this period is relatively small since the observed rainfall over the southwestern part of the Korean Peninsula is simulated well in QSVA experiment. For 6-h forecast, although 6-h accumulated rainfall distributions of 4DVAR and OUTER experiments are

better than those of CONTROL and 3DVAR experiments in a certain manner (e.g., forecast of rainfall over the southwestern part of the Korean Peninsula), RMSEs of rainfall of 4DVAR and OUTER experiments are larger than those of CONTROL and 3DVAR experiments. This is due to the overestimation of rainfall over the southwestern part of the Korean Peninsula and false simulation of rainfall over the central part of South Korea. RMSE of rainfall of QSVa experiment is the smallest among all the experiments, and this is consistent with the qualitative analyses of simulated rainfall (e.g., distribution and time series of rainfall).

RMSEs of radial velocity as a function of forecast time for CONTROL, 3DVAR, 4DVAR, OUTER, and QSVa experiments are shown in Fig. 4.12. Error is defined as the difference between observed radial velocity from 13 radar observation sites over the Korean Peninsula and simulated radial velocity derived from simulated wind components. RMSE of radial velocity of CONTROL experiment increases with increasing forecast time. On the whole, RMSEs of data assimilation experiments are smaller than that of CONTROL experiment during 6-h forecast. However, in 3DVAR experiment, RMSE of radial velocity increases rapidly during the period from 0800 UTC to 0930 UTC, which is related to rainfall over the southwestern part of the Korean Peninsula,

and at 1200 UTC, the difference in RMSE between CONTROL and 3DVAR experiments is not large. In 4DVAR, OUTER, and QSVA experiments, RMSE of radial velocity is the smallest in the middle of 30-minute assimilation window, and this is consistent with previous studies (Pires et al., 1996; Swanson and Vautard, 1998). RMSEs of radial velocity of 4DVAR, OUTER, and QSVA experiments remain relatively small compared to CONTROL and 3DVAR experiments during the whole forecast. Among 4DVAR, OUTER, and QSVA experiments, RMSE of QSVA experiment is the smallest.

Fit to the observations (i.e., bias) of zonal wind, meridional wind, temperature, and water vapor mixing ratio for CONTROL, 3DVAR, 4DVAR, OUTER, and QSVA experiments are shown in Fig. 4.13. Fit to the observations is calculated using sounding observations from 7 radiosonde observation sites over the Korean Peninsula at 1200 UTC 6 August 2006. In CONTROL experiment, negative bias of zonal wind appears below 800 hPa, positive bias appears between 800 hPa and 600 hPa, and again negative bias appears above 600 hPa except for 200 hPa. These biases in CONTROL experiment are reduced in data assimilation experiments, especially in QSVA experiment and at mid-levels. Bias of meridional wind is negative almost at all pressure levels in CONTROL experiment. Through assimilation of radar data, bias of meridional wind is

reduced at all levels except for above 300 hPa. Among data assimilation experiments, decrease in bias of meridional wind is the largest in OUTER and QSVA experiments. Bias of temperature is the largest at lower levels, it is close to zero at mid-levels, and it is slightly negative at upper levels. Positive bias of temperature below 800 hPa in CONTROL experiment is lessened only in QSVA experiment. Bias of water vapor mixing ratio is positive at all levels except for 450 hPa in CONTROL experiment. Below 900 hPa, bias of water vapor mixing ratio in QSVA experiment is negative, which is different from the other experiments. Positive bias of water vapor mixing ratio between 800 hPa and 500 hPa is reduced in data assimilation experiments, and decrease in bias is the largest in QSVA experiment.

In order to figure out the reason why the rainfall forecast of the QSVA experiment is different from that of the 4DVAR (or OUTER) experiment, analysis increments of the 4DVAR and QSVA experiments are investigated. Figure 4.14 shows analysis increments of the horizontal wind, divergence, and CAPE at 850 hPa for the 4DVAR and QSVA experiments with the corresponding background fields. In the CONTROL experiment (i.e., in background fields), CAPE over the southern part of the Korean Peninsula is greater than 1500 J kg^{-1} , and the water vapor mixing ratio is also large over

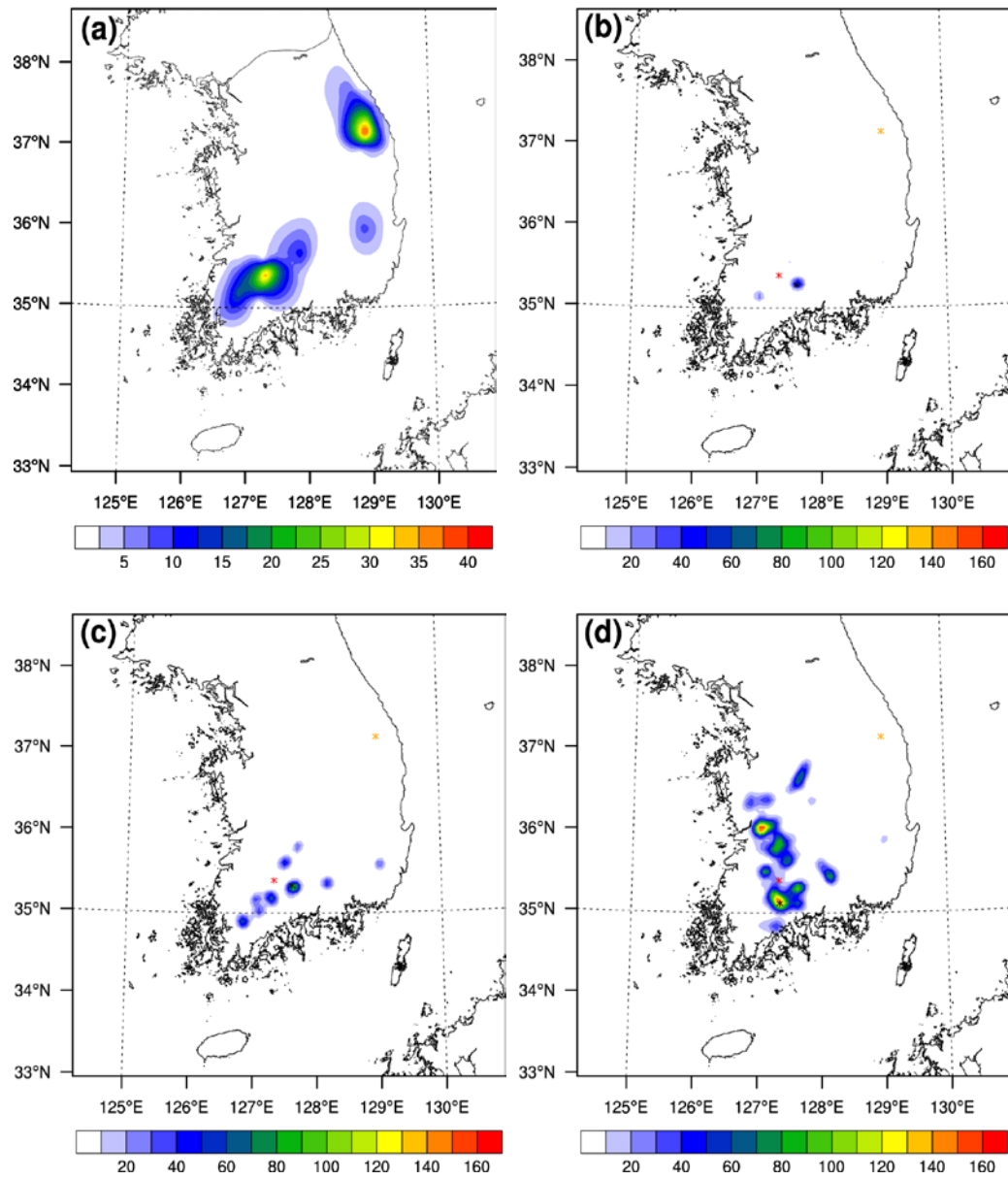
South Korea. However, in the CONTROL experiment, the rainfall distribution is too localized to be considered as rainfall caused by an organized system (Fig. 4.10a). In the CONTROL experiment, the horizontal wind over the Yellow Sea and the Korean Peninsula is anti-cyclonic, and divergence is dominant over the southern part of the Korean Peninsula (Fig. 4.14a). As a result, there is not enough lift forcing in the CONTROL experiment, which is necessary in simulating rainfall over the southwestern part of the Korean Peninsula. Incremental wind of the 4DVAR experiment is cyclonic and convergent over the Yellow Sea and the southwestern part of the Korean Peninsula. In particular, the analysis increment of convergence is maximized near Namwon (Fig. 4.14b). Consequently, through the assimilation of radial velocity data using the 4D-Var method, the horizontal wind over the southwestern part of the Korean Peninsula is modified, and this modification provides continuous forcing for lift, which is necessary for simulating rainfall centered at Namwon. However, simulated rainfall over the southwestern part of the Korean Peninsula is highly overestimated, and it extends erroneously to the central part of South Korea in the 4DVAR experiment. This is because the analysis increment of CAPE over the western part of the Korean Peninsula is positive, and excessive convective instability is simulated over that region. Incremental wind in the QSV

experiment over the southwestern part of the Korean Peninsula is cyclonic and convergent as in the 4DVAR experiment. In contrast to the 4DVAR experiment, however, the analysis increment of CAPE over the western part of the Korean Peninsula is negative, and this improves the rainfall forecast over the southwestern part of the Korean Peninsula in the QSVA experiment. It is also noted that in the QSVA experiment, the analysis increment of CAPE over the east coast is positive, and this may enable the simulation of the observed rainfall near Taebaek (Fig. 4.14c).

Vertical cross sections of the vertical wind and divergence, and equivalent potential temperature and reflectivity along the line in Fig. 4.10d at 0900 UTC 6 August 2006 are shown in Figs. 4.15a and b. A convective system characterized by a strong upward motion can be found in the vertical cross section of the vertical wind and divergence for the QSVA experiment. The upward motion extends to near the tropopause with a maximum value of approximately 2 m s^{-1} at a height of about 8 km. This upward motion is related to convergence at lower levels and divergence at upper levels. These features are consistent with the observations shown in Fig. 4.3b. In the vertical cross section of the equivalent potential temperature and reflectivity, high values ($> 40 \text{ dBZ}$) of the reflectivity correspond well to the strong upward motion. The

equivalent potential temperature decreases by approximately 10 K, going from 2 km to 8 km, and this implies conditional instability. Note that near the convection center, the decrease in the equivalent potential temperature is not significant because the conditional instability is partly relieved by the convective system. The improvement of the analysis shown in Fig. 4.14, especially of the wind fields, leads to a better forecast of rainfall and meteorological fields in the QSVA experiment.

Figure 4.15c shows the skew T-log p diagram at the grid point corresponding to Gwangju at 0900 UTC 6 August 2006 in the QSVA experiment. Compared to the observations at 0600 UTC in Fig. 4.2a, development of the vertical structure of the temperature and dew-point temperature are simulated well. In addition, there is a Moist Absolutely Unstable Layer (MAUL) near 850 hPa, which is frequently observed in the developing stage of many MCSs and lasts throughout their mature stage (Bryan and Fritsch, 2000). The simulated value of CAPE is approximately 2564 J kg^{-1} , which is reasonable when the observed value of 1970 J kg^{-1} at 0600 UTC is considered (Table 4.1). These results indicate that the vertical structure of the thermodynamic fields over the southwestern part of the Korean Peninsula is reproduced well in the QSVA experiment.



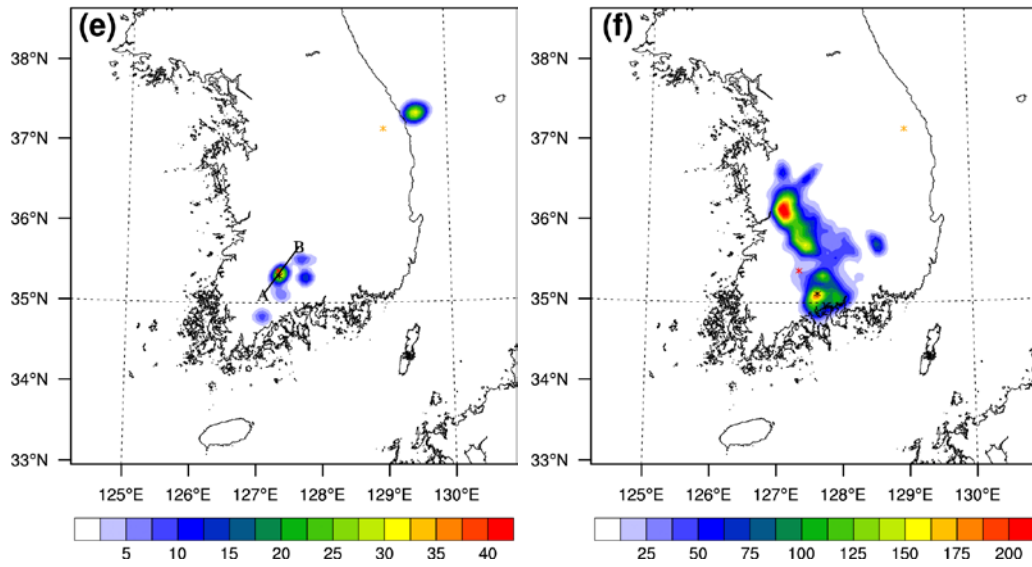


Figure 4.10. 6-h accumulated rainfall ($\text{mm } 6\text{h}^{-1}$) distribution over South Korea from 0600 UTC to 1200 UTC 6 August 2006 for the (a) observations, (b) CONTROL, (c) 3DVAR, (d) 4DVAR, (e) QSVa, and (f) OUTER experiments. Note that different color scales are used for the QSVa and OUTER experiments.

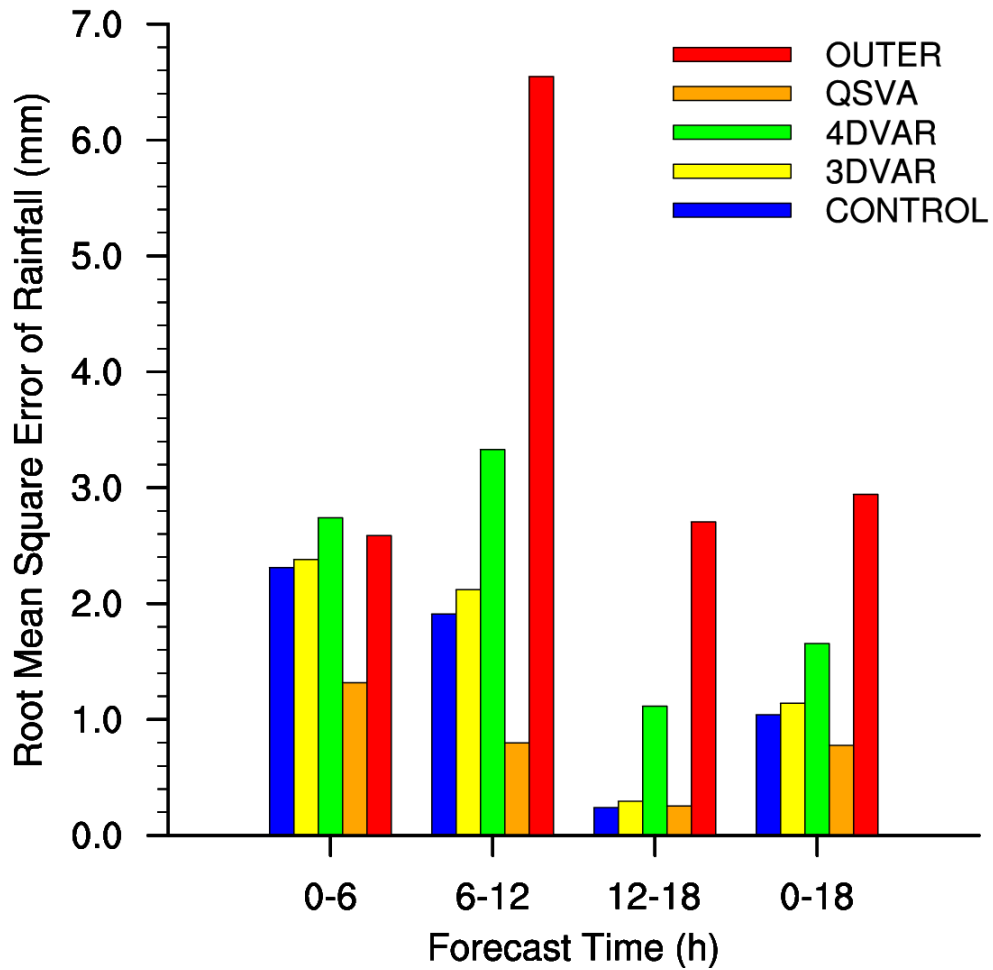


Figure 4.11. Root Mean Square Errors (RMSEs) of rainfall ($\text{mm } 6\text{h}^{-1}$) as a function of forecast time for the CONTROL (blue), 3DVAR (yellow), 4DVAR (green), QSVA (orange), and OUTER (red) experiments. Surface observations from 76 observation sites over South Korea are used.

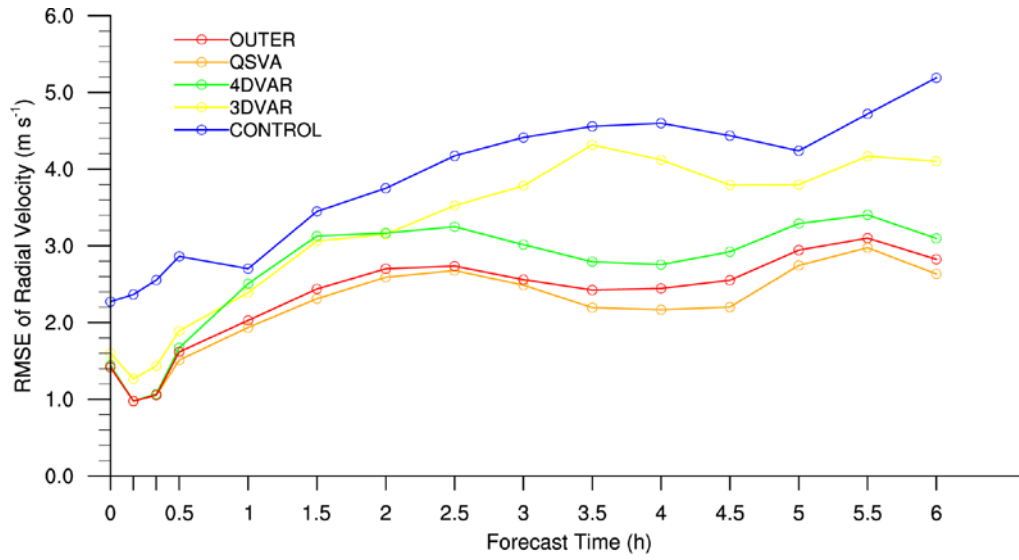


Figure 4.12. Root Mean Square Errors (RMSEs) of radial velocity (m s^{-1}) as a function of forecast time for the CONTROL (blue), 3DVAR (yellow), 4DVAR (green), QSVA (orange), and OUTER (red) experiments. Radial velocity observations from 13 radar observation sites over the Korean Peninsula are used.

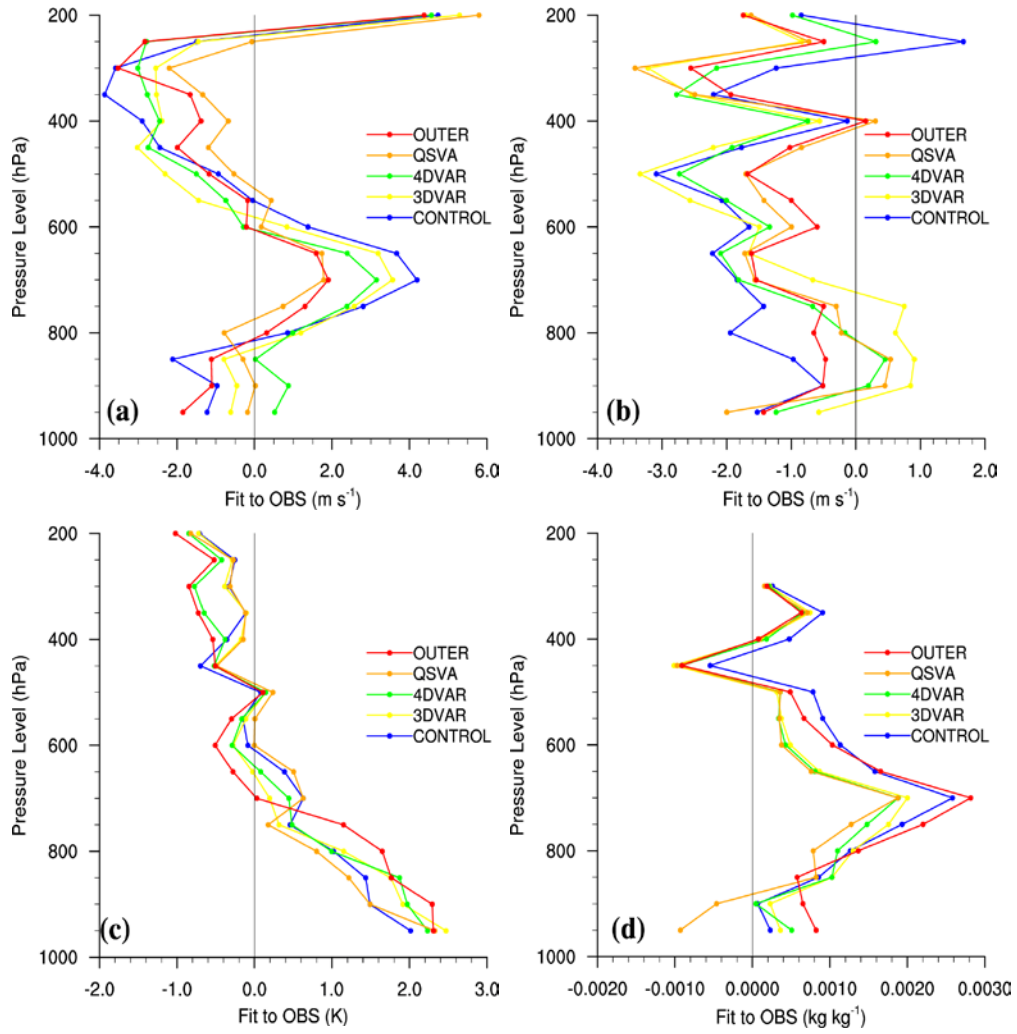


Figure 4.13. Vertical distribution of fit to the observations using sounding observations over the Korean Peninsula at 1200 UTC 6 August 2006 for the CONTROL (blue), 3DVAR (yellow), 4DVAR (green), QSVA (orange), and OUTER (red) experiments. (a) Zonal wind (m s^{-1}), (b) meridional wind (m s^{-1}), (c) temperature (K), and (d) water vapor mixing ratio (kg kg^{-1}).

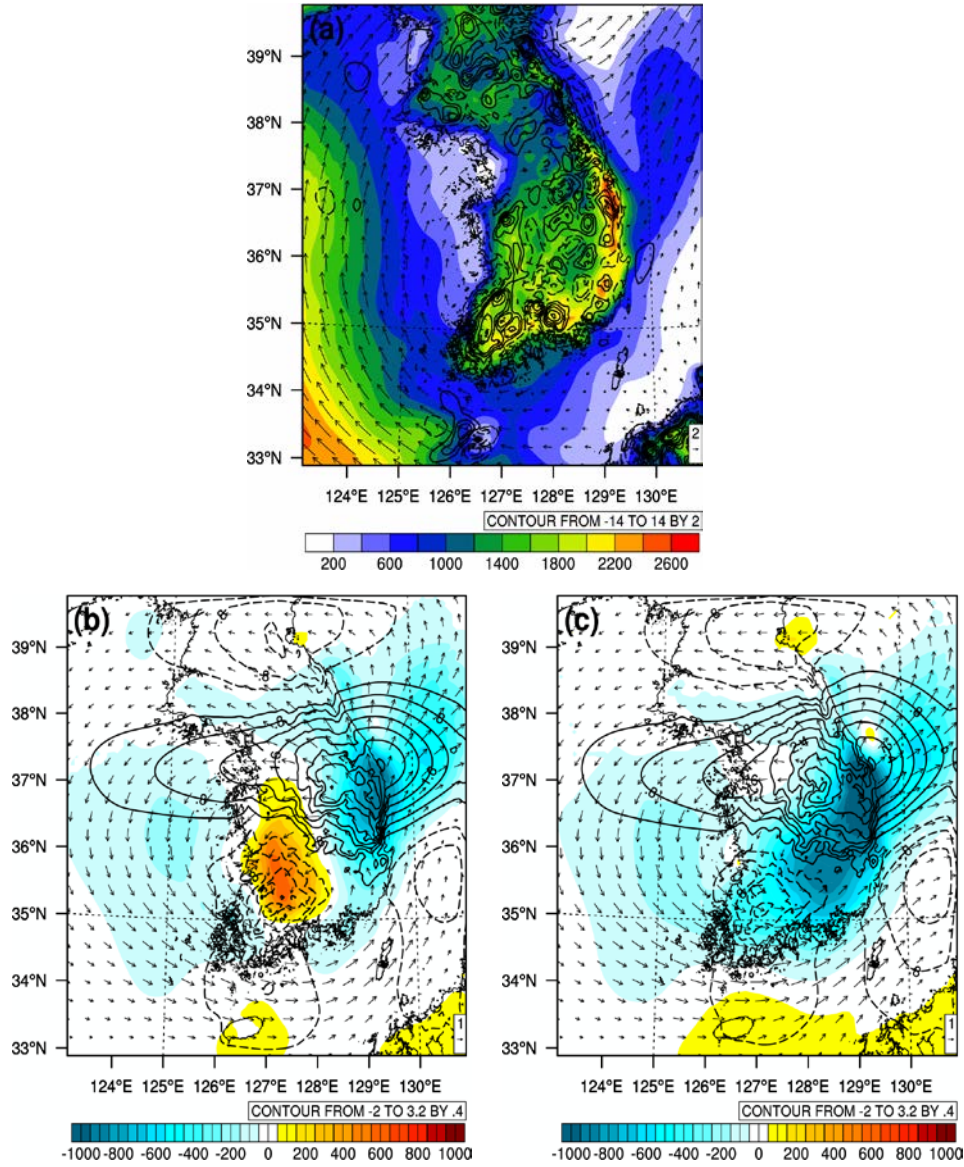


Figure 4.14. (a) Convective Available Potential Energy (CAPE, J kg^{-1} , shading), divergence (10^{-5} s^{-1} , negative values are denoted by dashed contours), and winds (m s^{-1} , vector) of 850 hPa at 0600 UTC 6 August 2006 for the CONTROL experiment. Analysis increments of CAPE (J kg^{-1} , shading), divergence (10^{-5} s^{-1} , negative values are denoted by dashed contours), and winds (m s^{-1} , vector) at 850 hPa for the (b) 4DVAR and (c) QSVA experiments.

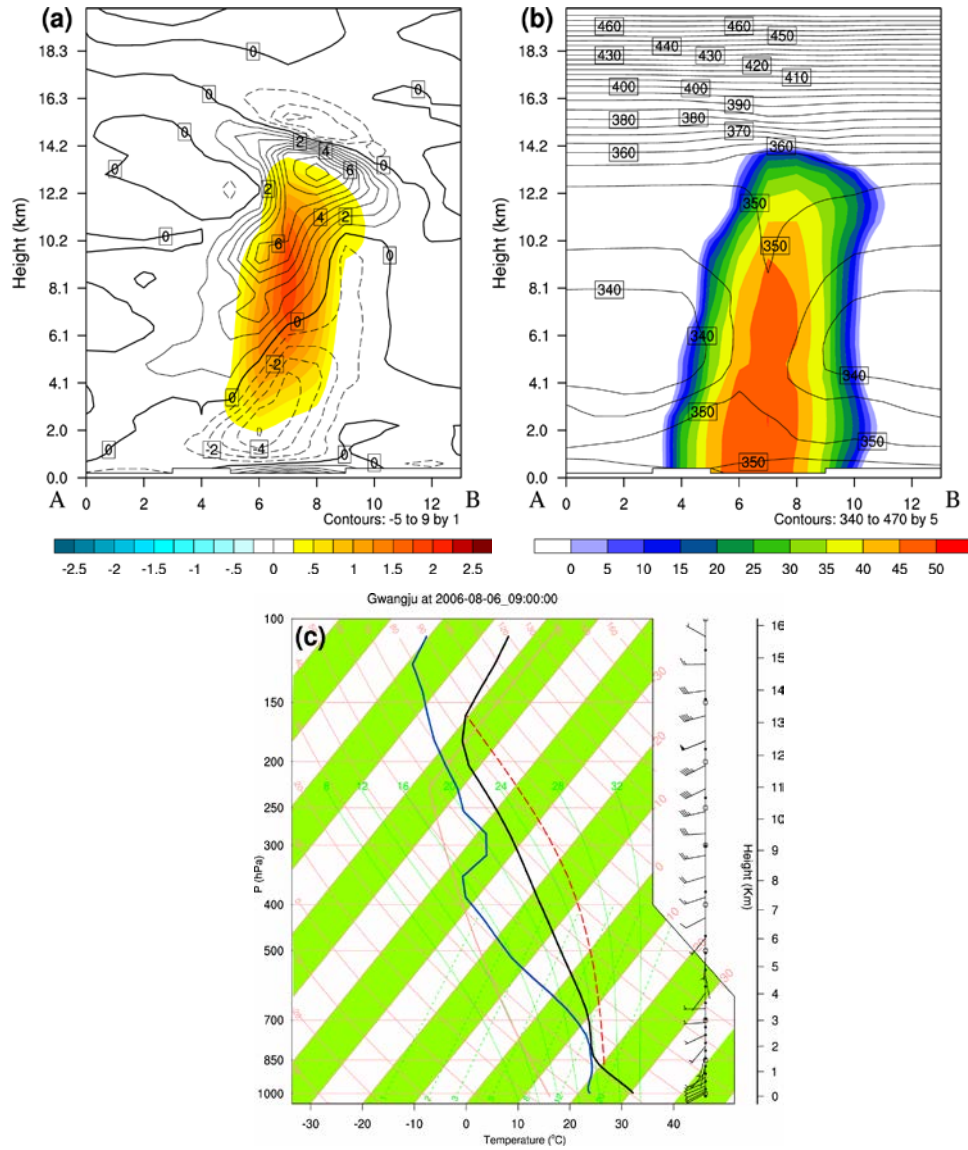


Figure 4.15. Vertical cross section along the line in Fig. 4.10d of (a) vertical wind (m s^{-1} , shading) and divergence (10^{-4} s^{-1} , negative values are denoted by dashed contours) and (b) reflectivity (dBZ, shading) and equivalent potential temperature (K, contour interval of 5 K) at 0900 UTC 6 August 2006. (c) Skew T-log p diagram of Gwangju for the QSVA experiment at 0900 UTC 6 August 2006.

In summary, incremental wind of the 4DVAR (or OUTER) and QSVA experiments is cyclonic and convergent over the southwestern part of the Korean Peninsula, and this modification to the wind field provides forcing for lift, which is essential in simulating rainfall near Namwon. However, in the 4DVAR (or OUTER) experiment, the analysis increment of CAPE over the western part of the Korean Peninsula is positive, and this results in excessive rainfall over the western part of the Korean Peninsula compared to the observations. In contrast, a negative (positive) increment of CAPE over the western part (east coast) of the Korean Peninsula in the QSVA experiment leads to better forecasts of rainfall and meteorological fields.

The analyses of both the OUTER and QSVA experiments are better than the 4DVAR experiment, but the rainfall forecast of only the QSVA experiment is improved. In the OUTER experiment, a 30-minute assimilation window is used in the inner-loop minimizations of all the outer loops. However, in the QSVA experiment, the length of the assimilation window is increased gradually from 0-minute to 30-minute in 10-minute interval, and the nonlinearity of the original minimization problem is increased accordingly. Therefore, the relatively-low-quality background estimate is used when the nonlinearity (and chance of multiple minima) of the nonlinear minimization problem is comparatively low,

and vice versa. In other words, by increasing the length of the assimilation window step by step, the orbit minimizing the cost function is determined at each step, and that orbit is used as the starting point for the next minimization in the QSVA method. This quasi-static adjustment ensures that the computed minimum at every step is the absolute minimum, and the starting point of the minimization of the cost function always lies within the attractive basin of the absolute minimum of the next minimization (Pires et al., 1996). Although it is not possible to show that the analysis of the QSVA experiment is closer to the global minimum than that of the OUTER (or 4DVAR) experiment, this may be convinced indirectly by the improved forecasts of the QSVA experiment.

4.4. Extension to heavy rainfall cases in 2006 and 2008

In order to obtain robustness of the conclusion drawn in section 4.3, a total of 9 heavy rainfall cases over the Korean Peninsula are selected. Data assimilation and forecast results from these 9 cases are analyzed and compared to the heavy rainfall case in section 4.3. Selected 5 heavy rainfall cases occurred in 2006 (including the heavy rainfall case in section 4.3) and 5 heavy rainfall cases

occurred in 2008 are summarized in Table 4.4. 24-h accumulated rainfall distributions for 9 heavy rainfall cases (excluding Case 4; refer to Fig. 4.1a of section 4.3) are shown in Figs. 4.16 and 17.

In Case 1, rainfall was broadly distributed over South Korea, and it was locally-concentrated over the central part and south coast of the Korean Peninsula. 24-h accumulated rainfall amount was maximized at Ganghwa, west of Seoul, and rainfall amount was approximately 153.0 mm. Rainfall was induced by the low-pressure system developing over the Central China and passing through the southern part of the Korean Peninsula. In Case 2, main rainfall band was line-shaped, and 24-h accumulated rainfall amount at Seosan was about 95.5 mm. This case was related to upper-level trough located over the northern part of the Korean Peninsula. Rainfall in Case 3 was caused by typhoon EWINIAR. Rainfall was concentrated over the south coast of South Korea, and 24-h accumulated rainfall amount at Namhae was approximately 264.5 mm. In Case 5, cold and moist air over the northern East Sea was transported to the east coast of South Korea by northeasterly flow. This cold and moist air was lifted by Taebaek Mountains parallel to the east coast, and a large amount of orographic rainfall was induced over Youngdong areas. 24-h accumulated rainfall amount at Gangneung was about 292.5 mm.

In Case 6, interaction between upper-level trough and surface disturbance induced heavy rainfall over the broad areas of the Korean Peninsula. 24-h accumulated rainfall amount at Seogwipo (in Jeju Island) was approximately 214.5 mm. In Case 7, a blocking-high was located over the areas north of Japan, and cold air was surged to the Korean Peninsula at upper levels. This synoptic environment caused the atmosphere over the Korean Peninsula to be convectively unstable, and finally, induced torrential rainfall and lightning. 24-h accumulated rainfall distribution was line-shaped, and it was maximized at Seoul with rainfall amount of about 80.5 mm. Rainfall in Case 8 and 9 was induced by Jangma front, and it was concentrated over the central part of the Korean Peninsula. 24-h accumulated rainfall amount at Hongcheon (Paju) was 108.5 mm (282.5 mm) in Case 8 (Case 9). Finally, in Case 10, rainfall was induced by mid-level trough, and rainfall was concentrated over the central part and south coast of the Korean Peninsula. 24-h accumulated rainfall amount at Yanggu was approximately 121.5 mm.

A total of 4 experiments are conducted for each case: CONTROL, 4DVAR, OUTER, and QSVA experiments. In CONTROL experiment, no radar data are assimilated. In 4DVAR, OUTER, and QSVA experiments, radar radial velocity data are assimilated using the 4D-Var (with single outer loop), 3 outer-loop 4D-

Var, and QSVA methods, respectively. Like in section 4.3, initial condition of CONTROL experiment is used as a first guess for data assimilation experiments (i.e., cold-start). Background error covariance is calculated by using the NMC method, and radar data are preprocessed before the assimilation. Assimilation window starts at the initial time of domain 3 and its length is 30 minutes. Results of additional 9 cases are compared to that of Case 4 in section 4.3. It should be noted that radar data from USAF, which are known to be effective in data assimilation, are available only for Cases 1-5.

Figure 4.18 shows normalized cost-function values as a function of iteration number for heavy rainfall cases in 2006 (i.e., Cases 1-5). In order to be compared with 4DVAR experiment, OUTER experiment refers to minimization of cost function for the third outer-loop, and QSVA experiment refers to minimization of cost function for assimilation window of 30-minute. In 4DVAR experiments, minimizations of cost function for all the cases are converged successfully after several tens of iterations. After minimization, cost function decreases to less than 50% of its starting value, especially, in Case 5, its ending value is less than 20% of the starting value (Fig. 4.18a). When inner-loop minimization for the third outer-loop is considered (Fig. 4.18b), ending values of normalized cost function for all the cases are relatively large compared to

4DVAR experiment. This implies that decreasing rate of cost function is not large, and hence ratio between starting and ending values of the cost function remains large in spite of greater number of iterations in OUTER experiment. In OUTER experiments, first guess is updated progressively through the use of outer-loop, which results in relatively-slow rate of convergence in minimization of cost function. In terms of both total number of iterations and ending value of cost function, minimization of cost function in QSVA experiment is between 4DVAR and OUTER experiments (Fig. 4.18c). Total number of iterations for Case 3 is the greatest in all the experiments, and decreasing rate of cost function for Case 1 is relatively large even in OUTER and QSVA experiments.

Normalized cost functions for heavy rainfall cases in 2008 (i.e., Cases 6-10) are shown in Fig. 4.19. Minimization of cost function in 4DVAR experiment for Cases 6-10 is converged after 19, 7, 40, 41, and 21 iterations, respectively. The ending value of cost function is approximately 0.3 for Cases 8, 9, and 10, and it is less than 0.2 for Cases 6 and 7 (Fig. 4.19a). In OUTER experiment, more iterations (36, 11, 58, 65, and 44 iterations for Cases 6-10) are needed for convergence of cost-function minimization, and the ending value of cost function is relatively large compared to 4DVAR experiment. Like in 4DVAR experiment, the number of total iteration for Case 9 is the greatest, and the

ending value of the cost function for Case 6 is the smallest (Fig. 4.19b). Unlike the heavy rainfall cases in 2006, total number of iterations in QSVA experiment is greater than those in OUTER experiment except for Case 10. In addition, decrease in cost-function value in QSVA experiment is not much different from OUTER experiment as opposed to heavy rainfall cases in 2006 (Fig. 4.19c).

Table 4.4. Summary of heavy rainfall cases in 2006 and 2008.

	Initial time for domain 3 (YYYYMMDDHH , UTC)	Forecast length for domain 3 (h)	Maximum point of 24-h (or 6-h) accumulated rainfall amount	24-h (or 6-h) accumulated rainfall amount at maximum point (mm)
Case 1	2006050512	24	Ganghwa	153.0
Case 2	2006060918	24	Seosan	95.5
Case 3	2006070918	24	Namhae	264.5
Case 4	2006080606	6	Namwon	33.5
Case 5	2006102218	24	Gangneung	292.5
Case 6	2008052712	24	Seogwipo	214.5
Case 7	2008060200	24	Seoul	80.5
Case 8	2008071200	24	Hongcheon	108.5
Case 9	2008072312	24	Paju	282.5
Case 10	2008081112	24	Yanggu	121.5
	Peak time in time series of hourly rainfall at maximum point (UTC)	Peak hourly rainfall amount at maximum point (mm)	Characteristics	
Case 1	1700 UTC 05	23.5	Low pressure	
Case 2	0100 UTC 10	27.0	Trough	
Case 3	0100 UTC 10	36.5	Typhoon	
Case 4	1000 UTC 06	30.5	Thunderstorm	
Case 5	0200 UTC 23	64.5	Orographic rain	
Case 6	0300 UTC 28	30.5	Trough	
Case 7	1100 UTC 02	38.0	Thunderstorm	
Case 8	2000 UTC 12	29.0	Jangma front	
Case 9	2000 UTC 23	55.0	Jangma front	
Case 10	0700 UTC 12	18.0	Trough	

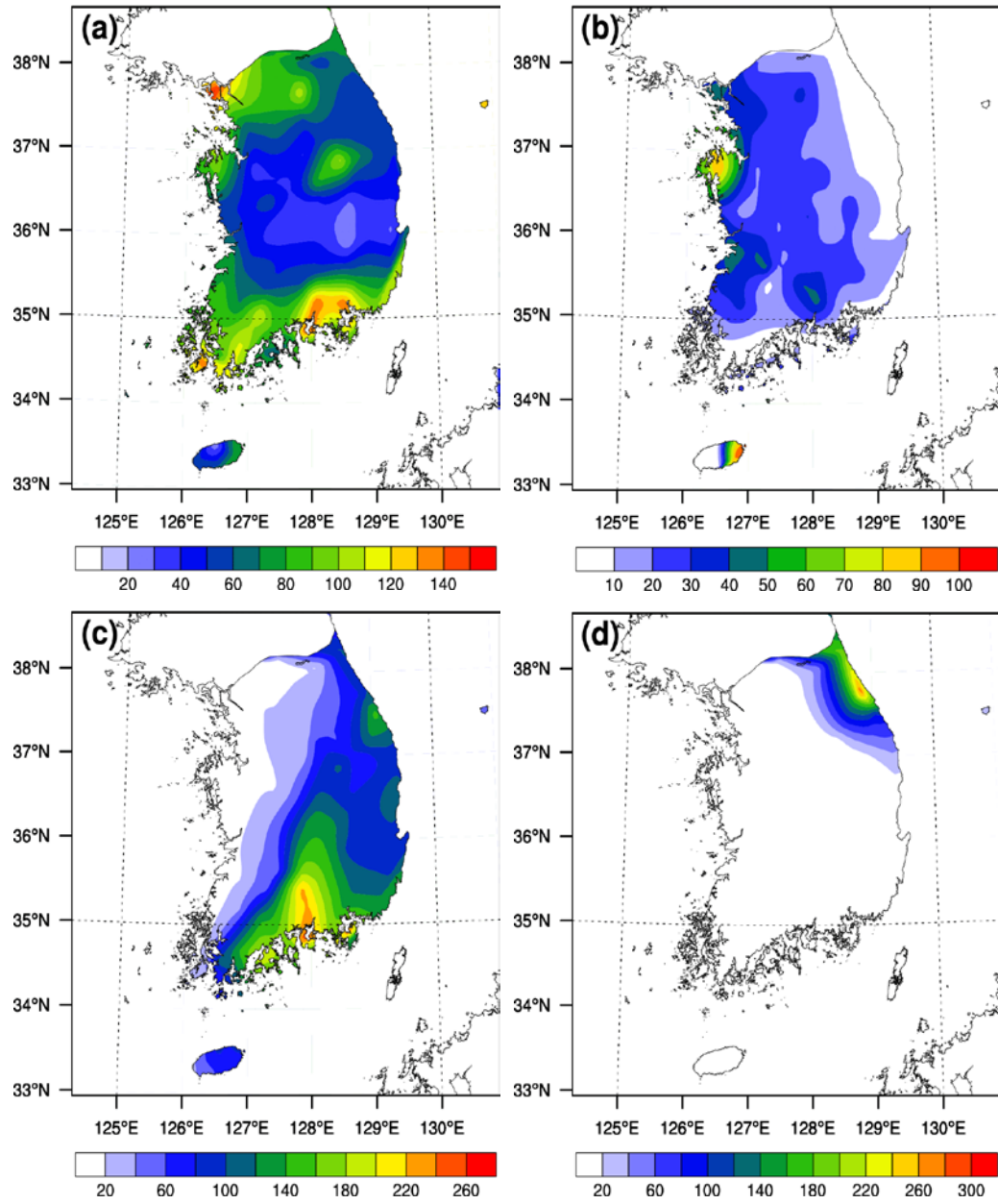
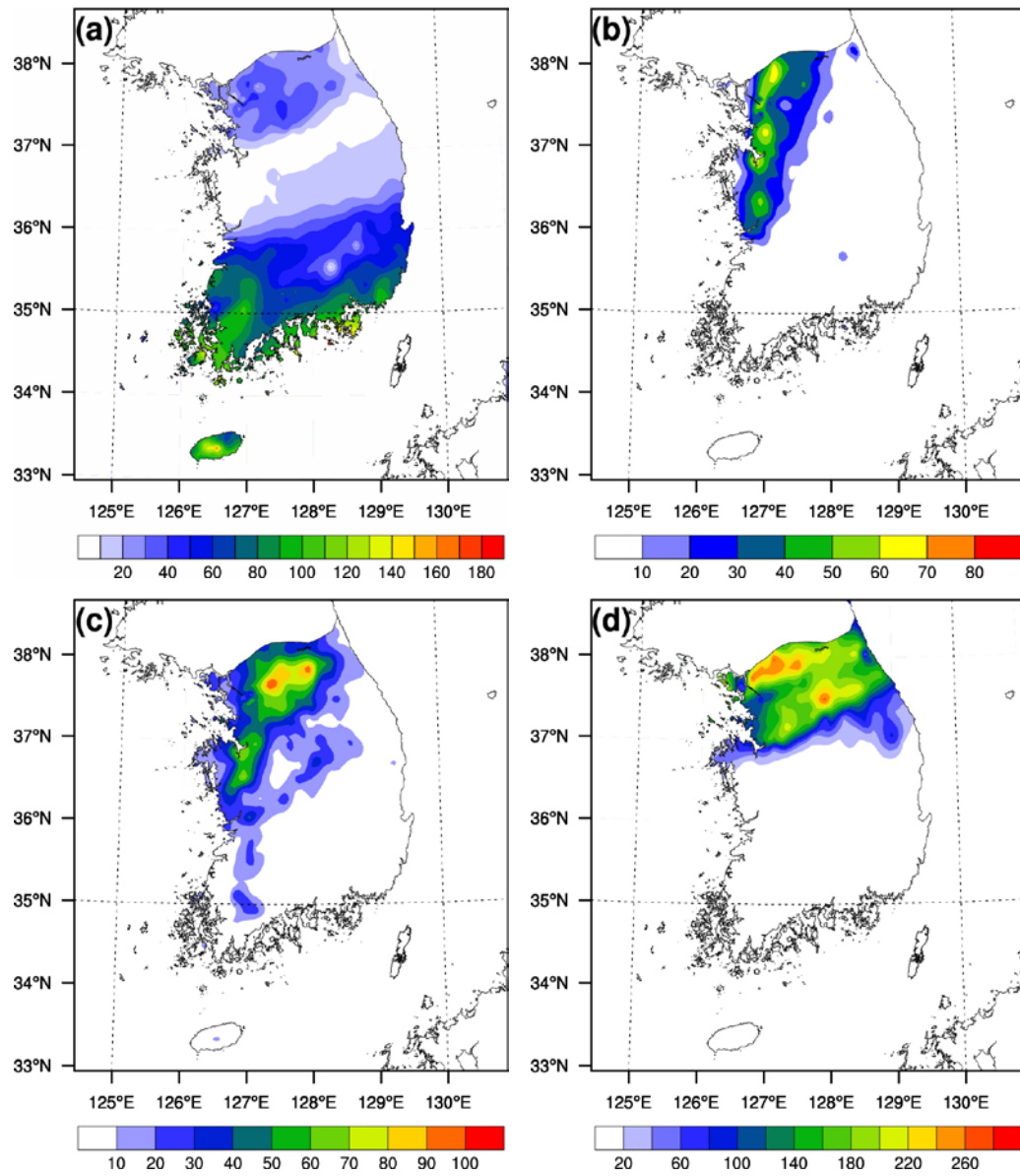


Figure 4.16. Observed 24-h accumulated rainfall distribution (mm 24h⁻¹) for (a) Case 1, (b) Case 2, (c) Case 3, and (d) Case 5.



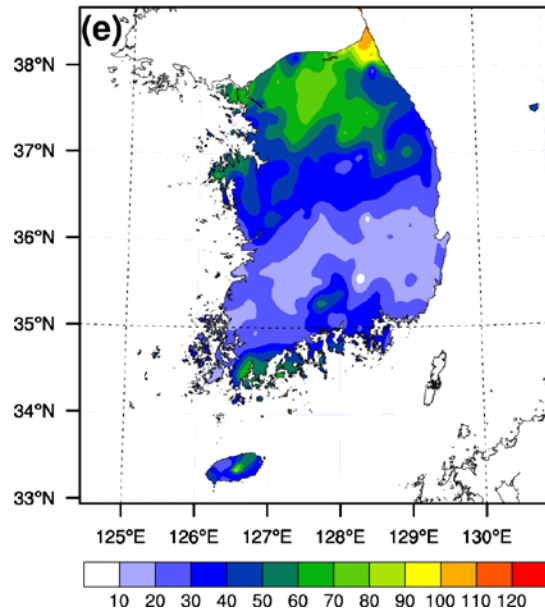


Figure 4.17. Observed 24-h accumulated rainfall distribution (mm 24h⁻¹) for (a) Case 6, (b) Case 7, (c) Case 8, (d) Case 9, and (e) Case 10.

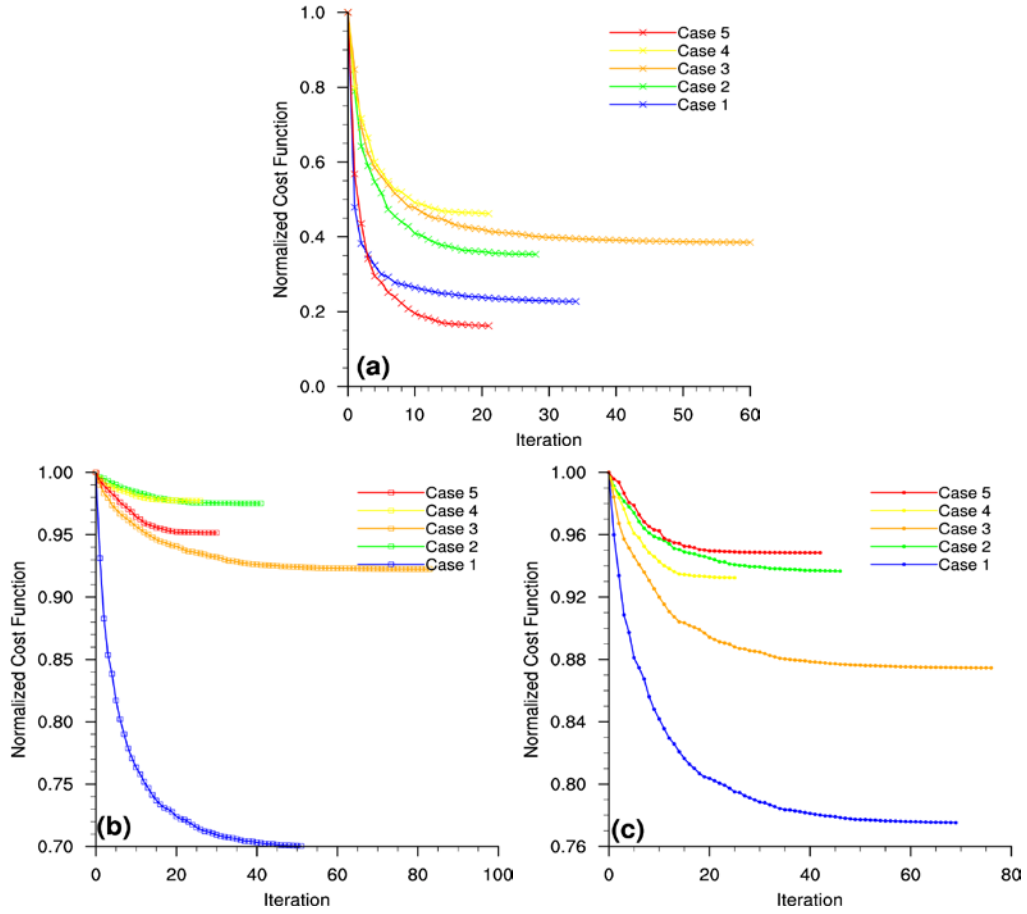


Figure 4.18. Normalized cost function as a function of iteration number for Case 1 (blue), Case 2 (green), Case 3 (orange), Case 4 (yellow), and Case 5 (red). (a) 4DVAR, (b) OUTER, and (c) QSVA experiments.

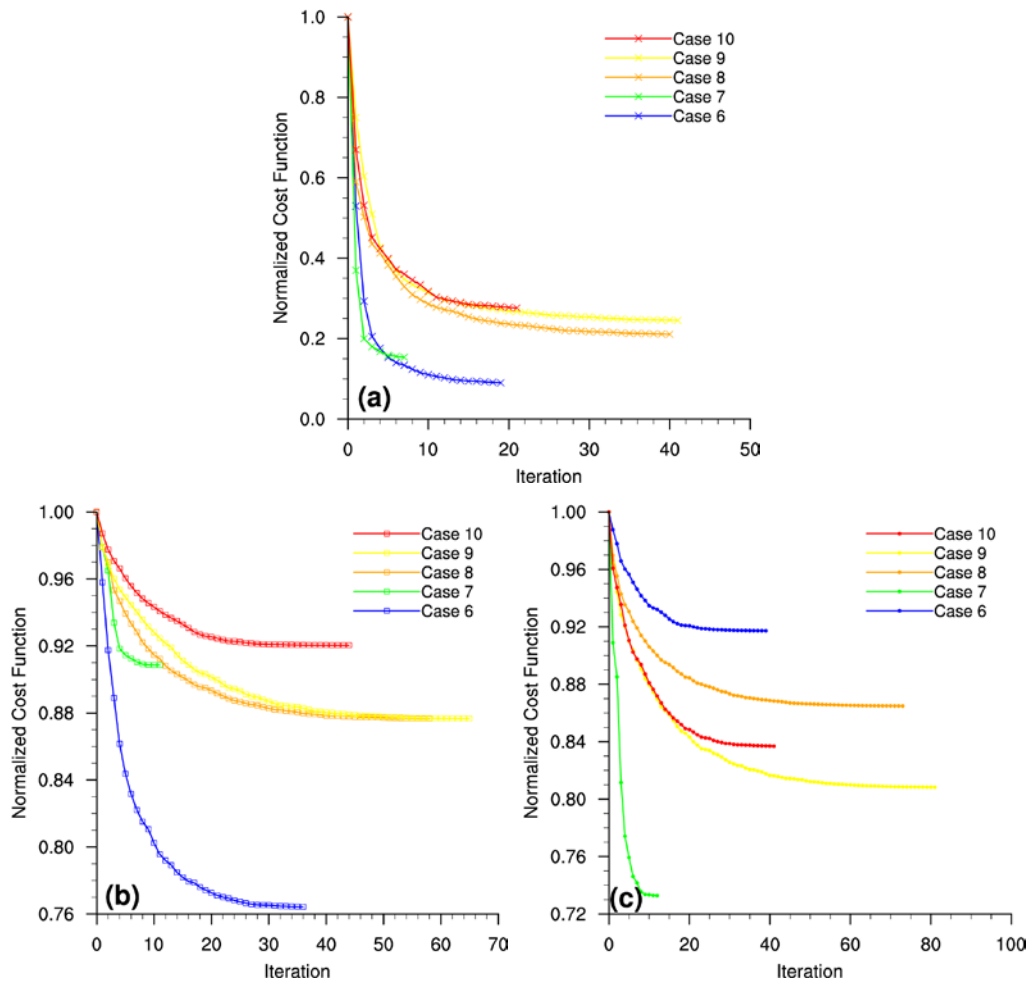


Figure 4.19. Same as Figure 4.18 but for Case 6 (blue), Case 7 (green), Case 8 (orange), Case 9 (yellow), and Case 10 (red).

Figure 4.20 shows RMSEs of O-B/O-A for radial velocity and the number of assimilated observations in 4DVAR, OUTER, and QSVA experiments for heavy rainfall cases in 2006 (i.e., Cases 1-5). O-B/O-A statistics are calculated for the second and third outer loop in OUTER experiment, and they are calculated for the assimilation window of 0, 10, 20, and 30-minute in QSVA experiment. The number of assimilated observations in OUTER or QSVA experiment is greater than that in 4DVAR experiment for all the cases, and the increase in the number of assimilated observations is the greatest for Case 1. RMSEs of O-A are reduced compared to RMSEs of O-B in 4DVAR, OUTER, and QSVA experiments for all the cases, and this implies successful assimilation of radar data. RMSEs of O-B are reduced consistently in OUTER experiment as more outer-loops are applied. Likewise, RMSEs of O-B are reduced progressively in QSVA experiment as the length of the assimilation window is increased. RMSE of O-A in OUTER (the third outer-loop) or QSVA experiment (30-min assimilation window) is smaller than that in 4DVAR experiment for Cases 1, 4, and 5. Although RMSE of O-A in OUTER or QSVA experiment is greater than 4DVAR experiment for Cases 2 and 3, the difference is not significant when considering the increase in the number of assimilated observations.

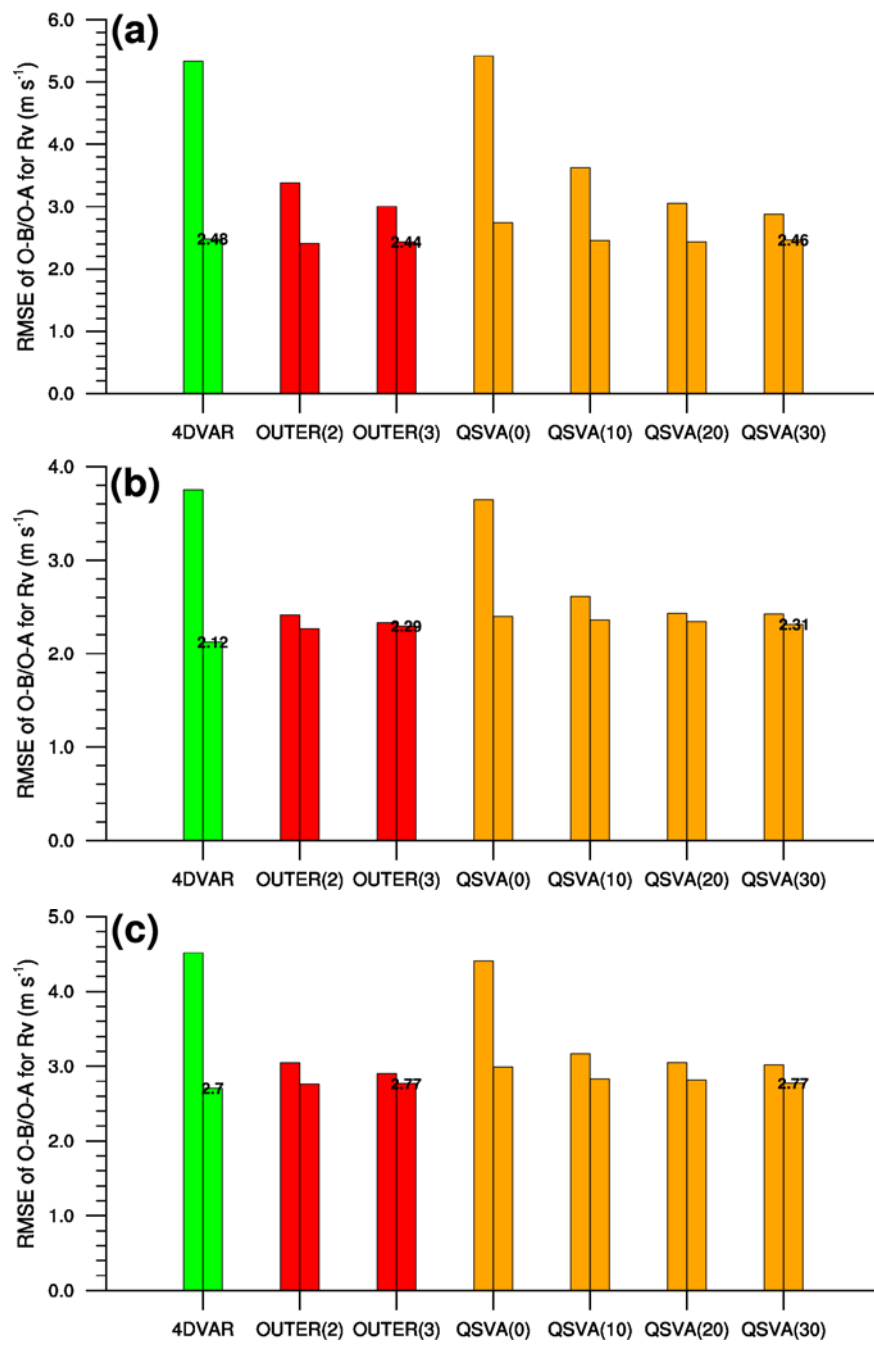
RMSEs of O-B/O-A and the number of assimilated observations for Cases 6-

10 are shown in Fig. 4.21. As for Cases 1-5, the number of assimilated observations in OUTER or QSVA experiment is greater than that in 4DVAR experiment although the difference among experiments is case-dependent. RMSEs of O-B in OUTER experiment are decreased progressively as more outer-loops are applied. Similarly, RMSEs of O-B in QSVA experiment are reduced consistently as the assimilation window is lengthened. For Cases 6, 9, and 10, RMSE of final O-A in OUTER or QSVA experiment is less than 4DVAR experiment. Although RMSE of final O-A in OUTER or QSVA experiment is larger than that in 4DVAR experiment for Cases 7 and 8, the difference is not large when considering the increase in the number of assimilated observations. As a result, the improvement of first guess in OUTER and QSVA experiments results in the improved analysis and use of more observations compared to 4DVAR experiment, which is consistent with results of Cases 1-5.

Figure 4.22 shows computational time on Linux cluster with 24 CPUs for Cases 1-5 (Fig. 4.22a) and Cases 6-10 (Fig. 4.22b). For reference, the number of total iterations for each experiment is also indicated. In OUTER experiment, the number of total iterations refers to sum of iterations for three inner-loop minimizations. In QSVA experiment, the number of total iterations refers to

sum of iterations for four assimilation windows (i.e., 0, 10, 20, and 30 minutes). For all the cases, the number of iterations in OUTER experiment is about 3-5 times of 4DVAR experiment due to the use of three outer loops, and hence computing time in OUTER experiment is much greater than 4DVAR experiment (approximately 3-5 times, proportional to the number of iterations). Although the number of iterations in QSVA experiment is slightly greater than that in OUTER experiment, computing time in QSVA experiment is less than OUTER experiment and it is less than twice of 4DVAR experiment.

Based on the analyses of cost-function values and O-B/O-A statistics, it can be said that the quality of first guess and analysis in OUTER or QSVA experiment is better than that in 4DVAR experiment via the consistent update of first-guess field. Computing time in OUTER experiment is increased significantly compared to 4DVAR experiment due to multiple outer loops. However, the increase in computing time in QSVA experiment is not large compared to OUTER experiment despite the nearly the same quality of analysis. It should be also noted that computing time in QSVA experiment can be reduced further by using loose inner-loop stopping criterion for prior minimizations of the QSVA method.



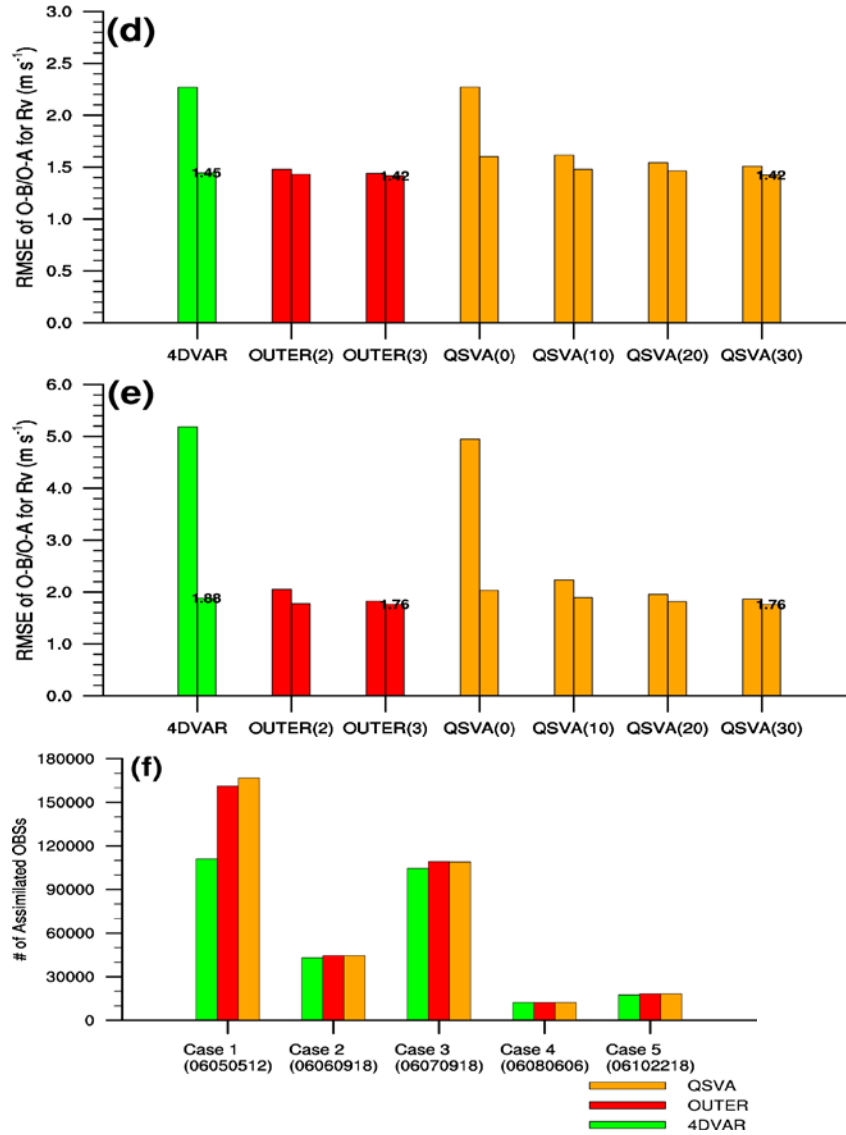
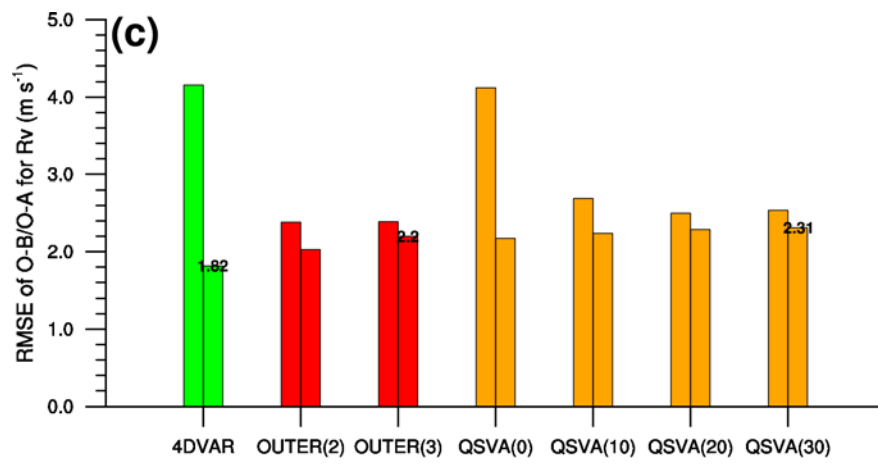
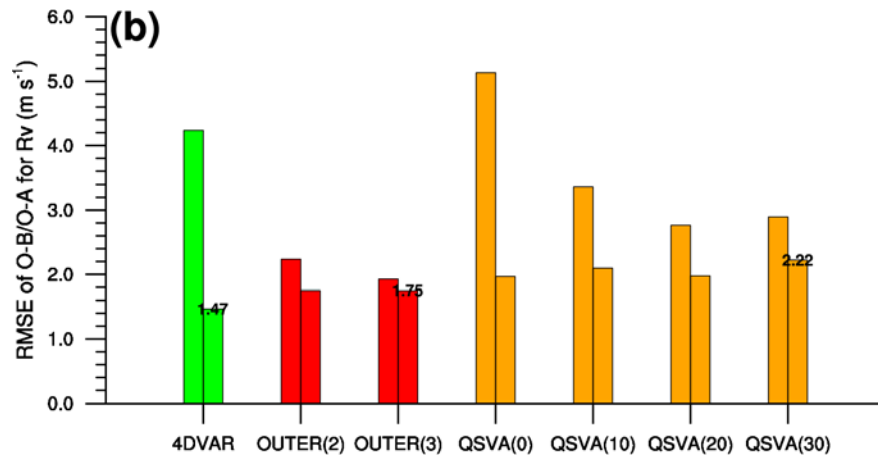
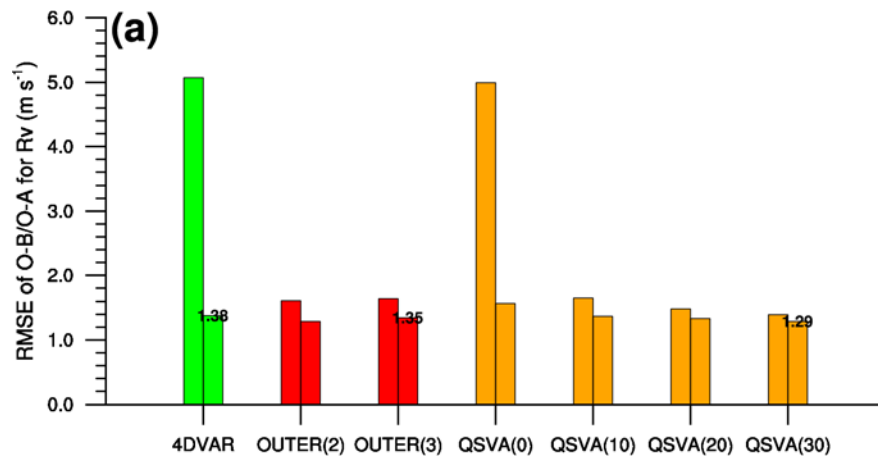


Figure 4.20. RMSEs of O-B and O-A for radial velocity (m s^{-1}) computed from 4DVAR (green), OUTER (red), and QSVa (orange) experiments. Results for (a) Case 1, (b) Case 2, (c) Case 3, (d) Case 4, and (e) Case 5 are shown. In case of OUTER experiment, results for the second and third outer loops are shown, and in case of QSVa experiment, results for assimilation window of 0, 10, 20, and 30 minutes are shown. (f) The number of total assimilated observations in 4DVAR (green), OUTER (red), and QSVa (orange) experiments.



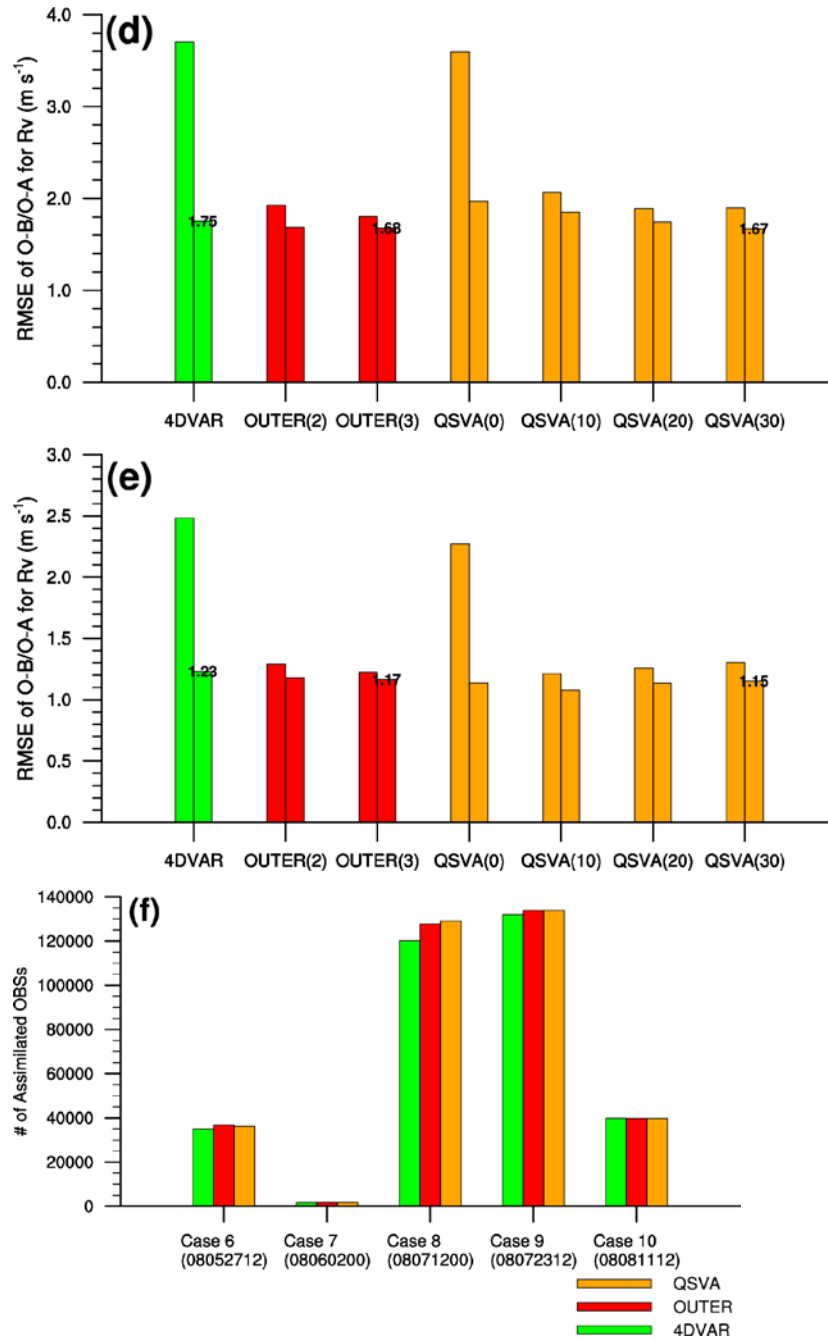


Figure 4.21. Same as Figure 4.20 but for Cases 6, 7, 8, 9, and 10.

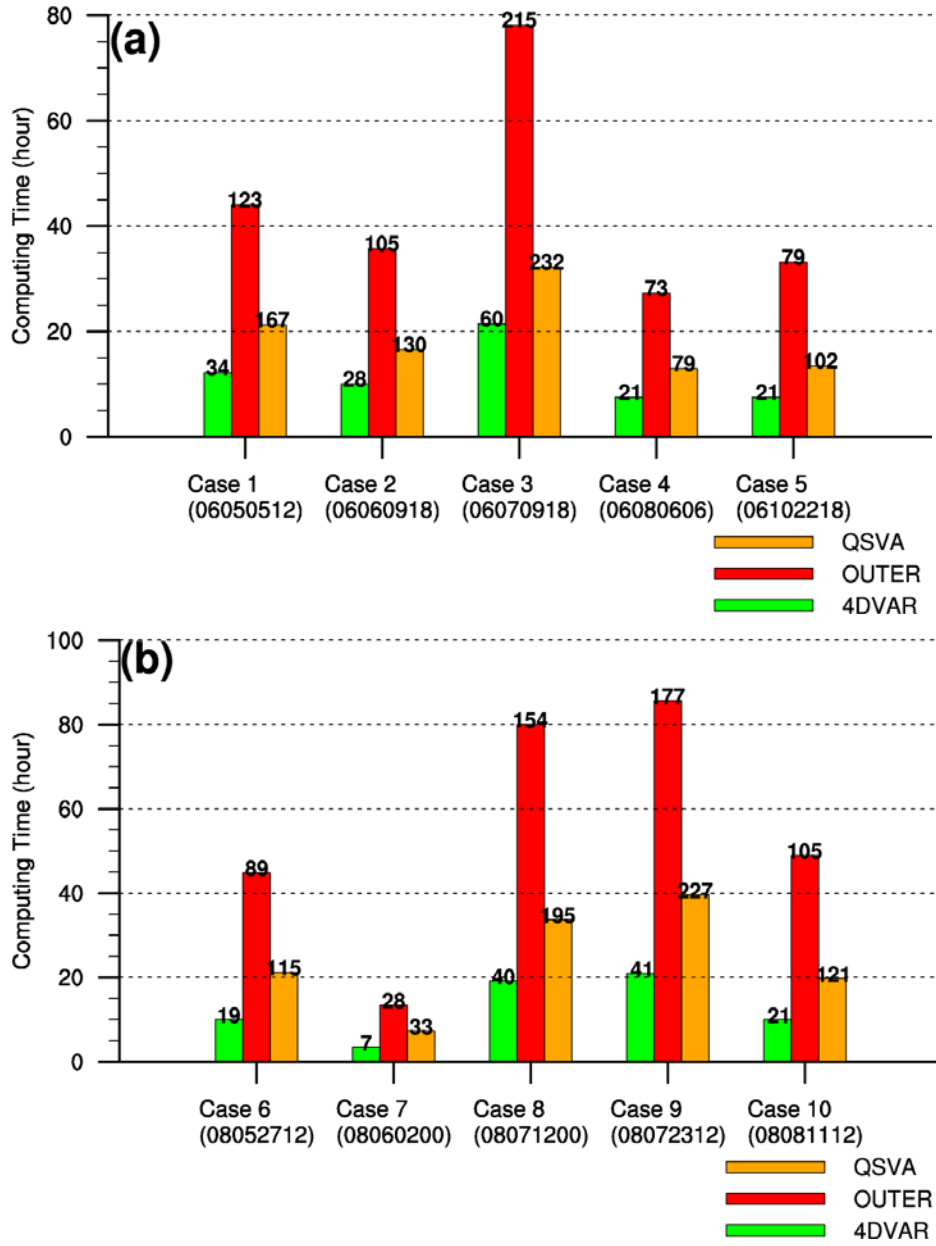


Figure 4.22. Computing time (hour) on Linux cluster with 24 CPUs for 4DVAR (green), OUTER (red), and QSVA (orange) experiments. (a) Cases 1-5 and (b) cases 6-10. The number of total iterations for each experiment is indicated.

24-h forecast (6-h forecast in case of Case 4) is made using the analysis of each experiment. Figure 4.23 shows threat scores and bias scores of 24-h (6-h for Case 4) accumulated rainfall for threshold value of 20 mm. In 3 (Cases 2, 3, and 4) out of 5 heavy rainfall cases in 2006, rainfall forecasts of data assimilation experiments (i.e., 4DVAR, OUTER, and QSVA experiments) are improved compared to CONTROL experiment in terms of both threat and bias scores. For Case 2, threat score and bias score in OUTER experiment are better than those in QSVA experiment. However, for Cases 3 and 4, threat and bias scores in QSVA experiment are better than those in OUTER experiment. For Case 5, rainfall forecasts in 4DVAR and OUTER experiments are degraded compared to CONTROL experiment in terms of both threat and bias scores, but rainfall forecast in QSVA experiment is improved compared to CONTROL experiment, especially in terms of bias score. For Case 1, threat score is one and bias score is also one for threshold value of 20 mm because rainfall is distributed widely over the Korean Peninsula. Overall rainfall forecasts in data assimilation experiments are similar to CONTROL experiment for Case 1.

Threat scores and bias scores of 24-h accumulated rainfall for threshold value of 20 mm computed from 5 heavy rainfall cases in 2008 are shown in Fig. 4.24. For Case 6, rainfall forecasts in data assimilation experiments are degraded

compared to CONTROL experiment in terms of two scores (except for bias score of OUTER experiment). For Case 7, although overestimation of rainfall amount in CONTROL experiment is reduced in data assimilation experiments, threat scores in data assimilation experiments are worse than CONTROL experiment. It should be noted that the degradation in rainfall forecasts of Cases 6 and 7 in data assimilation experiments is due to unavailability of USAF radar data and relatively small amount of radar data. For these cases, the use of outer loops or the QSVA method is pointless, and hence threat score and bias score for OUTER or QSVA experiment are not better than those for 4DVAR experiment. Rainfall forecasts for Cases 9 and 10 are improved via the assimilation of radar radial velocity data. For Case 9, threat and bias scores in OUTER experiment are better than those in QSVA experiment. In contrast, for Case 10, rainfall forecast in QSVA experiment is better than OUTER experiment in terms of threat and bias scores. For Case 8, in 4DVAR and OUTER experiments, rainfall forecasts are degraded compared to CONTROL experiment, however, through the assimilation of radar data using the QSVA method, rainfall forecast is improved compared to CONTROL experiment. Consequently, in 7 out of 10 heavy rainfall cases, rainfall forecasts are improved in at least one of data assimilation experiments. Among these 7 cases,

rainfall forecast in QSVa experiment is better than OUTER experiment for 5 cases. The reason for this forecast result will be investigated further at the end of this section.

Figure 4.25 shows temporally-averaged RMSE of radial velocity for heavy rainfall cases in 2006 (Cases 1-5) and 2008 (Cases 6-10). Error is calculated by using radar radial velocity observations over South Korea and derived model radial velocity at an interval of 30 minutes. Overall, RMSE of radial velocity is in the range of about 3.0 to 5.0 m s^{-1} . RMSEs of radial velocity in data assimilation experiments are reduced compared to CONTROL experiment for all the cases except for Case 1. In 6 out of 9 cases, where forecasts are improved compared to CONTROL experiment in terms of RMSE of radial velocity, RMSE of radial velocity in QSVa experiment is smaller than those in 4DVAR and OUTER experiments. In data assimilation experiments, wind forecasts as well as rainfall forecasts are improved compared to CONTROL experiment. Especially, it should be noted that forecasts of QSVa experiment are better than those of OUTER experiment based on the analyses of threat/bias scores and RMSE of radial velocity.

Analyses of both OUTER and QSVa experiments are better (i.e., closer to the observations) than that of 4DVAR experiment. However, forecasts of rainfall

and/or meteorological fields are better in OUTER experiment for some cases, and they are better in QSVA experiment for the other cases. In order to investigate the factor which has an influence on forecast skill, percentage error in linearization at the end of 30-minute assimilation window is calculated (Table 4.5). Percentage error in linearization is calculated by using nonlinear and linear growth of perturbation (from analysis increment) in terms of dry total energy as mentioned previously. In interpreting percentage error in linearization, positive value denotes that nonlinear growth is greater than linear growth, and vice versa. On the whole, percentage errors in OUTER and QSVA experiments are reduced compared to 4DVAR experiment. This is because in OUTER and QSVA experiments, first guess is updated progressively through the use of outer loop or gradually-increasing assimilation window, and nonlinear model trajectory is also updated accordingly. Percentage error in QSVA experiment is reduced further compared to OUTER experiment due to quasi-static adjustment of minimizing solution. In other words, in QSVA experiment, length of assimilation window is gradually increased, nonlinearity of original minimization problem is also gradually increased, and hence probability of getting trapped near local minima remains relatively low during assimilation window. Consequently, in the cases where percentage error in linearization is

relatively high (Cases 3, 4, 5, 8, and 10), forecast of QSVA experiment is better than OUTER experiment due to quasi-static adjustment of minimizing solution, and in the other cases (Cases 2 and 9), forecast of OUTER experiment is better than QSVA experiment.

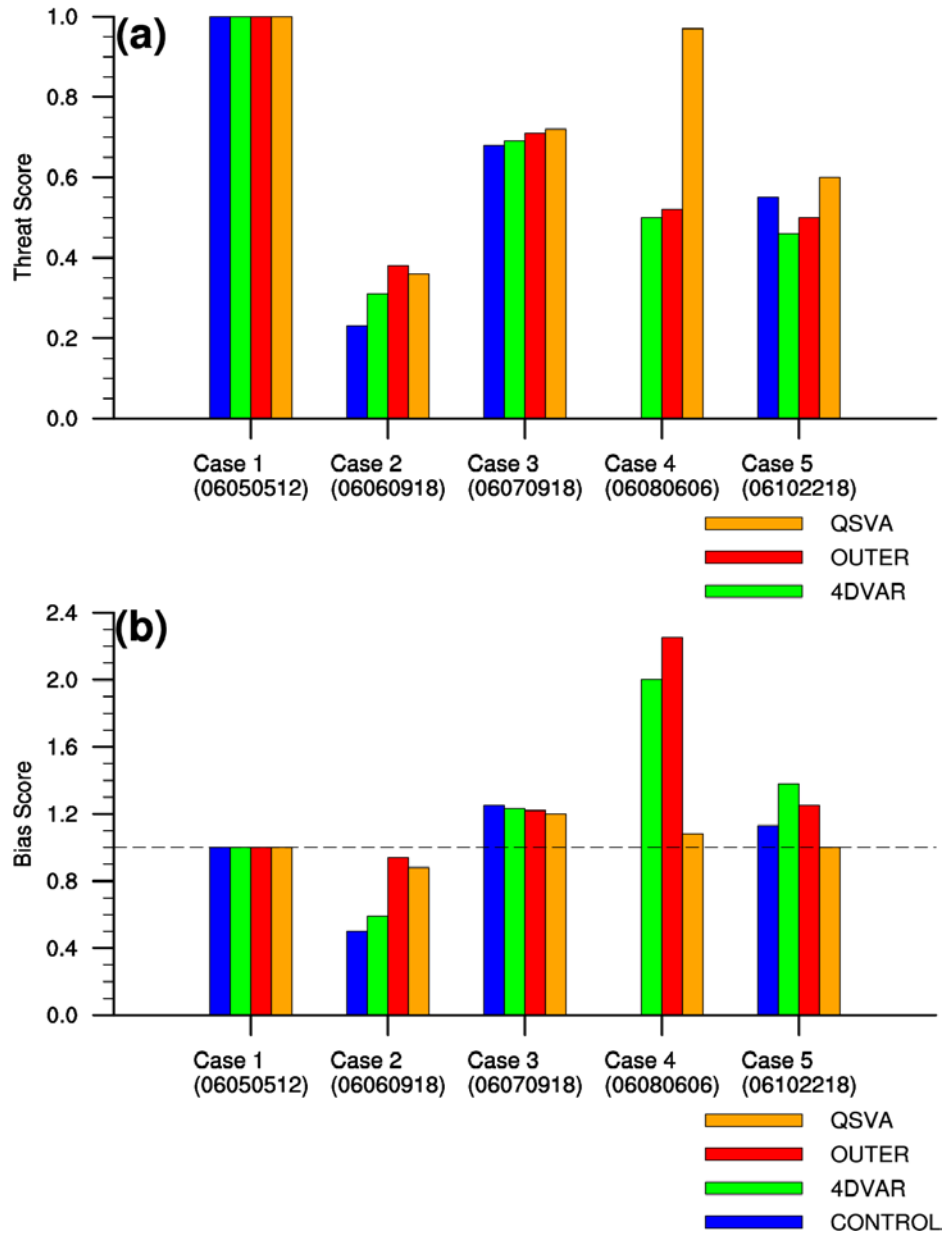


Figure 4.23. (a) Threat score and (b) bias score of 24-h (or 6-h) accumulated rainfall for threshold value of 20 mm in CONTROL (blue), 4DVAR (green), OUTER (red), and QSVA (orange) experiments. Results for Cases 1, 2, 3, 4, and 5 are shown.

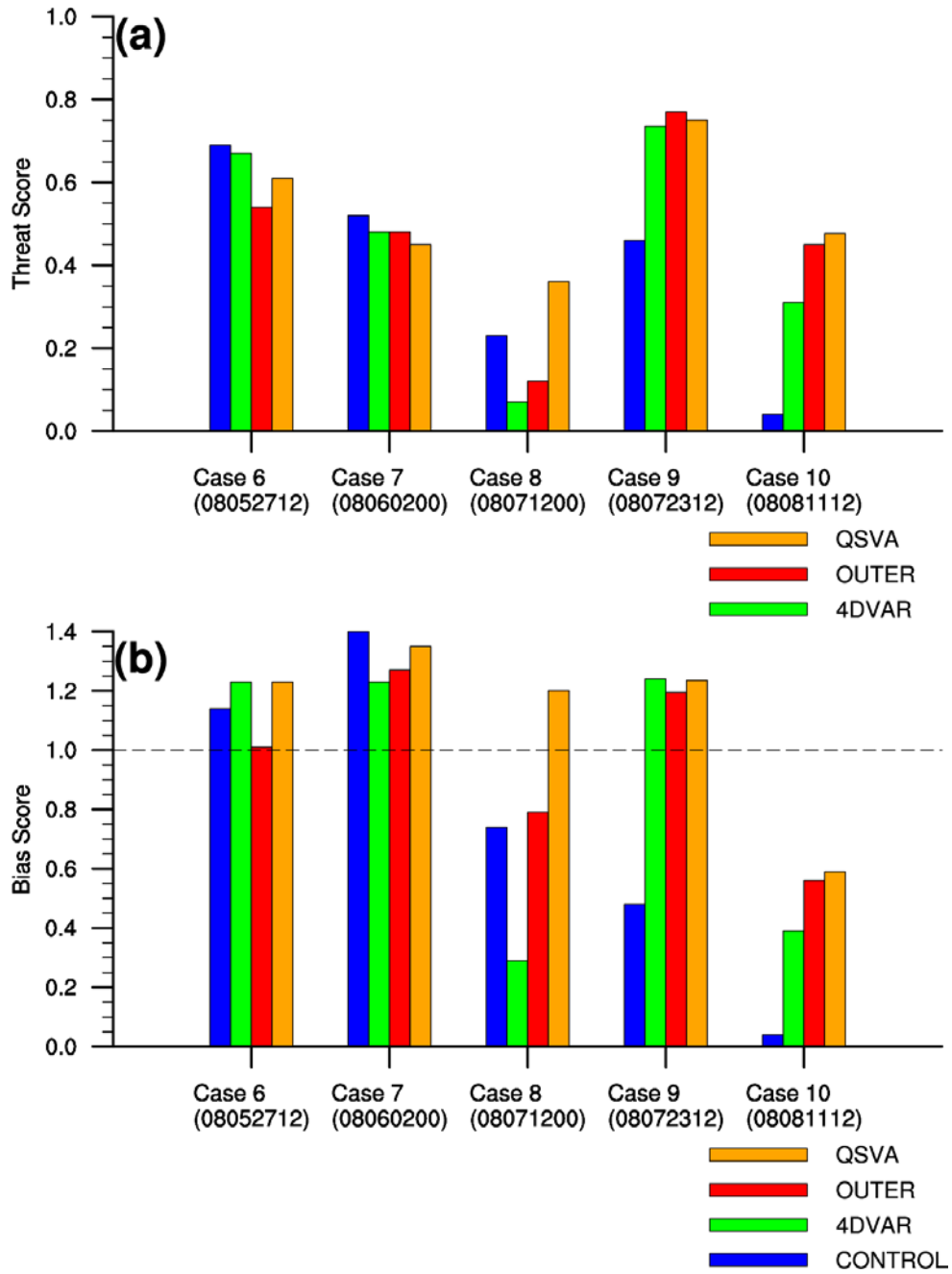


Figure 4.24. Same as Figure 4.23 but for Cases 6, 7, 8, 9, and 10.

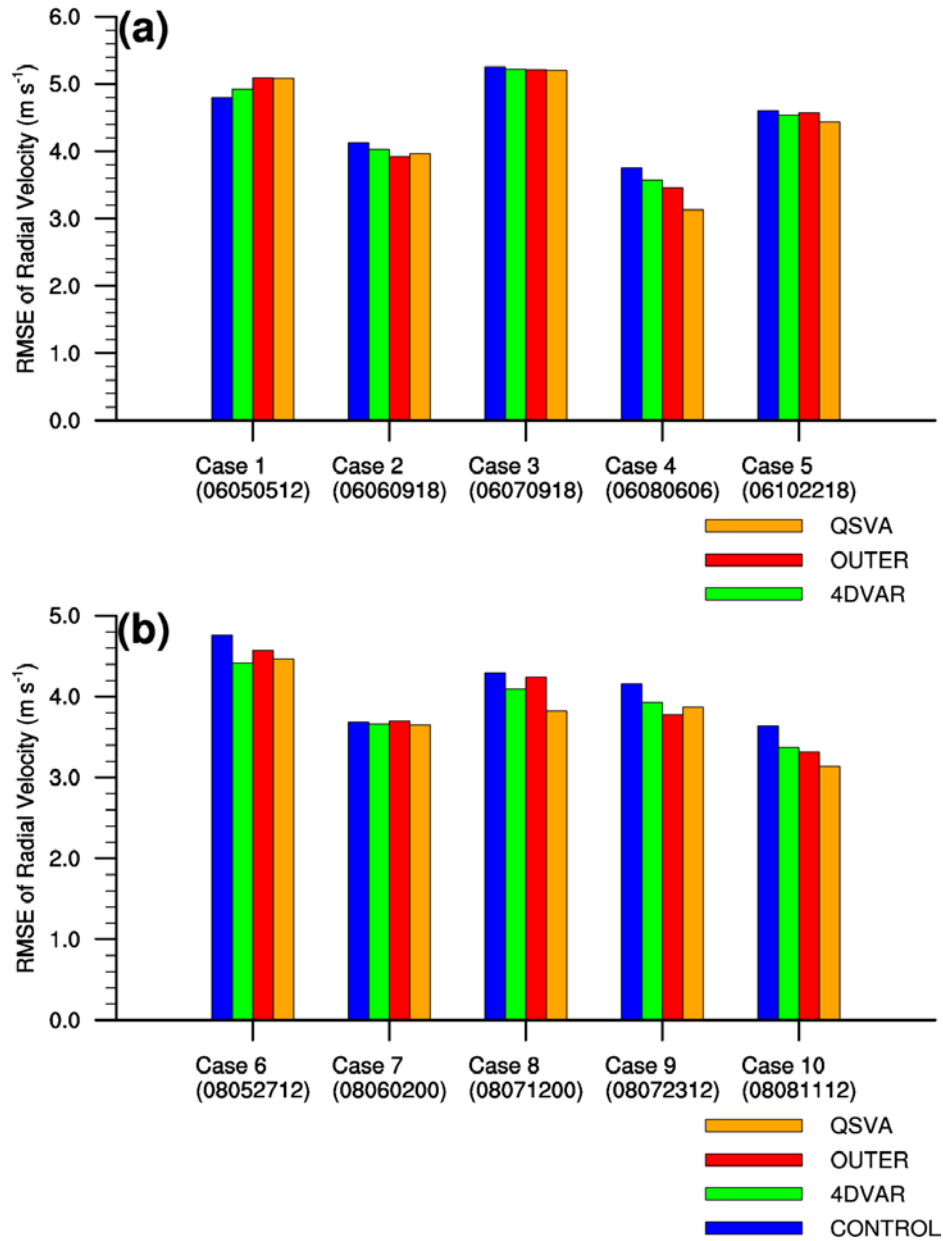


Figure 4.25. RMSE of radial velocity (m s^{-1}) for CONTROL (blue), 4DVAR (green), OUTER (red), and QSVA (orange) experiments. (a) Cases 1-5 and (b) cases 6-10. RMSEs of radial velocity during 24-h (or 6-h) forecast are averaged.

Table 4.5. Percentage error in linearization (%) at the end of an assimilation window for 4DVAR, OUTER, and QSVA experiments.

Case	4DVAR	OUTER	QSVA
Case 1	-9.44	-5.27	-3.56
Case 2	4.97	3.11	2.86
Case 3	-21.19	-15.46	-5.36
Case 4	-22.06	-9.62	-5.53
Case 5	-18.47	-12.28	-4.09
Case 6	-6.90	-4.10	-2.49
Case 7	1.03	0.95	0.85
Case 8	-18.66	-13.79	-5.07
Case 9	9.64	6.05	4.14
Case 10	24.87	19.36	5.24

Chapter 5. The ASDA method and its comparison to variational methods

5.1. Case description

Figure 5.1 shows 18-h accumulated rainfall distribution from 1800 UTC 26 to 1200 UTC 27 July 2006. Rainfall was concentrated over the central part (including Gyeonggi and Gangwon provinces) of the Korean Peninsula and it was band-shaped. There were two localized rainfall maxima: one at Seoul and the other at Hongcheon. 18-h accumulated rainfall amount at Seoul and Hongcheon was 187.5 mm and 189.0 mm, respectively. 1-h accumulated rainfall amount in time series of rainfall at Seoul and Hongcheon peaked at 0700 UTC and 0900 UTC 27 July 2006 with maximum rainfall amount of 32.0 mm and 37.0 mm, respectively (Fig. 5.9). Horizontal distribution of 18-h accumulated rainfall and time series of rainfall at two localized maxima will be investigated again in section 5.3, being compared with experiment results.

Synoptic environments related to heavy rainfall at 0000 UTC 27 July 2006 are

shown in Fig. 5.2. At 850 hPa, North Pacific high-pressure system extended to the Korean Peninsula, and this made the atmosphere over the Korean Peninsula very unstable. Warm and moist air was transported to the Korean Peninsula by southerly or southwesterly flow between cyclonic circulation and anti-cyclonic circulation (Fig. 5.2a). Maximum wind speed of southerly or southwesterly flow was greater than 20 m s^{-1} and hence it could be considered as Low Level Jet (LLJ). It is known that low-level convergence appears at the nose of LLJ, where wind speed decreases abruptly (Astling et al., 1985; McCorcle, 1988; Chen and Kpaeyeh, 1993; Jiang et al., 2007). Over the Yellow Sea, low-level convergence related to LLJ appeared, and it could provide forcing for upward motion (Fig. 5.2b). At 500 hPa, mid-level trough was located west of the Korean Peninsula. Cyclonic vorticity was found over the Yellow Sea although its amplitude was small compared to that related to low-pressure system (e.g., Aleutian Low; Fig. 5.3c). The role of this Mesoscale Convective Vortex (MCV) will be investigated further at the end of this section. At 200 hPa, the Korean Peninsula was located on the right of the entrance of Upper Level Jet (ULJ) and divergence related to this ULJ was locally maximized over the Yellow Sea (Fig. 5.3d). Both upper-level divergence related to ULJ and low-level convergence related to LLJ were favorable for upward motion, which was essential for the

development of Mesoscale Convective Systems (MCSs).

Radar reflectivity and wind vector over the Korean Peninsula at 4-km height are shown in Fig. 5.3. In order to show morphological transition in the MCS development, radar reflectivity and wind vector from 1800 UTC 26 to 1200 UTC 27 July 2006 at an interval of 1-hour are plotted. From 1800 UTC 26 to 0600 UTC 27 July 2006, the MCS, which affected the Korean Peninsula, could be classified as Training Line/Adjoining Stratiform (TL/AS)-type defined in Schumacher and Johnson (2005). Prolonged heavy convective rainfall was observed along the training (or convective) line and stratiform rainfall was adjacent to the region of convective rainfall. The MCS moved east/northeastward due to west/southwesterly flow over the Korean Peninsula. After 0600 UTC 27, the MCS affecting the Korean Peninsula had characteristics of Back Building (BB)-type MCS also defined in Schumacher and Johnson (2005). Convective cells formed over the west coast of the Korean Peninsula continuously, and they moved eastward slowly, or sometimes were quasi-stationary and merged into bigger cells. This characteristic of BB-type MCS, namely linear development and slow movement caused heavy rainfall over a localized area and a short period of time.

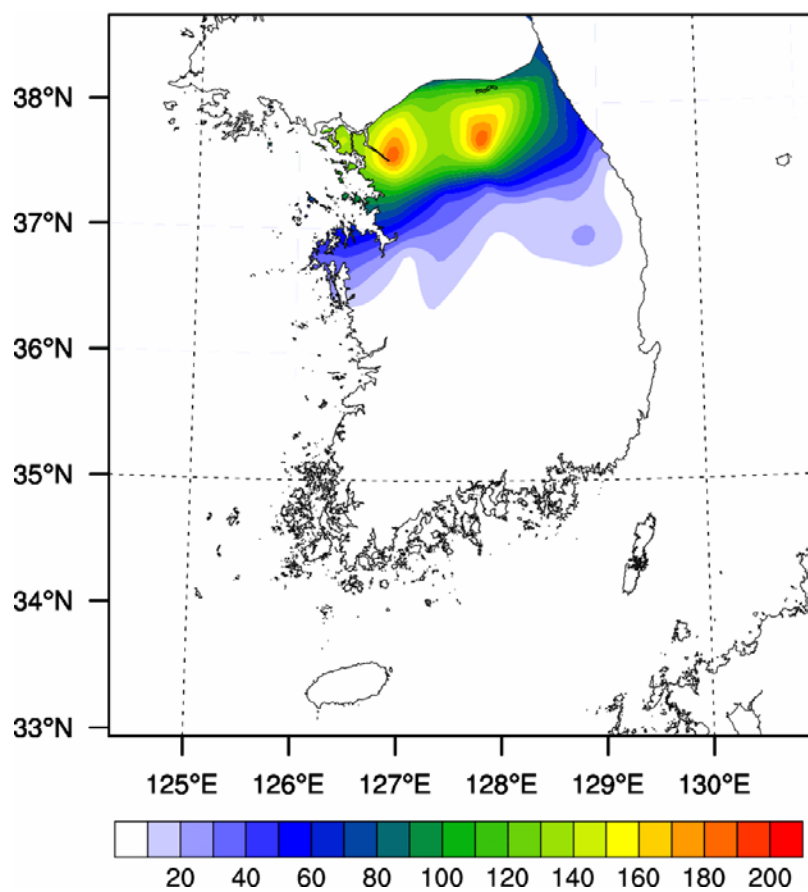


Figure 5.1. Observed 18-h accumulated rainfall ($\text{mm } 18\text{h}^{-1}$) distribution from 1800 UTC 26 to 1200 UTC 27 July 2006.

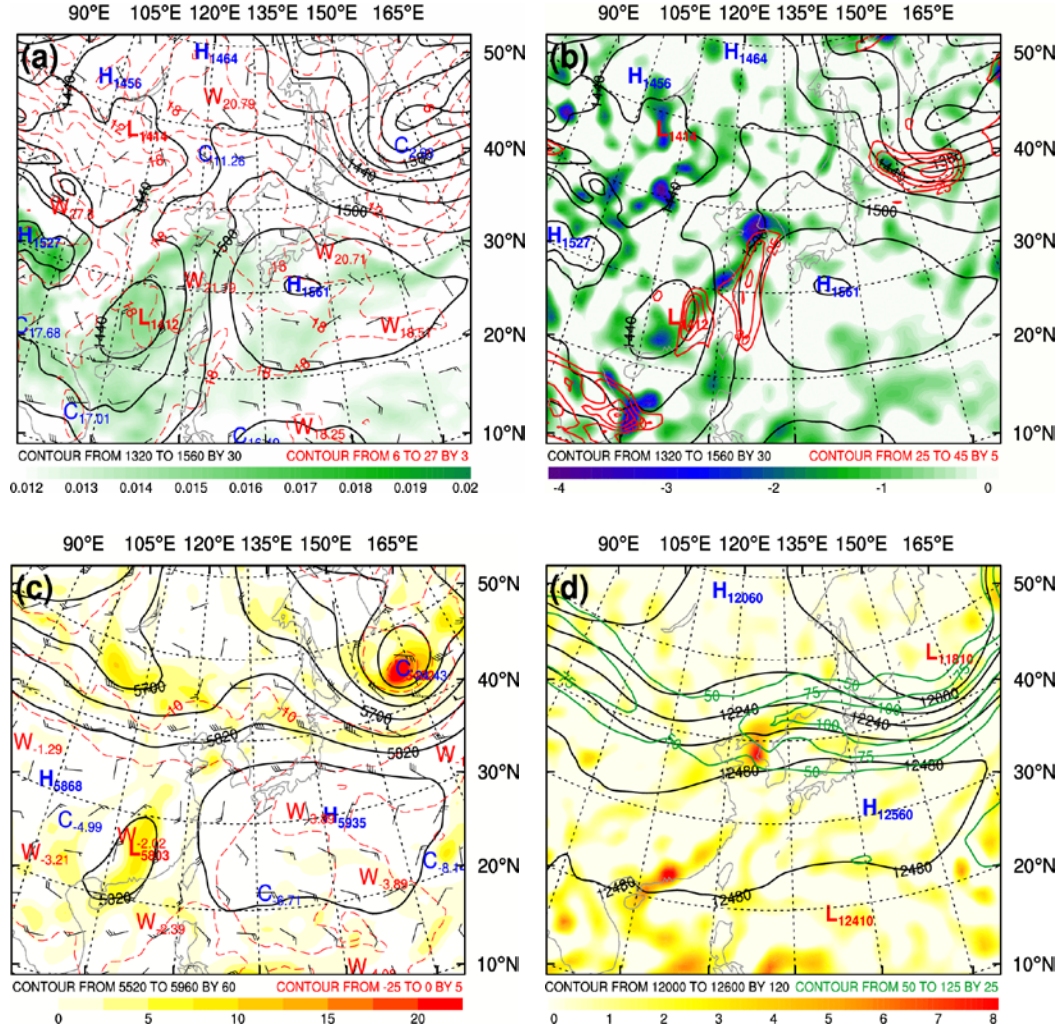
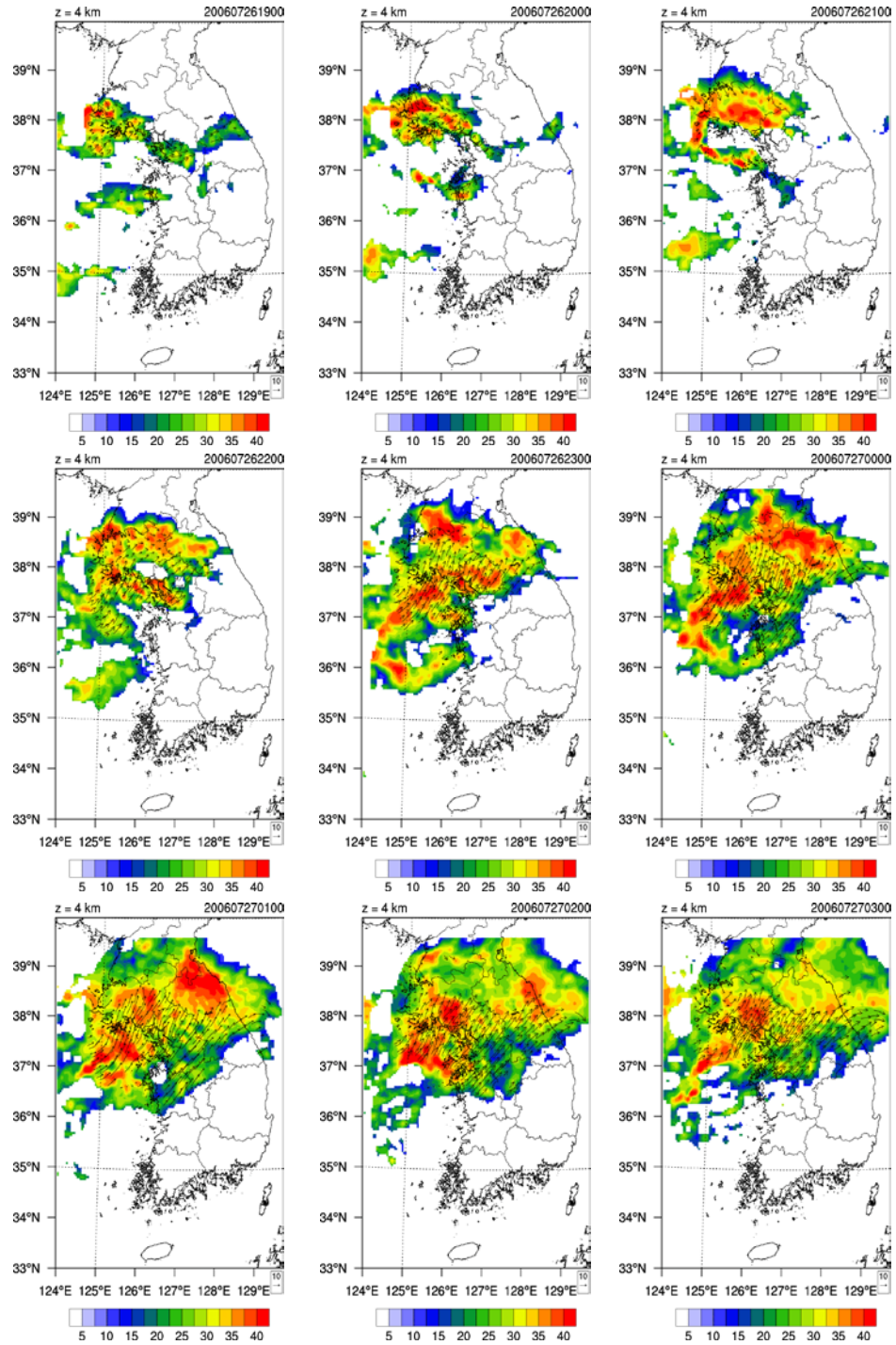


Figure 5.2. Synoptic environments at 0000 UTC 27 July 2006. (a) geopotential height (black solid, contour interval of 30 m), temperature (red dashed, contour interval of 3°C), water vapor mixing ratio (shaded, greater than 0.012 kg kg⁻¹), and wind vector (knot) at 850 hPa, (b) geopotential height (black solid, contour interval of 30 m), wind speed (red solid, contour interval of 5 knots), and divergence (shaded, 10⁻⁵ s⁻¹, only negative values are plotted) at 850 hPa, (c) geopotential height (black solid, contour interval of 60 m), temperature (red dashed, contour interval of 5°C), relative vorticity (shaded, 10⁻⁵ s⁻¹, only positive values are plotted), and wind vector (knot) at 500 hPa, (d) geopotential height (black solid, contour interval of 120 m), wind speed (green solid, contour interval of 25 knots), and divergence (shaded, 10⁻⁵ s⁻¹, only positive values are plotted) at 200 hPa.



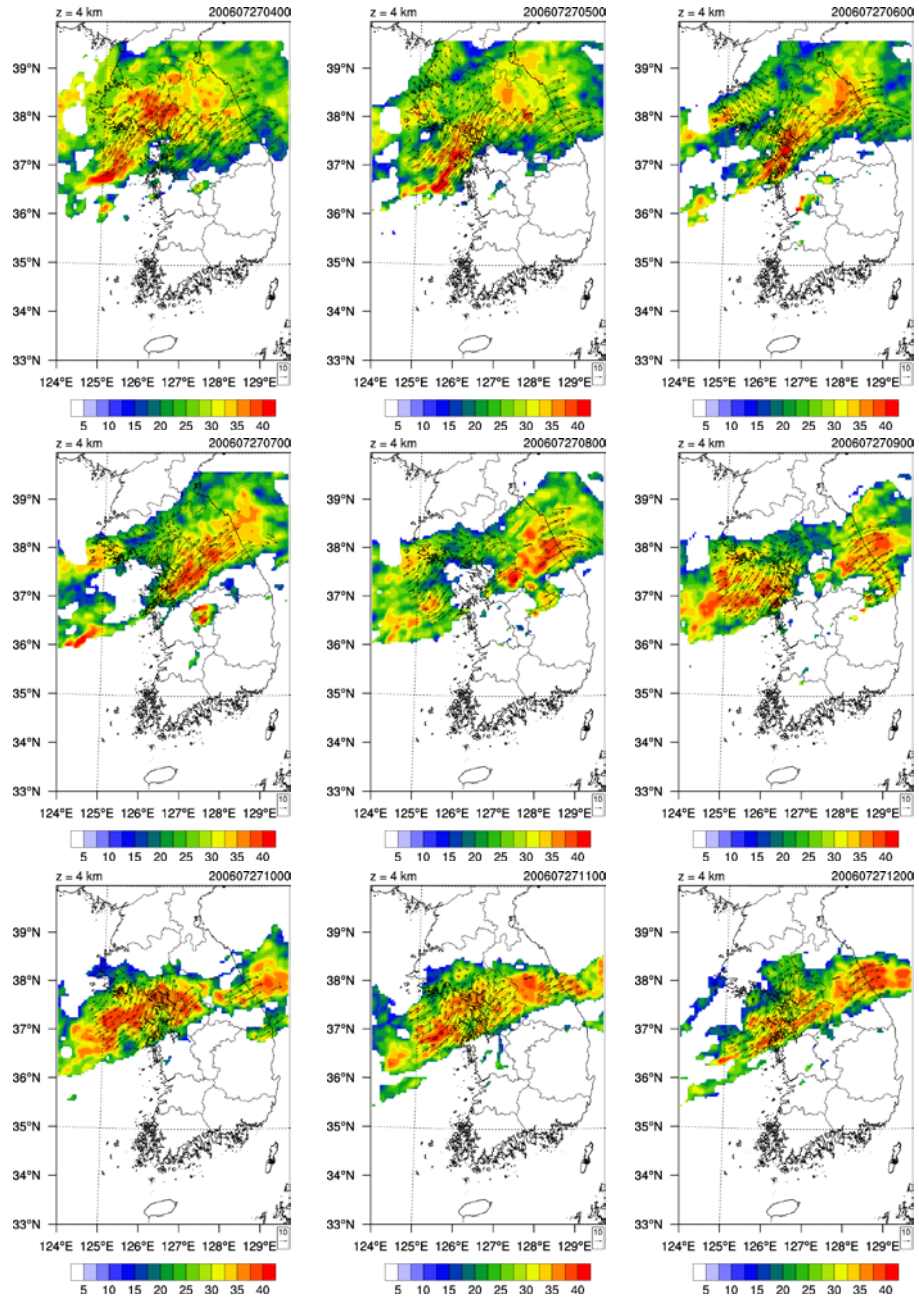


Figure 5.3. Observed radar reflectivities (dBZ) at 4-km height from 1900 UTC 26 to 1200 UTC 27 July 2006 with an interval of one hour.

Figure 5.4 shows vertical wind shear vector between surface and 925 hPa, and that between 925 hPa and 500 hPa superimposed on 850-hPa equivalent potential temperature at 1800 UTC 26 July 2006. There existed large gradient in equivalent potential temperature over the Korean Peninsula, and TL/AS-type MCS developed on the cool side of this synoptic-scale boundary. The large gradient in equivalent potential temperature implied baroclinic instability over the Korean Peninsula. Continuous transport of warm and moist air to the Korean Peninsula by LLJ increased convective instability, and subsequently, it might induce upward motion. These conditions were responsible for convective rainfall related to TL/AS-type MCS.

The mid-level (925-500-hPa) wind shear vector had a large component parallel to the convective line (Fig. 5.4b). In contrast, the low-level (surface-925-hPa) wind shear vector had a large component perpendicular to the convective line (Fig. 5.4a). Above 925 hPa, thermal wind balance could be assumed and hence the shear was largely boundary-parallel. However, below 925 hPa, thermal wind balance was not valid, and the shear was nearly perpendicular to the boundary. According to Rotunno et al. (1988), this condition favors updrafts leaning over the cool side of the boundary, and this leaning updrafts contribute to stratiform rainfall farther to the cool side of the

boundary. These features of vertical wind shear are consistent with properties of TL/AS-type MCS mentioned in Schumacher and Johnson (2005).

Figure 5.5 shows hodograph and skew T-log p diagram for Osan at 0600 UTC 27 July 2006. Upper-level wind was relatively weak compared to mid- and lower-level wind. As a result, wind shear vector reversed its direction sharply with height, and this reversal in the wind shear was reflected by a ‘hairpin’ shape hodograph (Fig. 5.5a). According to Schumacher and Johnson (2008 and 2009), MCV interacts with vertical wind shear in the development of BB-type MCS. In this heavy rainfall case, MCV was generated by prior convective rainfall related to TL/AS-type MCS and this MCV interacted with the vertical wind shear. This interaction destabilized the atmosphere by lifting conditionally-unstable air (i.e., warm and moist air) to its saturation level as noted in Schumacher and Johnson (2008 and 2009). Due to the vortex-related destabilization, Convective Available Potential Energy (CAPE) increased from 0 J kg^{-1} to 862 J kg^{-1} and Convective Inhibition (CIN) decreased from 84 J kg^{-1} to 4 J kg^{-1} compared to 0000 UTC 27 (Fig. 5.5b).

Cold pool and meso high are usually observed beneath mid-latitude squall lines and heavy rainstorms (Maddox et al., 1979; Johnson, 2001). Cold-pool-related MCSs are linearly developed and propagate rapidly. Relative humidity

over the central part of the Korean Peninsula at 0600 UTC 27 July 2006 was greater than 90%, and hence evaporation of falling rainfall might not occur. As a result, no cold pool and corresponding meso high was observed, and instead meso low was located over the central part of the Korean Peninsula (Fig. 5.6).

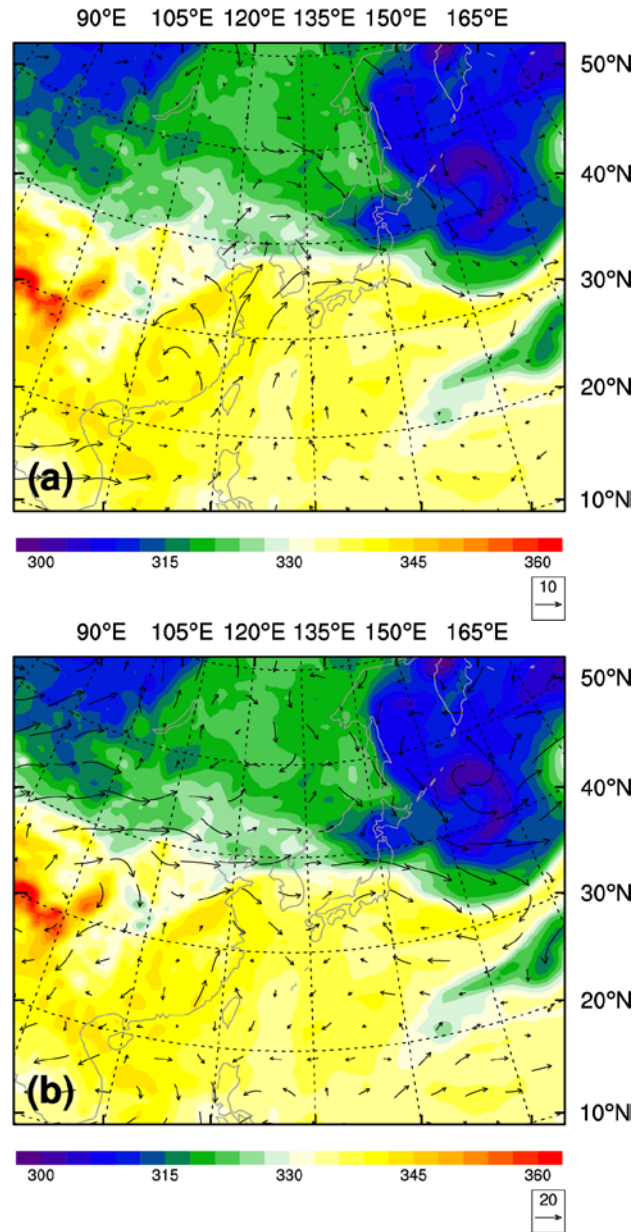


Figure 5.4. Horizontal distribution of 850-hPa equivalent potential temperature (shaded, K) and vertical wind shear vector (knot hPa⁻¹) between (a) surface and 925 hPa and (b) 925 hPa and 500 hPa at 1800 UTC 26 July 2006.

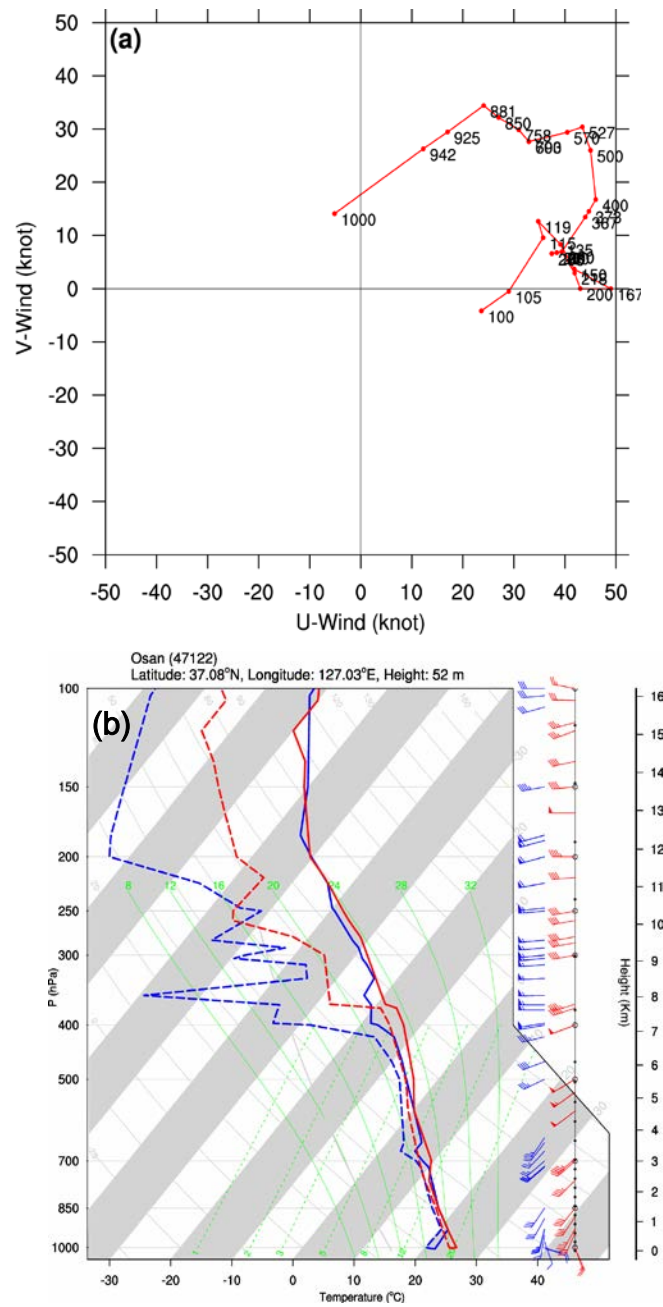


Figure 5.5. (a) Hodograph and (b) skew T-log p diagram of Osan at 0600 UTC 27 July 2006.

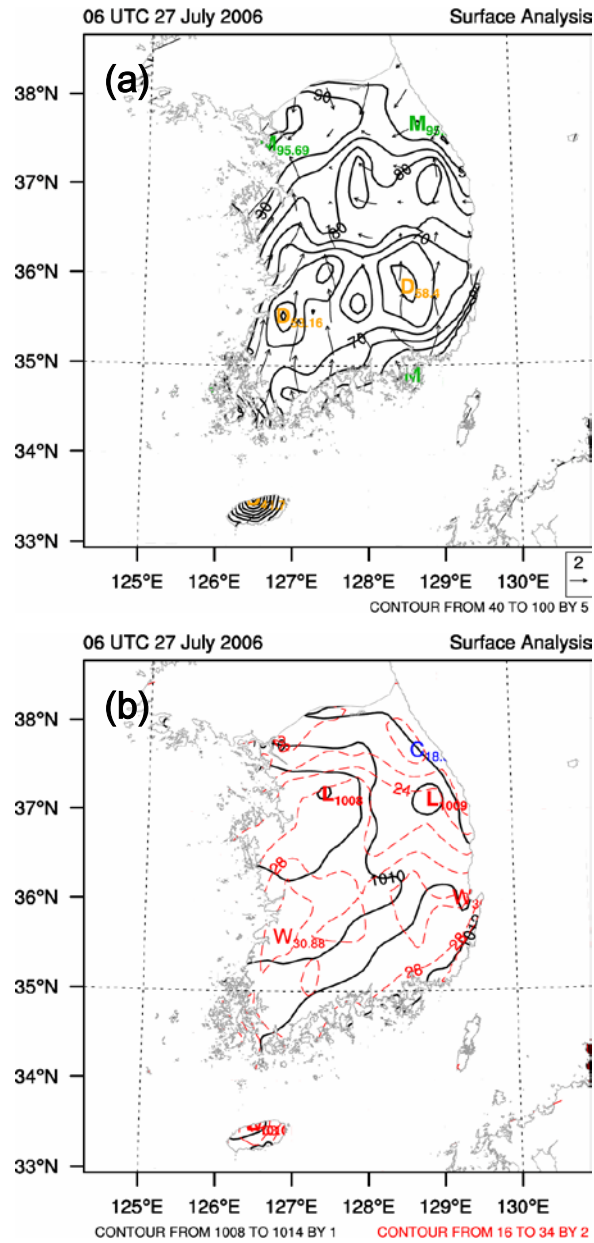


Figure 5.6. Surface analyses of (a) relative humidity (black solid, contour interval of 5%) and wind vector (m s^{-1}), and (b) pressure (black solid, contour interval of 1 hPa) and temperature (red dashed, contour interval of 2°C) at 0600 UTC 27 July 2006.

5.2. Experimental design

The Weather Research and Forecasting (WRF) model (Skamarock et al., 2008) version 3.4 is used as a nonlinear forecasting model in this study. Figure 5.7 shows geographical areas of triply-nested domains with horizontal resolutions of 54 km, 18 km, and 6 km, respectively. The 54-km domain covers East Asia including Korea, Japan, Taiwan, and Eastern China. The 18-km domain covers the Korean Peninsula and the surrounding areas, and the 6-km domain focuses on South Korea. The number of horizontal grids for 54-, 18-, and 6-km domain is 120×102 , 121×103 , and 121×127 , respectively. The number of vertical levels for all the domains is 35, and model top is set at 50 hPa.

The physical parameterization schemes used for the nonlinear model run include the WRF Single-Moment 6-class (WSM6) with graupel microphysics scheme (Hong and Lim, 2006), the Kain-Fritsch cumulus parameterization scheme (Kain, 2004), the Yonsei University (YSU) planetary boundary layer scheme (Hong et al., 2006), the Rapid Radiative Transfer Model (RRTM) longwave radiation scheme (Mlawer et al., 1997), and the Dudhia shortwave radiation scheme (Dudhia, 1989). The National Centers for Environmental

Prediction (NCEP) Final analysis (FNL) data are used as initial and lateral boundary conditions for all the domains. The initial time for the forecast of the 54-, 18-, and 6-km domain is 0000 UTC, 1200 UTC, and 1800 UTC 26 July 2006, respectively. Data assimilation is conducted only in the 6-km domain and 18-h forecast from 1800 UTC 26 to 1200 UTC 27 July 2006 will be analyzed throughout this chapter.

In this study, the WRF Data Assimilation (WRFDA) system version 3.4 (Barker et al., 2004; Huang et al., 2009), including Three Dimensional Variational (3D-Var) and Four Dimensional Variational (4D-Var) methods, is used. The initial condition for the experiment without data assimilation (denoted as CONTROL experiment in Table 5.1) is used as a first guess for all the data assimilation experiments (i.e., cold start). Background error covariance is calculated by using the National Meteorological Center (NMC) method (Parrish and Derber, 1992), where the background error statistics are derived from the differences between the 24- and 12-h forecasts for one-month period of July 2006.

Radar radial velocity data from 14 radar observation sites over the Korean Peninsula (Fig. 5.7b) are used in this study. In advance of being assimilated, radar data are preprocessed by the methods given in Park and Lee (2009). The

preprocessing includes quality control, interpolation/thinning to Cartesian grids by the Sorted Position Radar INTERpolation (SPRINT; Mohr and Vaughan, 1979; Miller et al., 1986) and Custom Editing and Display of Reduced Information in Cartesian coordinate (CEDRIC; Mohr et al., 1986) packages, and hole-filling/smoothing by the CEDRIC package. Finally, radar data are converted into input format appropriate to the WRFDA. The final radar data have a horizontal resolution of 6 km, a vertical resolution of 0.5 km at heights above approximately 3.0 km, and a temporal resolution of 10 minutes.

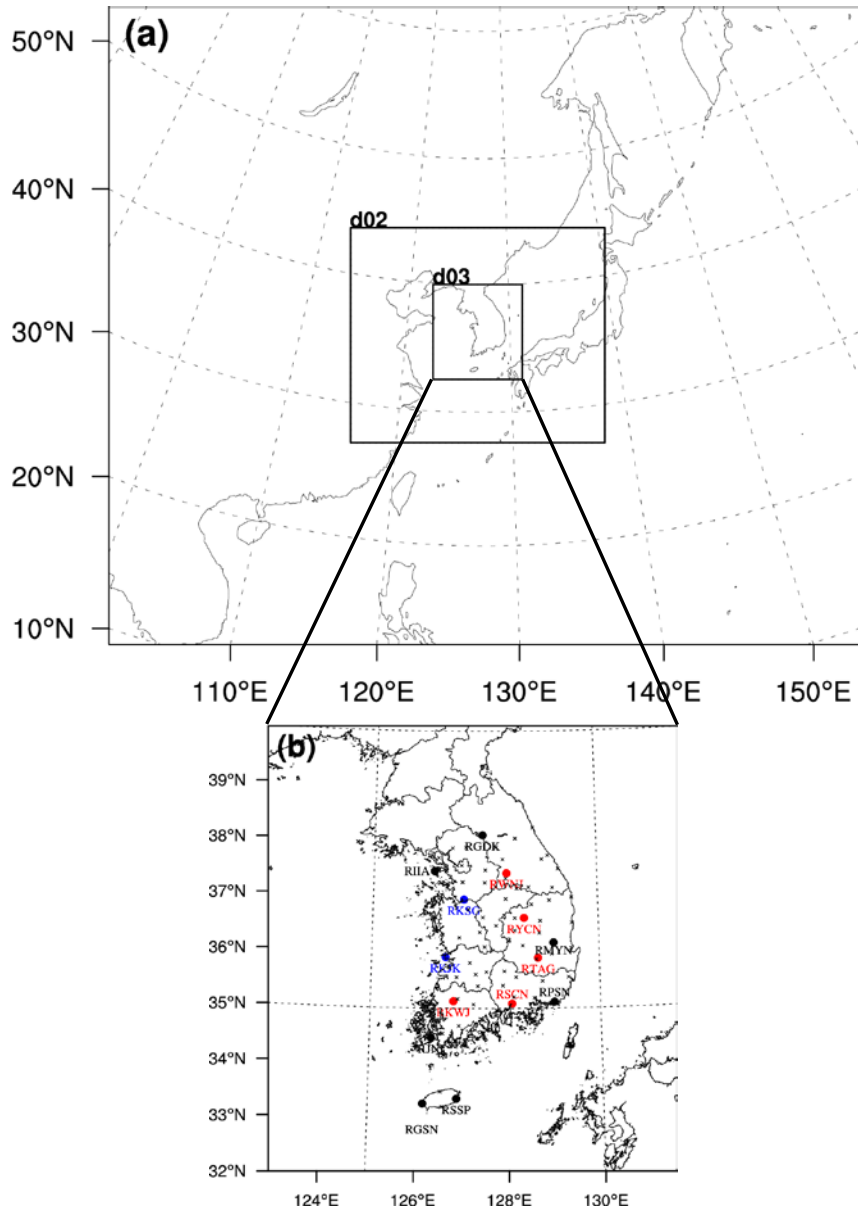


Figure 5.7. (a) Geographical areas of domains 1, 2, and 3 and (b) locations of radar observation sites operated by Korea Meteorological Administration (black), Korea Air Force (red), and United States of America Air Force (blue). Locations of Automatic Weather Station observation sites over South Korea are also indicated with crosses.

Table 5.1. Brief descriptions of numerical experiments.

Experiment name	Description
CONTROL	Experiment without data assimilation
3DVAR	Experiment with radar data assimilation using 3D-Var method
4DVAR	Experiment with radar data assimilation using 4D-Var method
ASDA	Experiment with radar data assimilation using ASDA method

5.3. Results and discussion

Experiment without data assimilation fails to simulate the heavy rainfall described in section 5.1. In order to improve the heavy rainfall forecast, radar radial velocity data are assimilated using WRF 3D-Var and 4D-Var systems. Additionally, radar data are assimilated using the proposed ASDA method. Radar data are available every 10 minutes during an assimilation window of 30 minutes from 1800 UTC to 1830 UTC 26 July 2006. Cost function is minimized using conjugate gradient algorithm with a stopping criterion of reduction in gradient norm to 0.01 of its starting value. A brief description of experiments conducted in this study is given in Table 5.1.

Figure 5.8 shows 18-h accumulated rainfall distribution from 1800 UTC 26 to 1200 UTC 27 July 2006 for CONTROL, 3DVAR, 4DVAR, and ASDA experiments. In CONTROL experiment, simulated rainfall band is shifted northeastward compared to the observations, and 18-h accumulated rainfall amount near Seoul (~ 93.8 mm) is underestimated. When radar radial velocity data are assimilated using the 3D-Var method (i.e., 3DVAR experiment), simulated rainfall band is slightly moved southwestward compared to

CONTROL experiment. However, it is still shifted northeastward compared to the observations, and 18-h accumulated rainfall amount near Seoul (~ 104.2 mm) is also underestimated. Additional experiment, 3D-Var analysis at +30 min, is conducted, and it is named as 3DVAR_30min experiment. When 18-h accumulated rainfall distribution for 3DVAR_30min experiment is analyzed, rainfall band is shifted northeastward compared to the observations, and 18-h accumulated rainfall amount at the grid point corresponding to Seoul is approximately 87.62 mm (underestimated). Overall, rainfall forecast for 3DVAR_30min experiment is very similar to 3DVAR experiment (not shown). Verification results of 3DVAR_30min experiment for the other variables such as winds and temperature are also similar to 3DVAR experiment, and hence results of 3DVAR_30min experiment will not be mentioned any longer. Simulated rainfall band in 4DVAR experiment is similar to the observations, and locations of two localized rainfall maxima are close to the observations. 18-h accumulated rainfall amount at the grid point corresponding to Seoul and Hongcheon is approximately 171.5 mm and 178.5 mm, respectively. Although 18-h accumulated rainfall amount at the point corresponding to Seoul and Hongcheon is underestimated compared to the observations (~ 187.5 mm and ~ 189.0 mm), its error is within 10% of the observed value. In ASDA experiment,

rainfall band is well simulated both in terms of shape and location when compared to the observations. Especially, locations of two localized rainfall maxima are very close to the observations. 18-h accumulated rainfall amount at the grid point corresponding to Seoul and Hongcheon is about 205.7 mm and 216.5 mm, respectively. Compared to the observations, simulated rainfall amount is slightly overestimated in ASDA experiment.

Time series of hourly rainfall amount at the point corresponding to Seoul and Hongcheon for CONTROL, 3DVAR, 4DVAR, and ASDA experiments is shown in Fig. 5.9 with the observations. In the observations at Seoul, time series of hourly rainfall was bimodal-shaped, and it peaked at 0700 UTC 27 July 2006 with rainfall amount of about 32.0 mm. In CONTROL and 3DVAR experiments, simulated time series of rainfall is unimodal-shaped, and rainfall peak appears at 0400 UTC and 0500 UTC 27 July 2006 with rainfall amount of about 25.5 mm and 49.9 mm, respectively. Correlation between time series of the observations and that of CONTROL or 3DVAR experiment is 0.295 and 0.298, respectively. In 4DVAR experiment, overall pattern of simulated time series is similar to the observations, and rainfall peak appears at 0900 UTC 27 July 2006 with rainfall amount of approximately 48.6 mm. Due to the delay in peak timing, lag-0 correlation between the observations and 4DVAR

experiment is small, but lag-2 correlation is about 0.418. Simulated time series of rainfall in ASDA experiment is similar to the observations with correlation value of 0.683. Hourly rainfall peaks at 0700 UTC 27 July 2006 like the observations although peak amount (~ 42.7 mm) is slightly overestimated compared to the observations. At Hongcheon, the observed time series of rainfall peaked at 0900 UTC 27 July 2006 with rainfall amount of approximately 37.0 mm. In CONTROL and 3DVAR experiments, localized rainfall maximum corresponding to Hongcheon is far from the observations as can be seen in Fig. 5.8. Time series of hourly rainfall in 4DVAR experiment is similar to the observations except for two-hour delay in peak timing. Hourly rainfall amount at the peak is about 40.0 mm, which is similar to the observations, and correlation between the observed time series and 4DVAR experiment is 0.748. In ASDA experiment, overall pattern of time series is well simulated although correlation coefficient is relatively small (~ 0.352) due to the overestimation of rainfall at earlier times.

Figure 5.10 shows Threat Scores (TSs) and Bias Scores (BSs) of 6-h or 18-h accumulated rainfall for threshold values of 5, 10, 25, and 50 mm. Both TS and BS are calculated using contingency table as follows.

$$TS = \frac{C}{F + O - C}, BS = \frac{F}{O}, \quad (22)$$

where O is the number of the events that occurred, F is the number of the events that are forecasted, and C is the number of the events that are correctly forecasted. TS measures how well the forecasted “yes” events correspond to the observed “yes” events and value of 1 means the perfect forecast. Overall, TSs of data assimilation experiments are greater than that of CONTROL experiment. For 6-h forecast from 0000 UTC to 0600 UTC 27 July 2006, TS of 3DVAR experiment is greater than those of 4DVAR and ASDA experiments when threshold values are 5, 10, and 25 mm. For 6-h forecast from 0600 UTC to 1200 UTC 27 July 2006, TS of 4DVAR or ASDA experiment is greater than that of 3DVAR experiment, especially when threshold value is 50 mm. When 18-h forecast is considered, TSs of 4DVAR and ASDA experiments are greater than that of 3DVAR experiment for all the threshold values. From 0000 UTC to 0600 UTC 27 July 2006, in the observations, convective rainfall related to TL/AS-type MCS was mainly located over the northern part of the Korean Peninsula, where surface rainfall observations are not available (refer to Fig.

5.7b). In 3DVAR experiment, simulated rainfall band is shifted northeastward compared to the observations; however, stratiform rainfall is simulated broadly over the central part of the Korean Peninsula. In contrast, in 4DVAR and ASDA experiments, simulated stratiform rainfall, south of main convective rainfall band, is not well simulated during that period. After 0600 UTC 27 July 2006, convective rainfall band related to BB-type MCS in the observations moved southward, and the improvement in rainfall forecast such as rainfall distribution and time series in 4DVAR and ASDA experiments is appropriately reflected in TS.

BS measures how the forecasted frequency of “yes” events compare to the observed “yes” events and value of 1 means the perfect forecast. For the first 6-h forecast (i.e., from 1800 UTC 26 to 0000 UTC 27 July 2006), rainfall is overforecasted in ASDA experiment while it is underforecasted in the other experiments. This is related to the overestimation of rainfall during the early period of forecast in ASDA experiment. For the second 6-h forecast, BS of 3DVAR experiment is closer to one than those of 4DVAR and ASDA experiments except for threshold value of 50 mm. In contrast, for the last 6-h forecast, BSs of 4DVAR and ASDA experiments are closer to one compared to that of 3DVAR experiment. These results are consistent with TS results. When

threshold value is 25 or 50 mm (i.e., heavy rainfall), rainfall is underforecasted in CONTROL and 3DVAR experiments, while it is slightly overforecasted in 4DVAR and ASDA experiments, especially for the last 6-h forecast. This implies that rainfall missed in CONTROL and 3DVAR experiments (related to BB-type MCS) is correctly forecasted in 4DVAR and ASDA experiments.

Figure 5.11 shows Root Mean Square Errors (RMSEs) of rainfall for CONTROL, 3DVAR, 4DVAR, and ASDA experiments. For the first 6-h forecast, RMSE of ASDA experiment is greater than the other experiments, and this is due to the overestimation of rainfall during this period in ASDA experiment. For the second 6-h forecast, RMSE of 3DVAR experiment is the smallest, and for the last 6-h forecast, RMSE of ASDA experiment is the smallest among all the experiments. When 18-h forecast from 1800 UTC 26 to 1200 UTC 27 July 2006 is considered, RMSEs of 4DVAR and ASDA experiments are smaller than those of CONTROL and 3DVAR experiments, and 4DVAR experiment performs the best. These RMSE results are consistent with the previous results on rainfall forecast.

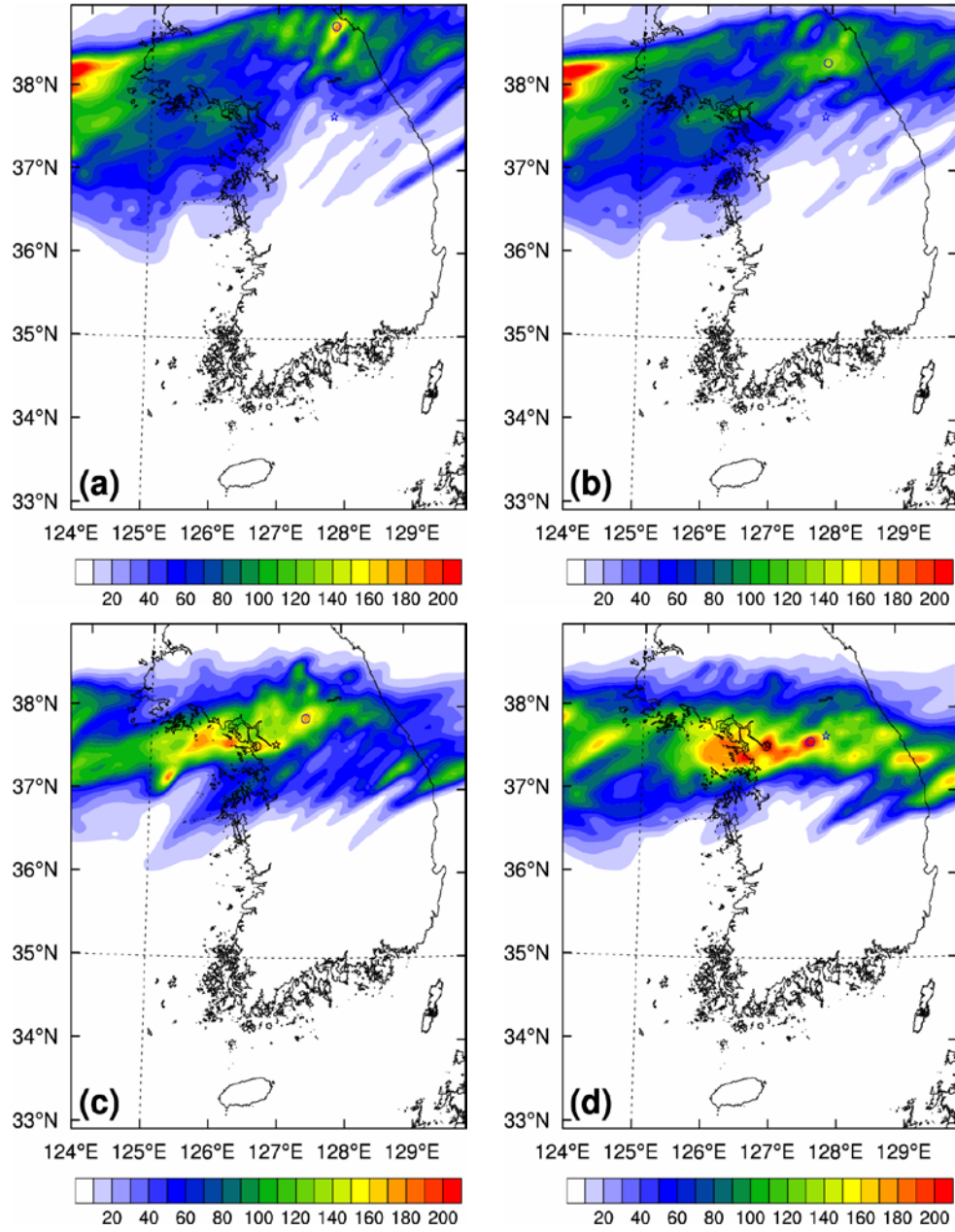


Figure 5.8. 18-h accumulated rainfall (mm 18h⁻¹) distributions from 1800 UTC 26 to 1200 UTC 27 July 2006 for (a) CONTROL, (b) 3DVAR, (c) 4DVAR, and (d) ASDA experiments.

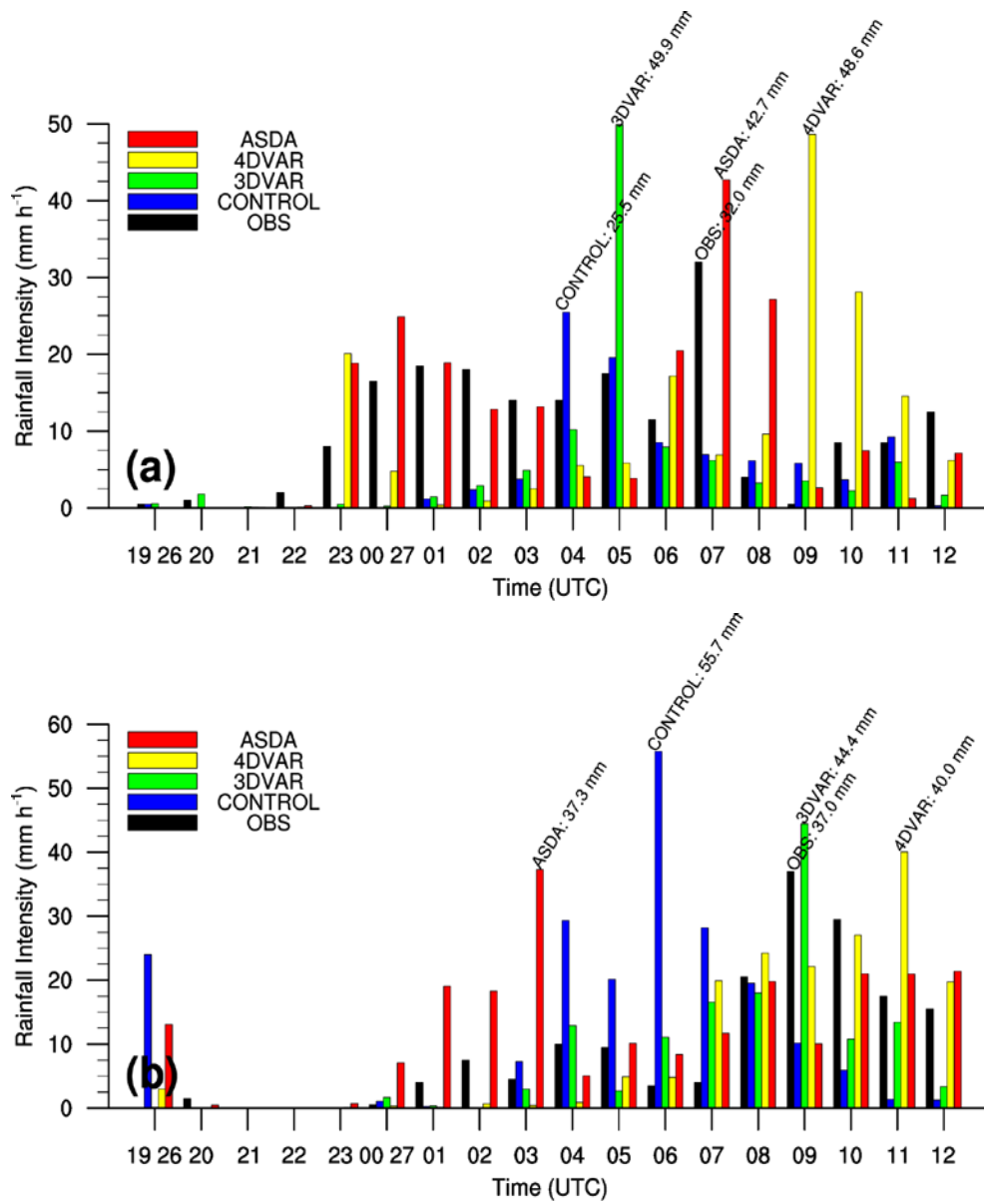


Figure 5.9. Time series of hourly rainfall amount (mm h^{-1}) at (a) Seoul and (b) Hongcheon (or the corresponding grid points in case of model experiment) for the observations (black), CONTROL (blue), 3DVAR (green), 4DVAR (yellow), and ASDA (red) experiments. Maximum hourly rainfall amount is also indicated.

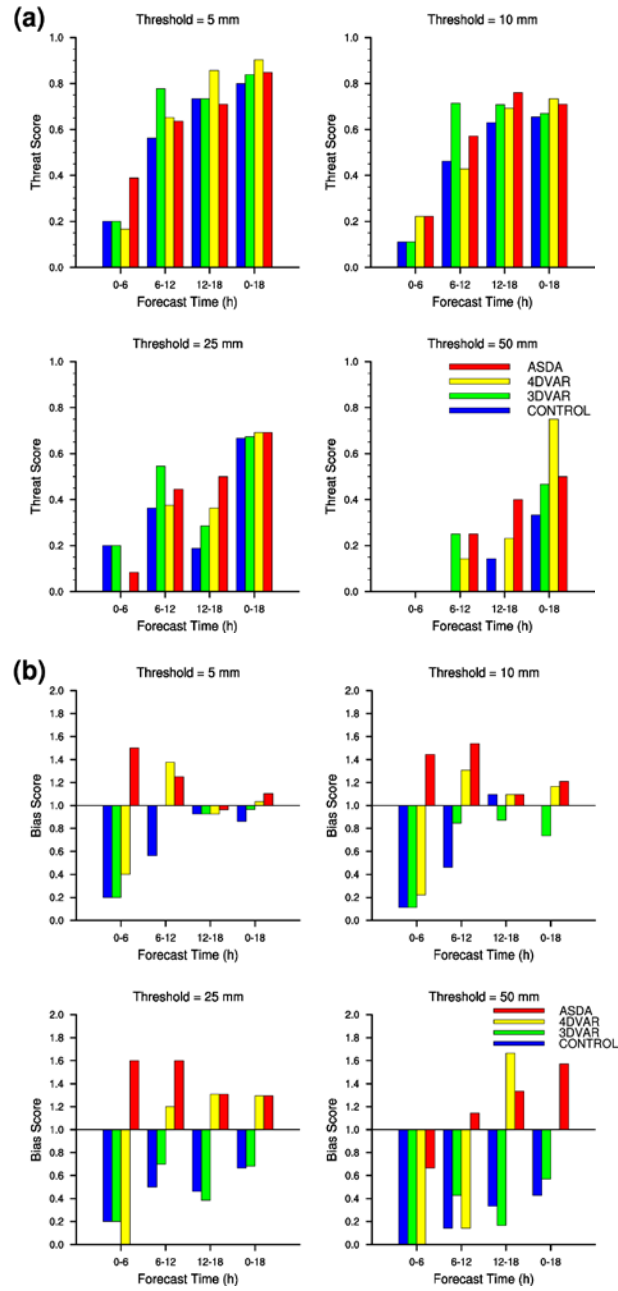


Figure 5.10. Quantitative precipitation forecast skill of CONTROL (blue), 3DVAR (green), 4DVAR (yellow), and ASDA (red) experiments for threshold values of 5, 10, 25, and 50 mm. (a) Threat score and (b) bias score.

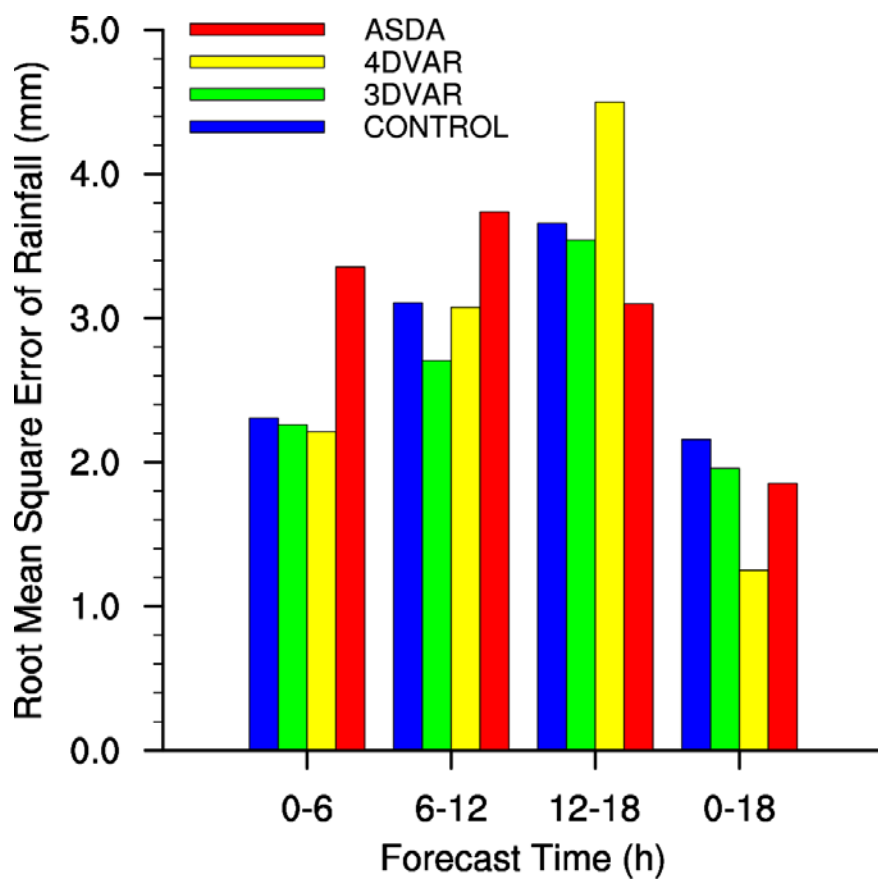


Figure 5.11. Root Mean Square Errors (RMSEs) of rainfall ($\text{mm } 6\text{h}^{-1}$ or $\text{mm } 18\text{h}^{-1}$) as a function of forecast time for CONTROL (blue), 3DVAR (green), 4DVAR (yellow), and ASDA (red) experiments.

Not only rainfall forecast but also forecasts of meteorological fields such as winds, temperature, and moisture are also improved through radar data assimilation, especially in 4DVAR and ASDA experiments. Figure 5.12 shows RMSEs verified against FNL data for CONTROL, 3DVAR, 4DVAR, and ASDA experiments as a function of forecast length. At forecast initial time, RMSEs of zonal wind, meridional wind, temperature, and water vapor mixing ratio for data assimilation experiments are greater than those for CONTROL experiment. Initial conditions of data assimilation experiments are altered by the assimilation of radar data while that of CONTROL experiment is solely based on FNL data. This causes RMSEs of data assimilation experiments at the initial time to be greater than CONTROL experiment when verified against FNL data. RMSEs of zonal wind and meridional wind for 4DVAR and ASDA experiments become smaller than those for CONTROL and 3DVAR experiments at 6-h into the forecast, and this remains unchanged during the next 12 hours. RMSEs of temperature and water vapor mixing ratio for 4DVAR and ASDA experiments are greater than those for CONTROL and 3DVAR experiments even at 6-h into the forecast. This may be due to the large analysis increments of temperature and water vapor mixing ratio for 4DVAR and ASDA experiments shown in Figs. 5.15b and c. However, RMSEs of temperature and

water vapor mixing ratio for 4DVAR and ASDA experiments are smaller than those for CONTROL and 3DVAR experiments during the last 12 hours. Consequently, forecasts of 4DVAR and ASDA experiments are better than CONTROL and 3DVAR experiments except for the initial time when evaluated using RMSE verified against FNL data.

Fits to the observations (i.e., biases) of zonal wind, meridional wind, temperature, and water vapor mixing ratio for CONTROL, 3DVAR, 4DVAR, and ASDA experiments are shown in Fig. 5.13. Fit to the observations is calculated by using sounding observations from 7 radiosonde observations sites over the Korean Peninsula at 0000 UTC 27 July 2006. Positive biases of zonal wind for 4DVAR and ASDA experiments are greater than those for CONTROL and 3DVAR experiments below 800 hPa. However, biases of zonal wind for 4DVAR and ASDA experiments are smaller than those for CONTROL and 3DVAR experiments between 800 hPa and 400 hPa, where radar data are relatively plentiful. Negative biases of meridional wind below 800 hPa are noticeable in CONTROL and 3DVAR experiments. These biases are reduced significantly in 4DVAR and ASDA experiments. Positive biases of meridional wind between 700 hPa and 400 hPa in 4DVAR and ASDA experiments are decreased slightly compared to those in CONTROL and 3DVAR experiments.

Positive (negative) biases of temperature between 800 (600) hPa and 600 (400) hPa are reduced in 4DVAR and ASDA experiments compared to those in CONTROL and 3DVAR experiments. In all the experiments, positive bias of water vapor mixing ratio prevails throughout the atmosphere (except for 450 hPa in 4DVAR experiment). These positive biases are reduced remarkably in 4DVAR and ASDA experiments compared to CONTROL and 3DVAR experiments, especially below 700 hPa. This is related to the large analysis increments of water vapor mixing ratio over the Yellow Sea (Figs. 5.15b and c) in 4DVAR and ASDA experiments. On the whole, in terms of fit to the observations, forecasts of 4DVAR and ASDA experiments are improved compared to those of CONTROL and 3DVAR experiments, particularly at mid-levels, where effects of data assimilation are the greatest. It should be also noted that biases of meridional wind and water vapor mixing ratio are reduced in 4DVAR and ASDA experiments even at lower levels due to the information-spreading effects of background error covariance and model dynamics.

Figure 5.14 shows RMSEs of radial velocity for CONTROL, 3DVAR, 4DVAR, and ASDA experiments as a function of forecast length. RMSE of radial velocity is calculated by using radar radial velocity observations from 14 radar observation sites over the Korean Peninsula (refer to Fig. 5.7b) and

forecasted radial velocity derived from forecasted wind components. At analysis time (i.e., 1800 UTC 26 July 2006), RMSEs of radial velocity for CONTROL, 3DVAR, 4DVAR, and ASDA experiments are 3.099, 2.123, 2.092, and 2.083, respectively. Compared to CONTROL experiment (RMSE of O-B), RMSEs of data assimilation experiments (RMSE of O-A) are reduced. This implies that radar data are assimilated successfully in terms of O-B/O-A statistics in data assimilation experiments and analysis of ASDA experiment is the closest to the observations at the analysis time. RMSEs of radial velocity increase rapidly during the first 6 hours and they oscillate with small amplitude of oscillation in all the experiments. Overall, RMSEs of radial velocity for data assimilation experiments are smaller than that for CONTROL experiment. RMSEs of radial velocity for 4DVAR and ASDA experiments are smaller than that for 3DVAR experiment except for during the first 2 hours into the forecast. Forecasts of radial velocity in 4DVAR and ASDA experiments are improved compared to that in 3DVAR experiment because radar data are assimilated more efficiently in those experiments. It is noted that RMSE of radial velocity for ASDA experiment is smaller than that for 4DVAR experiment during the last 6 hours. This is consistent with results of TS/BS (especially, for threshold value of 50 mm) and RMSE of rainfall.

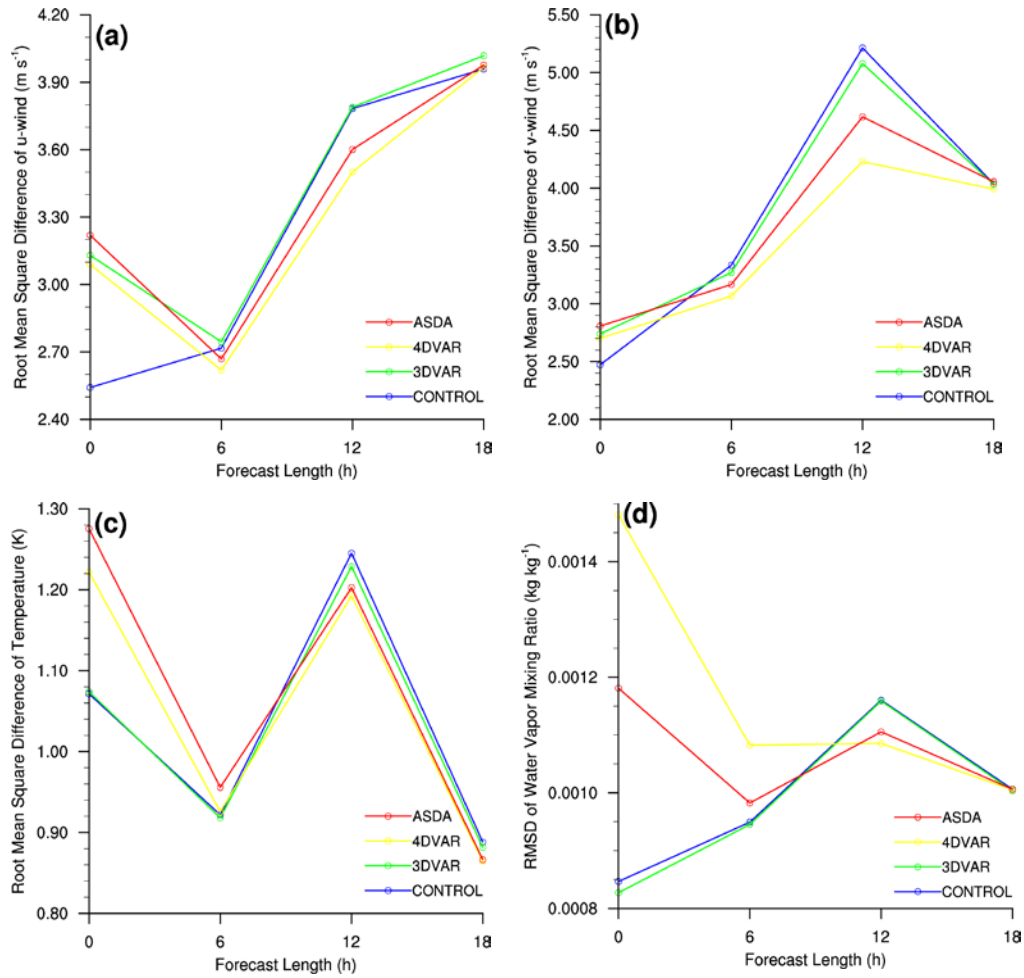


Figure 5.12. Root Mean Square Differences (RMSDs) against FNL data of (a) zonal wind (m s^{-1}), (b) meridional wind (m s^{-1}), (c) temperature (K), and (d) water vapor mixing ratio (kg kg^{-1}) as a function of forecast length for CONTROL (blue), 3DVAR (green), 4DVAR (yellow), and ASDA (red) experiments.

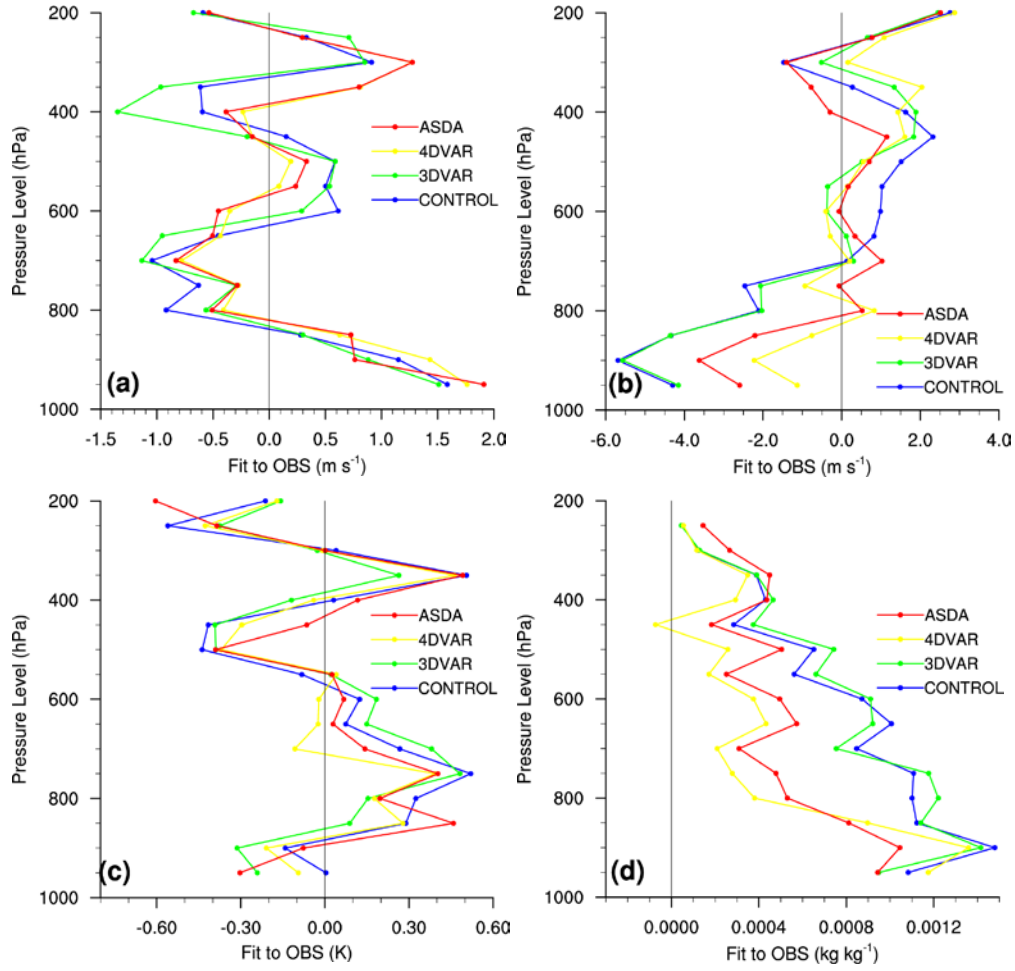


Figure 5.13. Vertical distributions of fit to the observations using sounding observations over South Korea at 0000 UTC 27 July 2006 for CONTROL (blue), 3DVAR (green), 4DVAR (yellow), and ASDA (red) experiments. (a) Zonal wind (m s^{-1}), (b) meridional wind (m s^{-1}), (c) temperature (K), and (d) water vapor mixing ratio (kg kg^{-1}).

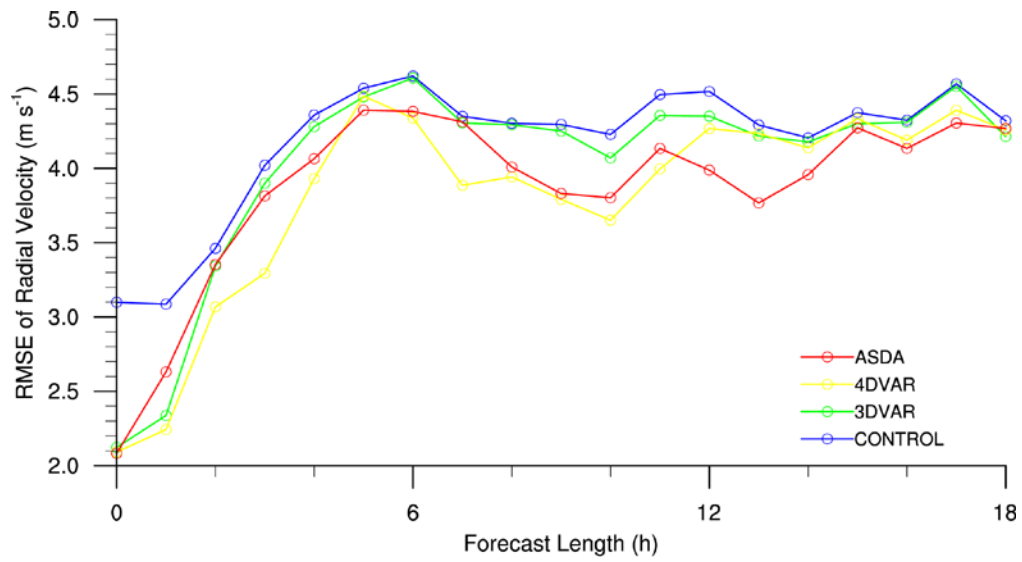


Figure 5.14. RMSEs of radial velocity (m s^{-1}) as a function of forecast length for CONTROL (blue), 3DVAR (green), 4DVAR (yellow), and ASDA (red) experiments. Radar radial velocity data from 14 radar observation sites over the Korean Peninsula are used.

In order to investigate the reason why forecasts of 4DVAR and ASDA experiments are improved compared to CONTROL and 3DVAR experiments, analysis increments (analysis minus background) of 4DVAR and ASDA experiments are analyzed. Figure 5.15 shows horizontal distribution of 850-hPa Equivalent Potential Temperature (EPT) at 1800 UTC 26 July 2006 for CONTROL, 4DVAR, and ASDA experiments. Analysis increments of EPT for 4DVAR and ASDA experiments are also shown. In CONTROL experiment, meridional gradient of EPT is not large, especially over the central part of the Korean Peninsula. However, in 4DVAR experiment, meridional gradient of EPT is approximately 44 K over the Yellow Sea. As a result of data assimilation, negative increment of EPT appears over the areas north of 37°N, and positive increment of EPT appears south of 37°N. This change in EPT field is related to an increase of baroclinic instability over the areas upstream of the Korean Peninsula, and it also corrects the location of surface boundary for TL/AS-type MCS development. It is also noted that increment of water vapor mixing ratio is greater than that of temperature. In ASDA experiment, meridional gradient of EPT over the Yellow Sea is increased to approximately 16 K although the gradient is not as large as that in 4DVAR experiment. Unlike 4DVAR experiment, positive increment of EPT appears over the continental areas north

of 37°N. This may be partly related to overestimation of rainfall in ASDA experiment during the early period of forecast. Consequently, via the data assimilation, EPT gradient is modified in 4DVAR and ASDA experiments, and this modification improves rainfall forecast related to TL/AS-type MCS.

Analysis increments of 850-hPa wind vector and wind speed for 4DVAR and ASDA experiments are shown in Fig. 5.16 with the corresponding analysis fields. In 4DVAR experiment, incremental wind is anti-cyclonic over the Korean Peninsula and it is cyclonic over the Yellow Sea. This feature is also found in ASDA experiment although anti-cyclonic incremental wind is not dramatic compared to 4DVAR experiment. Due to the increment of wind, simulated LLJ in 4DVAR and ASDA experiments is enhanced compared to CONTROL experiment, and this implies that favorable conditions for heavy rainfall are formed in 4DVAR and ASDA experiments.

Finally, analysis increments of Sea Level Pressure (SLP) superimposed on the corresponding analysis fields for 4DVAR and ASDA experiments are shown in Fig. 5.17. Both in 4DVAR and ASDA experiments, positive increment of SLP appears over the southeastern part of the Korean Peninsula and negative increment appears over the Yellow Sea. Due to the increment of SLP, low-level trough is created over the Yellow Sea, and pressure gradient over the Yellow

Sea, which is related to the intensity of LLJ, is increased in 4DVAR and ASDA experiments.

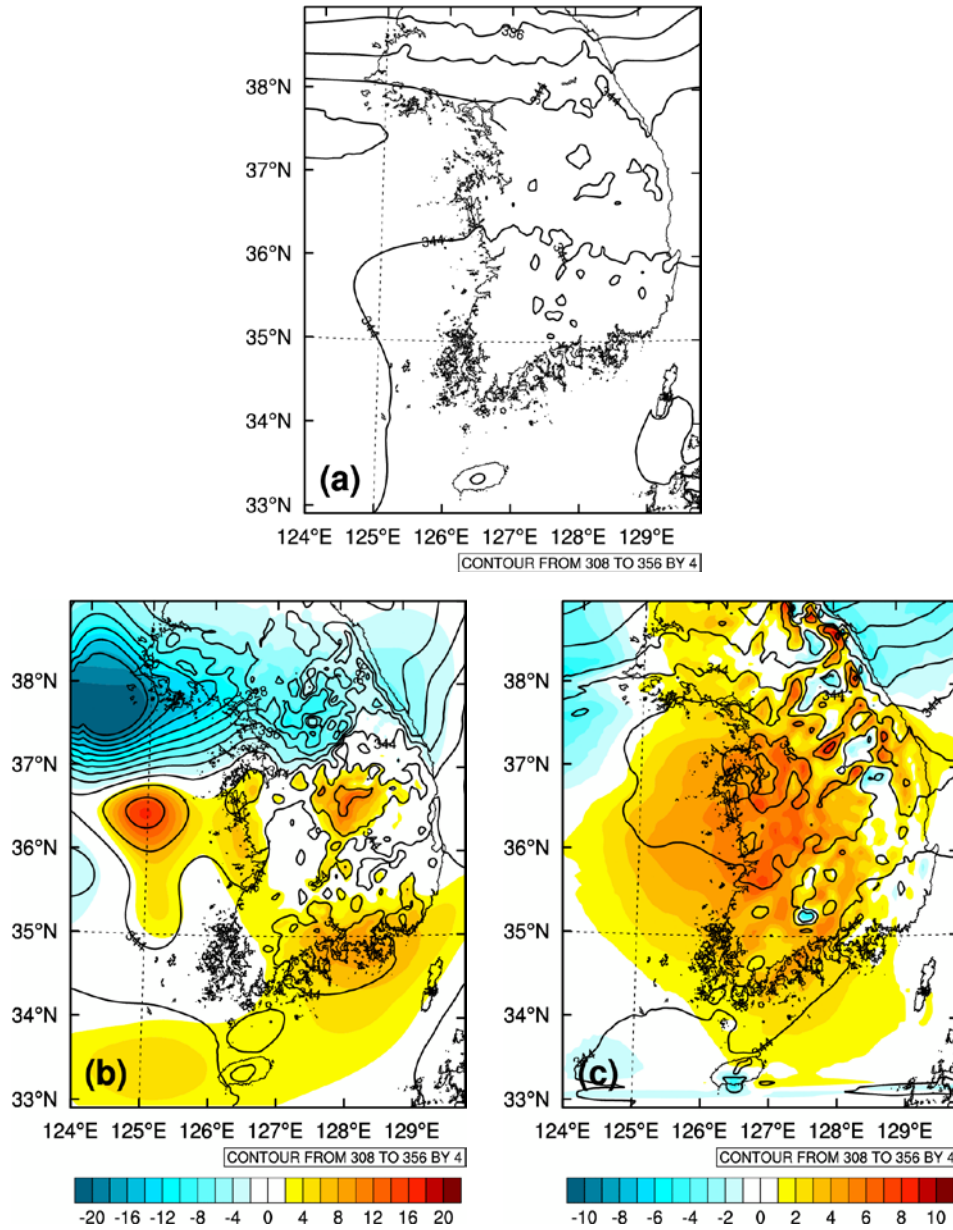


Figure 5.15. Horizontal distributions of 850-hPa equivalent potential temperature (contour interval of 4 K) at 1800 UTC 26 July 2006 for (a) CONTROL, (b) 4DVAR, and (c) ASDA experiments. In case of data assimilation experiments, analysis increments of equivalent potential temperature (shaded, K) are also shown.

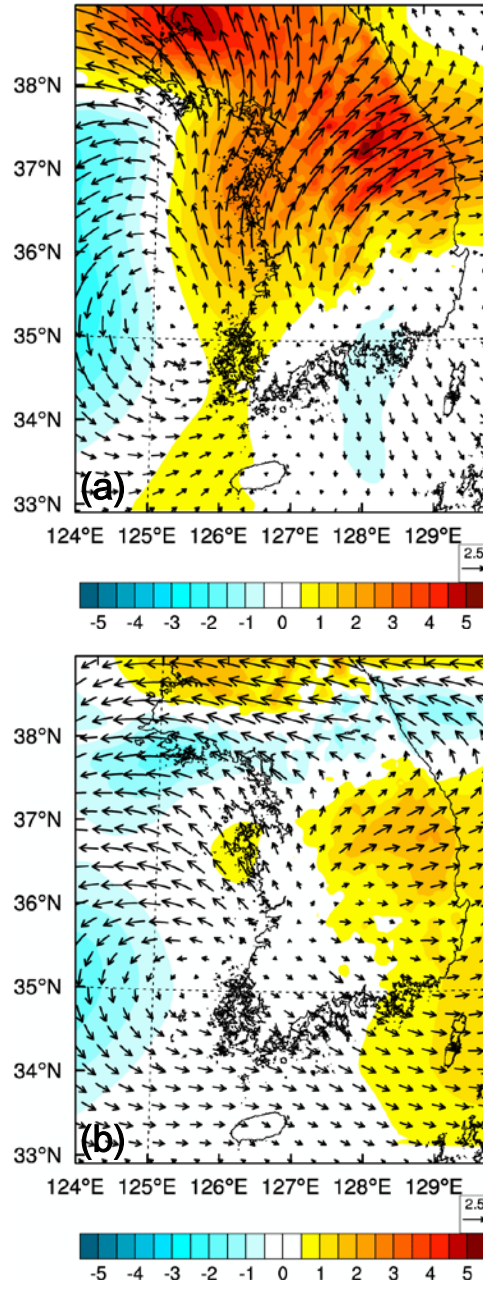


Figure 5.16. 850-hPa analysis increment of wind vector and speed (shaded, m s^{-1}) for (a) 4DVAR and (b) ASDA experiments.

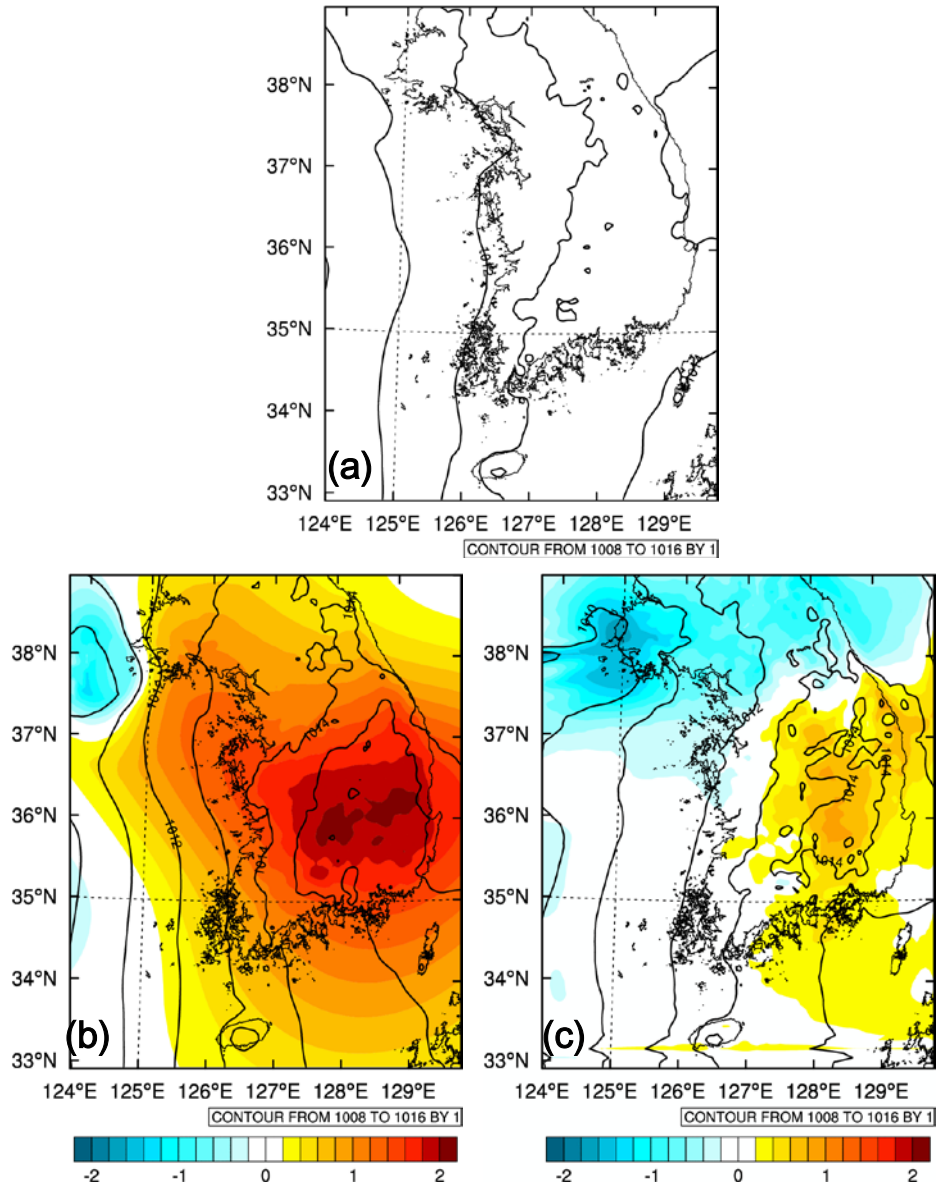


Figure 5.17. Horizontal distributions of Sea Level Pressure (SLP, contour interval of 1 hPa) at 1800 UTC 26 July 2006 for (a) CONTROL, (b) 4DVAR, and (c) ASDA experiments. In case of data assimilation experiments, analysis increments of SLP (shaded, hPa) are superimposed on the corresponding analysis fields.

Figure 5.18 shows simulated reflectivity at 4-km level for 0300, 0600, 0900, and 1200 UTC 27 July 2006. Reflectivities of CONTROL, 4DVAR, and ASDA experiments can be compared to the observations shown in Fig. 5.3. At 0300 UTC 27 July 2006, when the MCS affecting the Korean Peninsula had the characteristics of TL/AS-type, convective rainfall was observed over the cool side of the boundary, which was distinguished by large EPT-gradient, and stratiform rainfall was adjacent to the region of convective rainfall in the observations. In 4DVAR and ASDA experiments, convective rainfall and stratiform rainfall are simulated appropriately while they are shifted northward in CONTROL experiment. At 0600 UTC 27, when the MCS affecting the Korean Peninsula had the characteristics of BB-type, convective cells were formed over the west coast of the Korean Peninsula and they moved northeastward slowly in the observations. In CONTROL experiment, rainfall distribution is shifted northward compared to the observations. In 4DVAR and ASDA experiments, it is located over the central part of the Korean Peninsula like the observations although rainfall band is not tilted in the southwest-northeast direction. At 0900 and 1200 UTC, convective cells continuously passed Seoul in the observations. In 4DVAR and ASDA experiments, convective rainfall related to BB-type MCS is simulated well. Even in

CONTROL experiment, simulated reflectivity is not much different from the observations although it is overestimated over the east coast of the Korean Peninsula due to the fast movement of the simulated MCS.

Figure 5.19 shows horizontal distributions of 500-hPa absolute vorticity and vertical wind shear vector between 500 hPa and 800 hPa at 0600 UTC 27 July 2006 for CONTROL, 4DVAR, and ASDA experiments. As explained in section 5.1, the interaction between MCV and vertical wind shear destabilizes the atmosphere by lifting conditionally-unstable air to its saturation level. In CONTROL experiment, until 0600 UTC 27 July 2006, rainfall is mainly concentrated over the areas north of 38°N, where transport of warm and moist air by LLJ is not significant, and hence MCV related to rainfall is also distributed over those areas. This northward-shifted rainfall band in CONTROL experiment contributes to failure of simulating BB-type MCS and finally, it results in northeastward-shifted 18-h accumulated rainfall distribution. However, in 4DVAR and ASDA experiments, movement of rainfall band from 1800 UTC 26 to 0600 UTC 27 July 2006 is appropriately simulated as in the observations. MCV related to prior rainfall interacts with vertical wind shear over the central part of the Korean Peninsula. As a result of this interaction, warm and moist air transported by LLJ is lifted, and the atmosphere is destabilized. Consequently,

in 4DVAR and ASDA experiments, conditions for development of BB-type MCS are met, and simulated rainfall is concentrated over the localized areas after 0600 UTC 27 July 2006 due to the stationarity of BB-type MCS.

Simulated hodographs of Osan (one of radiosonde observation sites in South Korea) at 0600 UTC 27 July 2006 for 4DVAR and ASDA experiments are shown in Figs. 5.20a and b. Like the observations (Fig. 5.5a), simulated hodograph is hairpin-shaped, and this implies that wind shear vector reverses its direction with height. This reversal in the wind shear can be also found in simulated skew T-log p diagrams of Osan at 0600 UTC 27 July 2006 for 4DVAR and ASDA experiments (Figs. 5.20c and d). Winds at mid-levels are weaker than at lower levels. Interaction between this wind shear and MCV destabilizes the atmosphere, and finally, it results in Moist Absolutely Unstable Layer (MAUL; Bryan and Fritsch, 2000; Bryan et al., 2007) between 500 hPa and 700 hPa, where isotherms nearly coincide with isolines of dew-point temperature in simulated skew T-log p diagram. The MAUL is often observed in the developing stage of many MCSs and it lasts throughout their mature stage. Vertical structures related to BB-type MCS (e.g., vertical wind shear, MAUL) are well simulated in 4DVAR and ASDA experiments compared to the observations.

Figure 5.21 shows vertical cross sectional areas of vertical wind and relative humidity along the line shown in Figs. 5.19b and c for 4DVAR and ASDA experiments. In 4DVAR experiment, updrafts related to convective cells are maximized at mid-levels and they are extended to upper troposphere, even to tropopause-level. Maximum value of updraft is approximately 2 m s^{-1} , and compensating downdrafts are located between neighboring updrafts. Relative humidity below 6-km level is greater than 95%, and it is almost 100% (i.e., saturated) over the updraft regions. Due to the high relative humidity over the rainfall regions, there is no evaporative cooling and the corresponding cold pool. This is consistent with the observations shown in Fig. 5.6. These characteristics of vertical wind and relative humidity shown in 4DVAR experiment are also observed in ASDA experiment.

Consequently, in terms of both rainfall forecast and meteorological-field forecast, 4DVAR and ASDA experiments are superior to CONTROL or 3DVAR experiment. However, it should be noted that computational cost of 4DVAR experiment is much greater than that of 3DVAR experiment. As a reference to computational cost, detailed running time on Linux cluster with 8 CPUs and 8-GB memory is given here. One-iteration for minimization of cost function in 4DVAR experiment takes about 0.5-h wall clock time (i.e., ~24-h for 48-

iteration 4D-Var analysis). In contrast, several tens of iterations in 3DVAR experiment takes about less than 5 minutes on the same machine. One-iteration for minimization of cost function in 4DVAR experiment includes runs of nonlinear, tangent linear, and adjoint models, and hence computational cost of 4DVAR experiment is much greater than 3DVAR experiment. Total computational cost of ASDA experiment is approximately less than one hour because the ASDA method does not require iterative minimization of cost function.

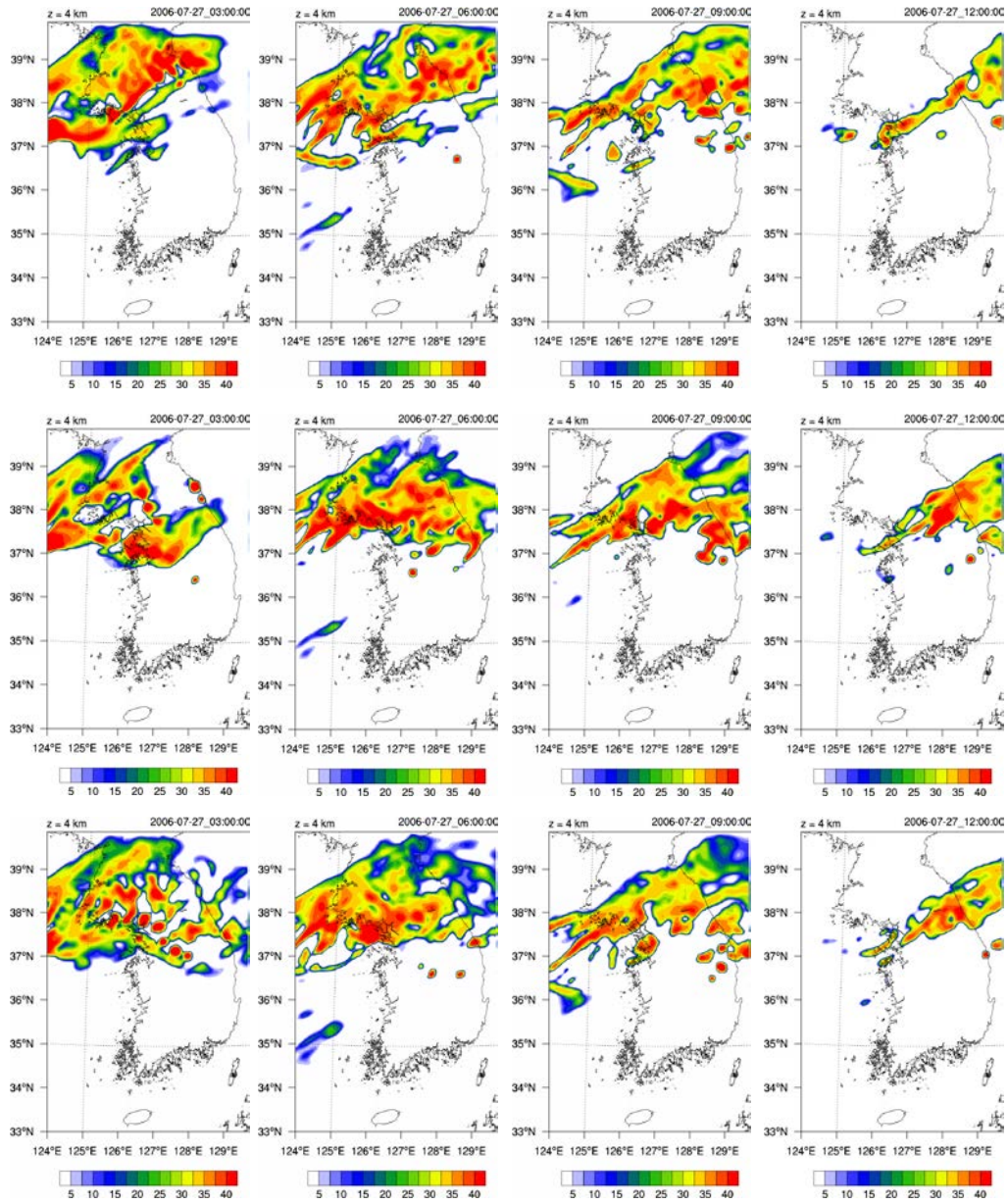


Figure 5.18. Radar reflectivities (dBZ) of 4-km height from 0300 UTC to 1200 UTC 27 July 2006 with 3-hour interval for CONTROL (top), 4DVAR (middle), and ASDA (bottom) experiments.

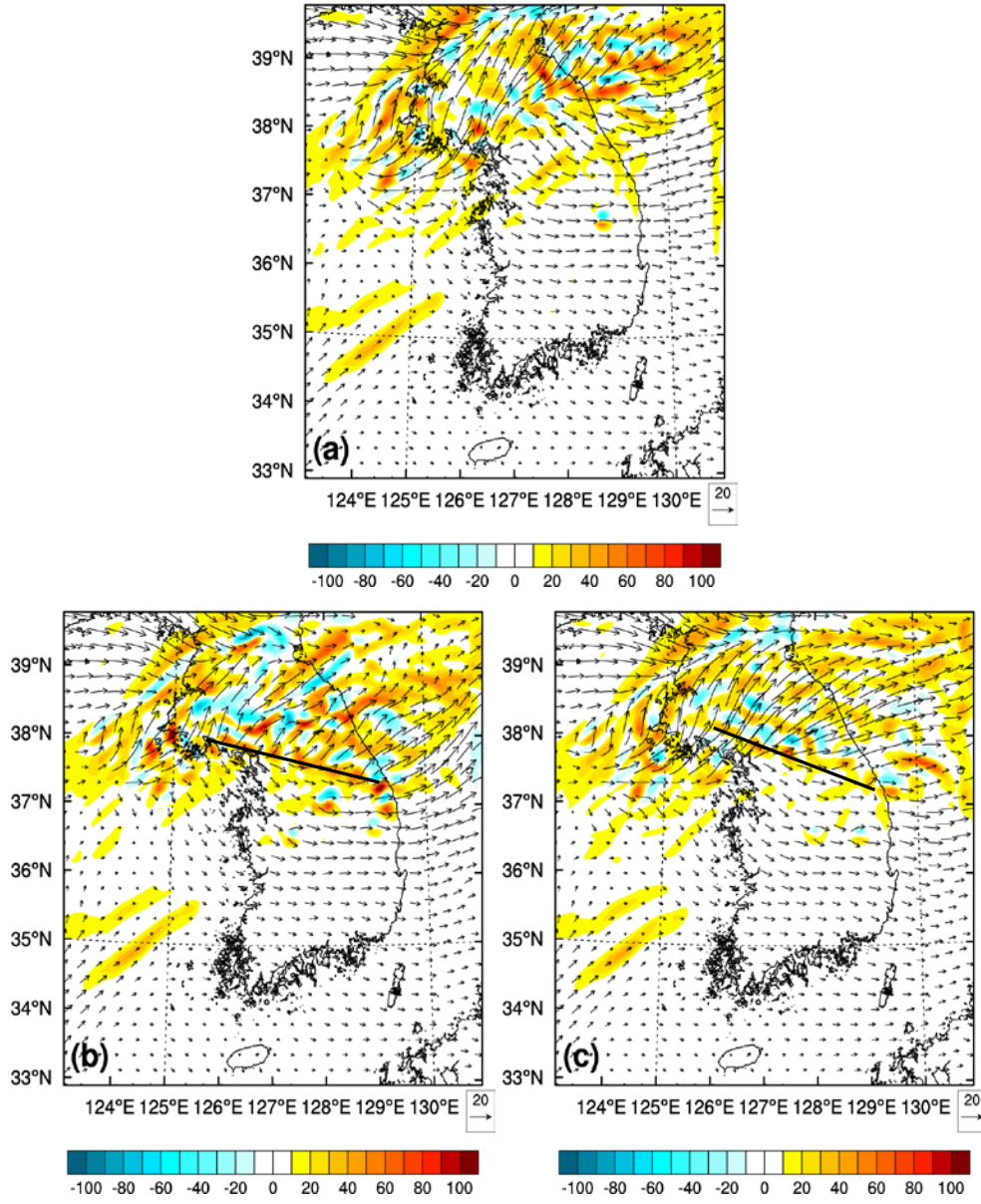


Figure 5.19. Horizontal distributions of 500-hPa absolute vorticity (shaded, 10^{-5} s^{-1}) and vertical wind shear vector between 500 hPa and 800 hPa ($\text{m s}^{-1} \text{ hPa}^{-1}$) at 0600 UTC 27 July 2006 for (a) CONTROL, (b) 4DVAR, and (c) ASDA experiments.

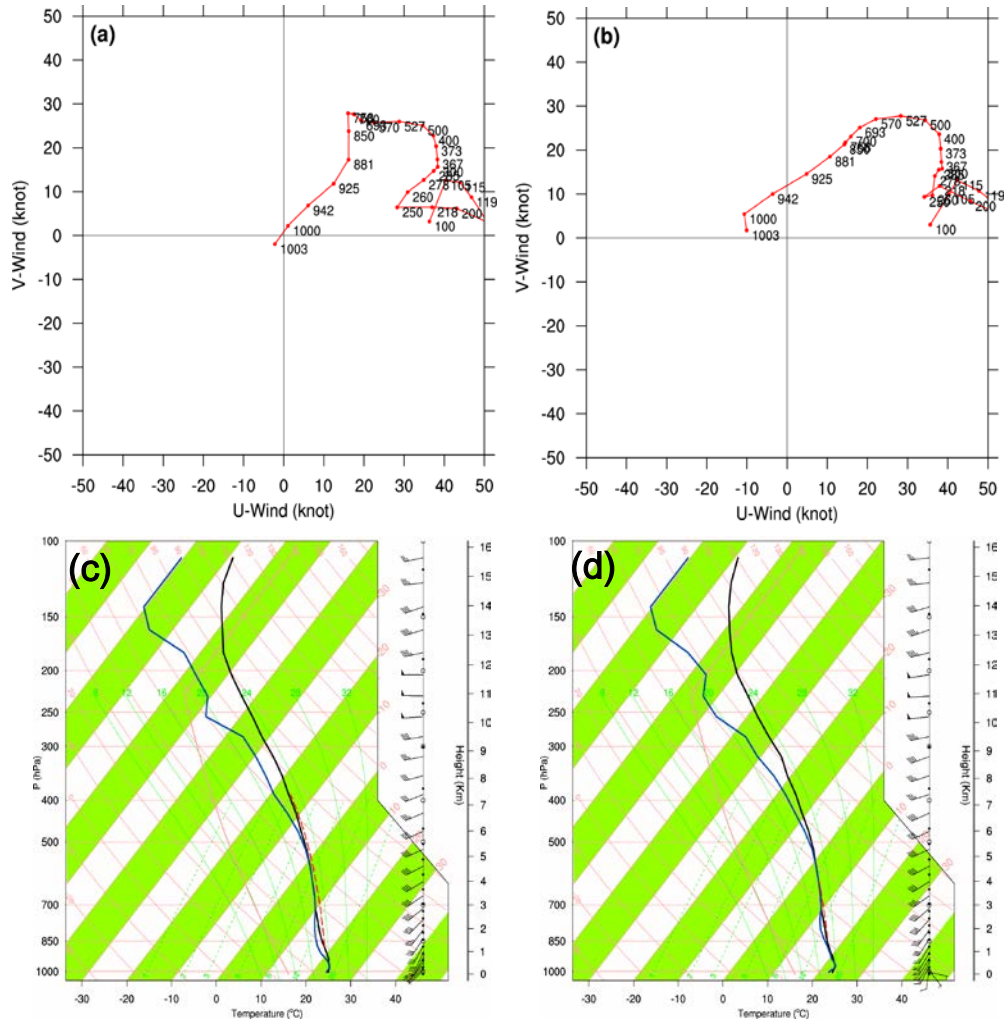


Figure 5.20. Simulated hodographs of Osan at 0600 UTC 27 July 2006 for (a) 4DVAR and (b) ASDA experiments. Simulated skew T-log p diagrams of Osan at 0600 UTC 27 July 2006 for (c) 4DVAR and (d) ASDA experiments.

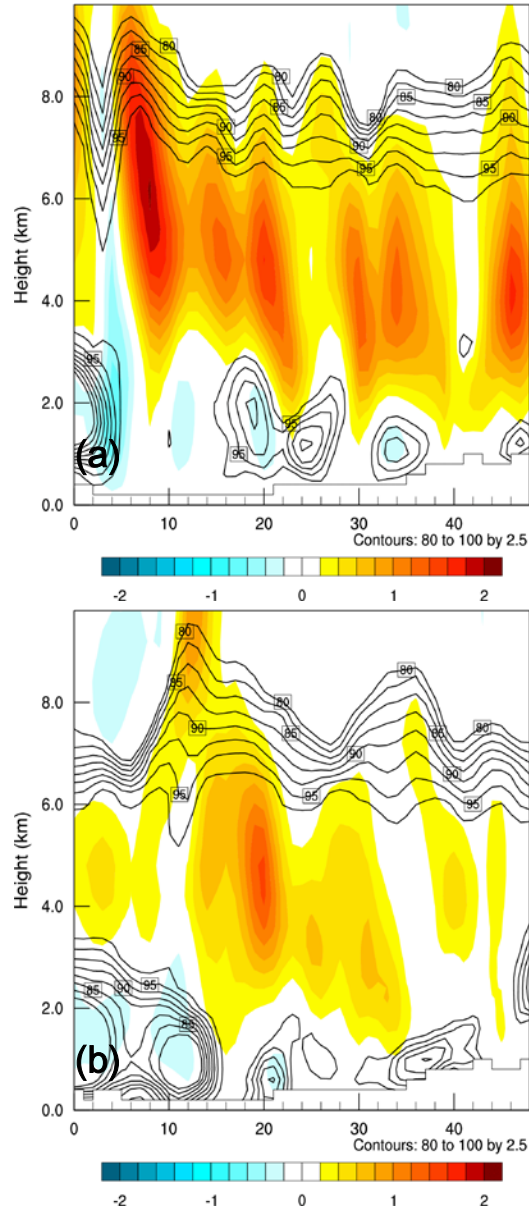


Figure 5.21. Vertical cross sections of vertical wind (shaded, m s^{-1}) and relative humidity (contour interval of 2.5%) along the line shown in Figs. 5.19b and c at 0600 UTC 27 July 2006 for (a) 4DVAR and (b) ASDA experiments.

Chapter 6. Summary and conclusion

The heavy rainfall case selected in the first part of this study is characterized by two localized rainfall maxima over the southwestern part and east coast of the Korean Peninsula. This rainfall was caused by an air-mass thunderstorm related to daytime surface heating. The atmosphere over the southwestern part and the east coast of the Korean Peninsula was convectively unstable with a large CAPE value, and lower-level convergence acted as a lift forcing. When no radar data are assimilated (CONTROL experiment), or when radar data are assimilated using the 3D-Var method (3DVAR experiment), neither of the two localized rainfall maxima is simulated accurately.

By using the 4D-Var method, the simulated rainfall over the southwestern part of the Korean Peninsula is partially improved compared to the CONTROL or 3DVAR experiment. In order to obtain further improvements to the rainfall forecast, more-than-one outer loops (OUTER experiment) and the QSVA method (QSVA experiment) are used. In the QSVA experiment, the length of the assimilation window is increased gradually, and the starting point of the current minimization task comes from the minimizer of the previous minimization task.

The minimization of the cost function in the 4DVAR, OUTER, and QSVA experiments converges successfully after several iterations. The ending value of the cost function and RMSE of O-A for the OUTER and QSVA experiments are smaller than those for the 4DVAR experiment. This implies that the analysis of the OUTER and QSVA experiments is closer to the observations than that of the 4DVAR experiment. RMSE of O-B and RMSD of analysis increment for the OUTER and QSVA experiments are less than those for the 4DVAR experiment, and hence the improved analysis of the OUTER and QSVA experiments is due to a better background estimate of those experiments. Moreover, additional observations, which are rejected in the 4DVAR experiment, get into the assimilation in the OUTER and QSVA experiments although the increase in the number of assimilated observations is not large.

The gap between nonlinear and linear growth (or the nonlinearity of the original minimization problem) is investigated using two measures, namely, the percentage error in linearization and the pattern correlation. In terms of both the percentage error in linearization and pattern correlation, the gap between nonlinear and linear growth is reduced in the OUTER and QSVA experiments compared to the 4DVAR experiment. This is because the background estimate and nonlinear model trajectory are updated progressively in the OUTER and

QSVA experiments. It should also be noted that the nonlinearity of the nonlinear minimization problem is increased with increasing length of the assimilation window in the minimization tasks of the QSVA experiment.

In the CONTROL and 3DVAR experiments, no organized rainfall is simulated although the atmosphere over the southwestern part of the Korean Peninsula is simulated to be conditionally unstable. Incremental wind in the 4DVAR experiment is cyclonic and convergent over the southwestern part of the Korean Peninsula, which acts as a lift forcing, and this modification to the wind field leads to an improved rainfall forecast in the 4DVAR experiment compared to the CONTROL or 3DVAR experiment. However, the 6-h accumulated rainfall amount over the southwestern part of the Korean Peninsula is overestimated, and the rainfall distribution extends wrongly to the central part of South Korea in the 4DVAR experiment. The simulated rainfall in the OUTER experiment is similar to that in the 4DVAR experiment except for more excessive rainfall amount. In the QSVA experiment, the analysis increment of CAPE is negative (positive) over the western part (east coast) of the Korean Peninsula, which results in a better rainfall forecast than in the 4DVAR and OUTER experiments. Besides rainfall forecast, forecasts of other meteorological fields such as wind, temperature, and water vapor mixing ratio are improved in the QSVA

experiment. Analyses of both the OUTER and QSVA experiments are improved compared to that of the 4DVAR experiment, but the rainfall forecast of only the QSVA experiment is improved. In the QSVA experiment, the nonlinearity of the original minimization problem is increased gradually with increasing length of the assimilation window. This quasi-static adjustment guarantees that the computed minimum at the current minimization is the global minimum (or close to the global minimum) and the starting point for the next minimization lies within the basin of the global minimum.

Consequently, the quality of the analysis is improved in the OUTER and QSVA experiments compared to the 4DVAR experiment owing to the nonlinear model trajectory and background estimate being updated. However, the rainfall forecast is improved only in the QSVA experiment due to modifications in the analysis. The quasi-static adjustment of the QSVA method leads to a better analysis in spite of the high degree of nonlinearity of this heavy rainfall case. In addition, the computational cost of the QSVA method is much smaller than that of using multiple outer loops, and it can be further reduced through the use of a loose stopping criterion for the inner-loop minimization. The conclusion from one heavy rainfall case (Case 4) is convinced by analyzing the results of 9 additional heavy rainfall cases over the Korean Peninsula. Quality of the

analysis can be improved through the use of outer-loop or QSVA method compared to 4D-Var method. Especially, the QSVA method is more effective than the outer-loop method when the nonlinearity of the minimization problem is relatively large. It is expected that the QSVA method will be more effective when the length of the assimilation window is increased and the nonlinearity of the minimization problem is increased accordingly.

In the second part of this study, a heavy rainfall case over the Korean Peninsula, which occurred on 1800 UTC 26 July 2006, is selected. This case caused torrential rainfall over the central part of the Korean Peninsula. 18-h accumulated rainfall amount at Seoul and Hongcheon was 187.5 mm and 189.0 mm, respectively. Synoptic environments related to the case were favorable for the development of MCSs. At lower levels, warm and moist air was transported to the Korean Peninsula by southerly or southwesterly flow (i.e., LLJ), and this made the atmosphere over the Korean Peninsula conditionally unstable. In addition, low-level convergence related to LLJ provided consistent forcing for lift. Upper-level divergence related to ULJ coincided with the low-level convergence, and this was responsible for upward motion over the Korean Peninsula.

The MCS related to the heavy rainfall can be classified as TL/AS-type for the

period of 1800 UTC 26 to 0600 UTC 27 and BB-type for the period after 0600 UTC 27 July 2006 based on the morphological analyses of radar reflectivity. Prolonged heavy convective rainfall was observed along the surface boundary, which was defined by large EPT gradient, and stratiform rainfall was adjacent to the region of convective rainfall during the TL/AS-type MCS period. MCV induced by prior rainfall interacted with vertical wind shear, and this interaction destabilized the atmosphere over the Korean Peninsula by lifting conditionally-unstable air to its saturation level during the BB-type MCS period.

The ASDA method is proposed to evade high computational cost of 4D-Var method, retaining the advantages of 4D-Var method such as flow-dependency and balanced-analysis. In the ASDA method, forecast error is defined as the difference between the forecast from the original analysis and the verifying 3D-Var analysis at the forecast time, and adjoint model is run backwards with the forecast-error gradient as an input. The adjoint sensitivity of forecast error to initial condition is scaled by an optimal scaling factor. The optimal scaling factor is determined by minimizing observational cost function of 4D-Var method, and the scaled sensitivity is added to the original first guess. Finally, an improved analysis is made by carrying out 3D-Var with the improved first guess and the observations at the analysis time.

The simulated rainfall distribution is shifted northeastward compared to the observations when no radar data are assimilated (i.e., CONTROL experiment), or radar data are assimilated using 3D-Var method (i.e., 3DVAR experiment). The rainfall distribution and time series of rainfall are similar to the observations when radar data are assimilated using 4D-Var method (i.e., 4DVAR experiment) or ASDA method (i.e., ASDA experiment). Quantitative Precipitation Forecast (QPF) skill is also improved in 4DVAR and ASDA experiments compared to CONTROL and 3DVAR experiments according to the analyses of TS, BS, and RMSE of rainfall. Simulated atmospheric fields such as zonal wind, meridional wind, temperature, and water vapor mixing ratio are verified against re-analysis data (FNL data) and the observational data. When forecasts are verified against FNL data, at the analysis time, RMSEs of 4DVAR and ASDA experiments are greater than those of CONTROL and 3DVAR experiments. Initial conditions (analyses) of 4DVAR and ASDA experiments are modified through the assimilation of radar data while those of CONTROL and 3DVAR experiments are nearly based on FNL data. Except for the analysis time, RMSEs of 4DVAR and ASDA experiments are smaller than those of CONTROL and 3DVAR experiments. When forecasts are verified against the observational data like sounding data or radar radial velocity data, fits to the

observations or RMSEs of 4DVAR and ASDA experiments are better than CONTROL and 3DVAR experiments.

Analysis increments of 4DVAR and ASDA experiments are investigated to find out the reason for the improved forecasts in these experiments. Negative increments of EPT, especially of water vapor mixing ratio over the Yellow Sea enhance meridional gradient of EPT in 4DVAR and ASDA experiments, and this corrects the location of the surface boundary, distinguished by large EPT-gradient, related to TL/AS-type MCS. Incremental wind of 4DVAR and ASDA experiments are anti-cyclonic over the Korean Peninsula and they are cyclonic over the Yellow Sea. This implies strengthening of LLJ transporting warm and moist air to the Korean Peninsula. Due to the improvement of the analysis, subsequent forecasts appropriately simulate the observed features of TL/AS- and BB-type MCSs and the corresponding rainfall in 4DVAR and ASDA experiments. In CONTROL experiment, simulated rainfall related to TL/AS-type MCS is displaced northeastward compared to the observations. The interaction between MCV induced by prior rainfall and vertical wind shear occurs over the northern part of the Korean Peninsula, where transport of warm and moist air is not active. Therefore, rainfall related to BB-type MCS is not simulated well in CONTROL experiment. However, in 4DVAR and ASDA

experiments, rainfall related to TL/AS-type MCS is properly simulated, and finally, rainfall related to BB-type MCS is also simulated well. In detail, MCV interacts with vertical wind shear over the central part of the Korean Peninsula, and this interaction results in MAUL and upward motion related to the heavy rainfall.

In conclusion, the heavy rainfall affecting the Korean Peninsula is not simulated appropriately when radar data are assimilated using 3D-Var method. Forecasts from 4D-Var analysis are similar to the observations, but computational cost of the 4D-Var method is very high (due to iterative minimization) compared to the 3D-Var method. Forecasts based on the proposed ASDA method are also similar to the observations, and the characteristics of TL/AS- and BB-type MCSs are properly simulated. It should be noted that computational cost of the ASDA method is relatively low (one adjoint-model run, two 3D-Var analyses, scaling-factor determination), and the first-guess and observations errors are not correlated with each other. The ASDA method will be applied to a variety of cases over the Korean Peninsula and statistical analysis will be conducted to get robustness of the method.

References

- Astling, E. G., J. Paegle, E. Miller, and C. J. O'Brien, 1985: Boundary layer control of nocturnal convection associated with a synoptic-scale system. *Mon. Wea. Rev.*, **113**, 540-552.
- Barker, D. M., W. Huang, Y.-R. Guo, A. J. Bourgeois, and Q. N. Xiao, 2004: A three-dimensional variational data assimilation system for MM5: Implementation and initial results. *Mon. Wea. Rev.*, **132**, 897-914.
- Bjerknes, V., 1904: Das Problem der Wettervorhersage, betrachtet vom Standpunkt der Mechanik und der Physik. *Meteorologische Zeitschrift*, **21**, 1-7.
- Bryan, G. H., and J. M. Fritsch, 2000: Moist absolute instability: The sixth static stability state. *Bull. Amer. Meteor. Soc.*, **81**, 1207-1230.
- Bryan, G. H., R. Rotunno, and J. M. Fritsch, 2007: Roll circulations in the convective region of a simulated squall line. *J. Atmos. Sci.*, **64**, 1249-1266.
- Chen, T.-C., and J. A. Kpaeyeh, 1993: The synoptic-scale environment associated with the low-level jet of the Great Plains. *Mon. Wea. Rev.*, **121**,

416-420.

Courtier, P., J.-N. Thépaut, and A. Hollingsworth, 1994: A strategy for operational implementation of 4D-Var, using an incremental approach. *Quart. J. Roy. Meteor. Soc.*, **120**, 1367-1387.

Daley, R., and Barker, E., 2001: *The NAVDAS Source Book*. NRL/PJ/7530-01-441. Naval Research Laboratory. 163 pp.

Dudhia, J., 1989: Numerical study of convection observed during the winter monsoon experiment using a mesoscale two-dimensional model. *J. Atmos. Sci.*, **46**, 3077-3107.

Evensen, G., 1994: Sequential data assimilation with a nonlinear quasi-geostrophic model using Monte Carlo methods to forecast error statistics. *J. Geophys. Res.*, **99C5**, 10143-10162.

Gandin, L. S., 1963: *Objective analysis of meteorological fields*. Translated from Russian 1965, Israel program for scientific translations.

Gauthier, P., 1992: Chaos and quadri-dimensional data assimilation: a study based on the Lorenz model. *Tellus*, **44A**, 2-17.

Gauthier, P., and J.-N. Thépaut, 2001: Impact of the digital filter as a weak

- constraint in the preoperational 4DVAR assimilation system of Météo France. *Mon. Wea. Rev.*, **129**, 2089-2102.
- Gauthier, P., M. Tanguay, S. Laroche, and S. Pellerin, 2007: Extension of 3DVAR to 4DVAR: Implementation of 4DVAR at the Meteorological Service of Canada. *Mon. Wea. Rev.*, **135**, 2339-2364.
- Grell, G. A., J. Dudhia, and D. Stauffer, 1994: A description of the fifth-generation Penn State/NCAR Mesoscale Model (MM5). NCAR Tech. Note TN-398+STR, 138pp.
- Haben, S. A., A. S. Lawless, and N. K. Nichols, 2011: Conditioning of incremental variational data assimilation, with application to the Met Office system. *Tellus*, **63A**, 782-792.
- Hello, G., F. Lalaurette, and J.-N. Thépaut, 2000: Combined use of sensitivity information and observations to improve meteorological forecasts: A feasibility study applied to the 'Christmas storm' case. *Quart. J. Roy. Meteor. Soc.*, **126**, 621-647.
- Honda, Y., M. Nishijima, K. Koizumi, Y. Ohta, K. Tamiya, T. Kawabata, and T. Tsuyuki, 2005: A pre-operational variational data assimilation system for a

- non-hydrostatic model at the Japan Meteorological Agency: Formulation and preliminary results. *Quart. J. Roy. Meteor. Soc.*, **131**, 3465-3475.
- Hong, S.-Y., and J.-O. Lim, 2006: The WRF single-moment 6-class microphysics scheme (WSM6). *J. Korean Meteor. Soc.*, **42**, 129-151.
- Hong, S.-Y., Y. Noh, and J. Dudhia, 2006: A new vertical diffusion package with an explicit treatment of entrainment processes. *Mon. Wea. Rev.*, **134**, 2318-2341.
- Huang, X.-Y., N. Gustafsson, and E. R. Källén, 1997: Using an adjoint model to improve an optimum interpolation-based data-assimilation system. *Tellus*, **49A**, 161-176.
- Huang, X.-Y., 1999: A generalization of using an adjoint model in intermittent data assimilation system. *Mon. Wea. Rev.*, **127**, 766-787.
- Huang, X.-Y., X. Yang, N. Gustafsson, K. Mogensen, and M. Lindskog, 2002: Four-dimensional variational data assimilation for a limited area model. HIRLAM Tech Rep 57, 41 pp. [Available from SMHI, S-601 76 Norrköping, Sweden.]
- Huang, X.-Y., and co-authors, 2009: Four-dimensional variational data

- assimilation for WRF: Formulation and preliminary results. *Mon. Wea. Rev.*, **137**, 299-314.
- Isaksen, L., M. Fisher, E. Andersson, and J. Barkmeijer, 2005: The structure and realism of sensitivity perturbations and their interpretation as 'Key Analysis Errors'. *Quart. J. Roy. Meteor. Soc.*, **131**, 3053-3078.
- Järvinen, H., J.-N. Thépaut, and P. Courtier, 1996: Quasi-continuous variational data assimilation. *Quart. J. Roy. Meteor. Soc.*, **122**, 515-534.
- Jiang, X., N.-C. Lau, I. M. Held, and J. J. Ploshay, 2007: Mechanisms of the Great Plain low-level jet as simulated in an AGCM. *J. Atmos. Sci.*, **64**, 532-547.
- Johnson, R. H., 2001: Surface mesohighs and mesolows. *Bull. Amer. Meteor. Soc.*, **82**, 13-31.
- Kain, J. S., 2004: The Kain-Fritsch convective parameterization: An update. *J. Appl. Meteor.*, **43**, 170-181.
- Kalnay, E., S. K. Park, Z.-X. Pu, J. Gao, 2000: Application of the quasi-inverse method to data assimilation. *Mon. Wea. Rev.*, **128**, 864-875.
- Klinker, E., F. Rabier, and R. Gelaro, 1998: Estimation of key analysis errors

- using the adjoint technique. *Quart. J. Roy. Meteor. Soc.*, **124**, 1909-1933.
- Le Dimet, F., and O. Talagrand, 1986: Variational algorithms for analysis and assimilation of meteorological observations: Theoretical aspects. *Tellus*, **38A**, 97-110.
- Lewis, J., and J. Derber, 1985: The use of adjoint equations to solve a variational adjustment problem with advective constraints. *Tellus*, **37A**, 309-327.
- Li, Y., I. M. Navon, W. Yang, X. Zou, J. R. Bates, S. Moorthi, and R. W. Higgins, 1994: Four-dimensional variational data assimilation experiments with a multilevel semi-Lagrangian semi-implicit general circulation model. *Mon. Wea. Rev.*, **122**, 966-983.
- Lorenz, E. N., 1963: Deterministic nonperiodic flow. *J. Atmos. Sci.*, **20**, 130-141.
- Luong, B., J. Blum, and J. Verron, 1998: A variational method for the resolution of a data assimilation problem in oceanography. *Inverse Problems*, **14**, 979-997.
- Maddox, R. A., C. F. Chappell, and L. R. Hoxit, 1979: Synoptic and meso- α

- scale aspects of flash flood events. *Bull. Amer. Meteor. Soc.*, **60**, 115-123.
- McCorcle, M. D., 1988: Simulation of surface-moisture effects on the Great Plain low-level jet. *Mon. Wea. Rev.*, **116**, 1705-1720.
- Miller, L. J., C. G. Mohr, and A. J. Weinheimer, 1986: The simple rectification to Cartesian space of folded radial velocities from Doppler radar sampling. *J. Atmos. Oceanic Technol.*, **3**, 162-174.
- Miller, R. N., M. Ghil, and F. Gauthiez, 1994: Advanced data assimilation in strongly nonlinear dynamical systems. *J. Atmos. Sci.*, **51**, 1037-1056.
- Mlawer, E. J., S. J. Taubman, P. D. Brown, M. J. Iacono, and S. A. Clough, 1997: Radiative transfer for inhomogeneous atmospheres: RRTM, a validated correlated-k model for the longwave. *J. Geophys. Res.*, **102**, 16663-16682.
- Mohr, C. G., and R. L. Vaughan, 1979: An economical procedure for Cartesian interpolation and display of reflectivity data in three dimensional space. *J. Appl. Meteor.*, **18**, 661-670.
- Mohr, C. G., R. L. Vaughan, and H. W. Frank, 1986: The merger of mesoscale datasets into a common Cartesian format for efficient and systematic

- analyses. *J. Atmos. Oceanic Technol.*, **3**, 144-161.
- Navon, I. M., X. Zou, J. Derber, and J. Sela, 1992: Variational data assimilation with an adiabatic version of the NMC spectral model. *Mon. Wea. Rev.*, **120**, 1433-1446.
- Park, S.-G., and D.-K. Lee, 2009: Retrieval of high-resolution wind fields over the Southern Korean Peninsula using the Doppler weather radar network. *Wea. Forecasting*, **24**, 87-103.
- Park, S. K., and D. Županski, 2003: Four-dimensional variational data assimilation for mesoscale and storm-scale applications. *Meteorol. Atmos. Phys.*, **82**, 173-208.
- Par, S. K., and E. Kalnay, 2004: Inverse three-dimensional variational data assimilation for an advection-diffusion problem: Impact of diffusion and hybrid application. *Geophys. Res. Lett.*, **31**, L04102.
- Parrish, D. F., and J. Derber, 1992: The National Meteorological Center's spectral statistical-interpolation analysis system. *Mon. Wea. Rev.*, **120**, 1747-1763.
- Pires, C., R. Vautard, and O. Talagrand, 1996: On extending the limits of

- variational assimilation in nonlinear chaotic systems. *Tellus*, **48A**, 96-121.
- Pu, Z.-X., E. Kalnay, J. C. Derber, and J. G. Sela, 1997: Using forecast sensitivity patterns to improve future forecast skill. *Quart. J. Roy. Meteor. Soc.*, **123**, 1035-1053.
- Rabier, F., and P. Courtier, 1992: Four-dimensional assimilation in the presence of baroclinic instability. *Quart. J. Roy. Meteor. Soc.*, **118**, 649-672.
- Rabier, F., E. Klinker, P. Courtier, and A. Hollingsworth, 1996: Sensitivity of forecast errors to initial conditions. *Quart. J. Roy. Meteor. Soc.*, **122**, 121-150.
- Rabier, F., J.-N. Thépaut, and P. Courtier, 1998: Extended assimilation and forecast experiments with a four-dimensional variational assimilation system. *Quart. J. Roy. Meteor. Soc.*, **124**, 1861-1887.
- Rabier, F., H. Järvinen, E. Klinker, J.-F. Mahfouf, and A. Simmons, 2000: The ECMWF operational implementation of four-dimensional variational assimilation. Experimental results with simplified physics. *Quart. J. Roy. Meteor. Soc.*, **126**, 1143-1170.
- Rawlins, F., S. P. Ballard, K. J. Bovis, A. M. Clayton, D. Li, G. W. Inverarity, A.

- C. Lorenc, and T. J. Payne, 2007: The Met Office global 4-Dimensional data assimilation system. *Quart. J. Roy. Meteor. Soc.*, **133**, 347-362.
- Rizvi, S. R. H., Y.-R. Guo, H. Shao, M. Demirtas, and X.-Y. Huang, 2008: Impact of outer loop for WRF data assimilation system (WRFDA). Proceedings, *The 9th WRF Users' Workshop*, Boulder, Colorado.
- Rotunno, R., J. B. Klemp, and M. L. Weisman, 1988: A theory for strong, long-lived squall lines. *J. Atmos. Sci.*, **45**, 463-485.
- Schumacher, R. S., and R. H. Johnson, 2005: Organization and environmental properties of extreme-rain-producing mesoscale convective systems. *Mon. Wea. Rev.*, **133**, 961-976.
- Schumacher, R. S., and R. H. Johnson, 2008: Mesoscale processes contributing to extreme rainfall in a midlatitude warm-season flash flood. *Mon. Wea. Rev.*, **136**, 3964-3986.
- Schumacher, R. S., and R. H. Johnson, 2009: Quasi-stationary, extreme-rain-producing convective systems associated with midlevel cyclonic circulation. *Wea. Forecasting*, **24**, 555-574.
- Skamarock, W. C., J. B. Klemp, J. Dudhia, D. O. Gill, D. M. Barker, M. Duda,

- X.-Y. Huang, W. Wang, and J. G. Powers, 2008: *A description of the Advanced Research WRF version 3*. NCAR Tech. Note TN-475+STR, 113 pp.
- Sneider, R., 1998: The role of nonlinearity in inverse problems. *Inverse Probl.*, **14**, 387-404.
- Song, H.-J., G.-H. Lim, D.-I. Lee, and H.-S. Lee, 2009: Comparison of retrospective optimal interpolation with four-dimensional variational assimilation. *Tellus*, **61A**, 428-437.
- Stensrud, D. J., and J.-W. Bao, 1992: Behaviors of variational and nudging assimilation techniques with a chaotic low-order model. *Mon. Wea. Rev.*, **120**, 3016-3028.
- Sun, J., 2005: Convective-scale assimilation of radar data: Progress and challenges. *Quart. J. Roy. Meteor. Soc.*, **131**, 3439-3463.
- Swanson, K., and R. Vautard, 1998: Four-dimensional variational assimilation and predictability in a quasi-geostrophic model. *Tellus*, **50A**, 369-390.
- Talagrand, O., 1997: Assimilation of observations, an introduction, *J. Met. Soc. Japan*, **75**, 191-209.

- Tanguay, M., P. Bartello, and P. Gauthier, 1995: Four-dimensional data assimilation with a wide range of scales. *Tellus*, **47A**, 974-997.
- Thépaut, J.-N., and P. Courtier, 1991: Four-dimensional variational data assimilation using the adjoint of a multilevel primitive-equation model. *Quart. J. Roy. Meteor. Soc.*, **117**, 1225-1254.
- Trémolet, Y., 2004: Diagnostics of linear and incremental approximations in 4D-Var. *Quart. J. Roy. Meteor. Soc.*, **130**, 2233-2251.
- Wang, H., J. Sun, X. Zhang, X.-Y. Huang, and T. Auligné, 2013: Radar data assimilation with WRF 4D-Var: Part I. System development and preliminary testing. *Mon. Wea. Rev.*, in press.
- Xiao, Q., Y.-H. Kuo, J. Sun, W.-C. Lee, E. Lim, Y.-R. Guo, and D. M. Barker, 2005: Assimilation of Doppler radar observations with a regional 3DVAR system: Impact of Doppler velocities on forecasts of a heavy rainfall case. *J. Appl. Meteor.*, **44**, 768-788.
- Xiao, Q., and J. Sun, 2007: Multiple-radar data assimilation and short-range quantitative precipitation forecasting of a squall line observed during IHOP_2002. *Mon. Wea. Rev.*, **135**, 3381-3404.

Xiao, Q., Y.-H. Kuo, J. Sun, W.-C. Lee, D. M. Barker, and E. Lim, 2007: An approach of radar reflectivity data assimilation and its assessment with the inland QPF of typhoon Rusa (2002) at landfall. *J. Appl. Meteor. Climatol.*, **46**, 14-22.

Xu, L., T. Rosmond, and R. Daley, 2005: Development of NAVDAS-AR: Formulation and initial tests for the linear problem. *Tellus*, **57A**, 546-559.

국문 초록

논문의 첫 번째 부분에서는 한반도에서 발생한, 두 개의 국지적인 강수 구역을 갖는 집중호우 사례를 선택하였다. 선택된 사례는 낮 시간대 지표면의 가열로 인해 발달한 뇌우에 의해 강수가 야기된 사례이다. 한반도 남서 지역과 동해안 지역은 대류 잠재 불안정 에너지의 값이 크게 나타나는 등 대류 불안정 상태에 놓여 있었고, 같은 지역에서 나타난 하층 수렴은 상승 운동에 기여하였다. 레이더 자료를 동화하지 않거나, 레이더 자료를 3차원 변분 자료 동화 방법을 이용하여 동화한 경우, 2개의 강수 구역 모두 제대로 모의되지 않았다. 4차원 변분 자료 동화 방법으로 레이더 자료를 동화한 경우, 한반도 남서쪽의 강수 구역이 일부 모의되었다. 강수 모의를 개선하기 위하여, 레이더 자료 동화 시 outer loop와 QSVA 방법을 사용하였다. QSVA 방법에서는 assimilation window의 길이가 서서히 증가하고, 현재 최소화 문제의 시작점이 이전 최소화 문제의 해로부터 온다는 특성이 있다.

4DVAR (4차원 변분 자료 동화 방법 사용), OUTER (outer loop 사용), 그리고 QSVA 실험 (QSVA 방법 사용)에서 다수의 iteration 후에 비용 함수의 최소화 과정이 수렴하였다. OUTER와 QSVA 실험에 대한 최종 비용 함수의 값과 O-A (관측과 분석장의 차)의 근제곱평균오차

값이 4DVAR 실험에 비해 작게 나타났다. 이는 OUTER 실험과 QSVa 실험의 분석장이 4DVAR 실험의 분석장에 비해 관측에 가까운 것을 의미한다. OUTER와 QSVa 실험에 대한 O-B (관측과 배경장의 차)의 근제곱평균오차 값과 분석 증분 (분석장과 배경장의 차)의 근제곱평균 차이 값 역시 4DVAR 실험에 비해 작게 나타났다. 이를 통해 OUTER 실험과 QSVa 실험의 분석장이 개선된 것은 배경장 (정확히는, 배경장에 대한 예측값)이 개선되었기 때문이라 할 수 있다. 나아가, OUTER 실험과 QSVa 실험에서는 4DVAR 실험에서는 사용되지 못한 관측값이 사용되었고, 이는 분석장의 품질 및 예보 오차 감소에 기여할 수 있다.

OUTER 실험과 QSVa 실험에서는 비선형 성장과 선형 성장의 차이, 혹은 최소화 문제의 비선형성이 4DVAR 실험에 비해 줄어든 것을 확인할 수 있었다. 이는 OUTER와 QSVa 실험에서 배경장에 대한 예측값 (혹은 최초 추측값)이 지속적으로 갱신되고, 이에 따라 선형화를 위한 비선형 모형 궤적 또한 지속적으로 갱신되기 때문이다. 특히, QSVa 실험에서는 assimilation window의 길이가 서서히 증가함에 따라 최소화 문제의 비선형성 역시 증가하여 국지적인 최소값이 아닌 절대적인 최소값을 찾는 데 있어 유리한 면이 있다.

4DVAR 혹은 OUTER 실험에서는 바람장에 대한 분석 증분이 한반도 남서쪽에서 저기압성 회전 성분을 갖고, 동시에 수렴하는 특성을 갖는다. 이러한 분석장의 수정을 통해 분석장이 관측과 가까워지고, 결

국 CONTROL 실험 (자료 동화를 수행하지 않은 실험)이나 3DVAR 실험 (3차원 변분 자료 동화 사용)에 비해 향상된 강수 모의 성능을 보이게 되는 것이다. 그렇지만 4DVAR 혹은 OUTER 실험에서는 모의된 강수량이 관측값에 비해 많고, 관측과 달리 한반도 남서쪽의 강수 구역이 한반도 중부 지역까지 확장되어 나타나는 한계를 갖는다. QSVA 실험에서는 대류 잠재 불안정 에너지에 대한 분석 증분이 한반도 남서쪽에서 음의 값으로 나타나 4DVAR 혹은 OUTER 실험에 비해 모의된 강수가 관측에 가깝게 나타난다. 앞에서도 언급했듯이, QSVA 실험에서는 assimilation window의 길이가 서서히 증가함에 따라 풀어야 하는 최소화 문제의 비선형성도 서서히 증가하게 된다. 이러한 quasi-static adjustment는 현재 최소화 문제의 해가 절대적인 최소값이고, 동시에 다음 최소화 문제에 대한 시작점이 절대적인 최소값이 속하는 공간 안에 놓여 있음을 보장한다. 또한 QSVA 방법에 대한 계산 비용은 outer loop를 여러 번 사용했을 때에 비해 매우 저렴하며, assimilation window의 길이가 짧은 경우에 대해서는 완화된 계산 기준을 적용함으로써 계산 비용을 더욱 줄이는 것도 가능하다.

QSVA 방법을 한 개의 강수 사례에 적용하여 얻은 결론을 통계적으로 확증하기 위하여 2006년과 2008년 한반도에서 발생한 9개의 집중호우 사례에 추가적으로 QSVA 방법을 적용하였다. 하나의 강수 사례에서와 마찬가지로, 4DVAR 실험에 비해 OUTER 실험과 QSVA 실험에서는 배경장에 대한 예측값, 그리고 분석장이 향상되었다. 향상된

분석장은 강수와 다른 기상 요소의 모의가 관측과 가까워지는 결과를 도출하였다. 특히, QSVA 방법의 경우, 최소화 문제의 비선형성이 상대적으로 클 때 outer loop 방법에 비해 효과적인 것으로 나타났다. 이를 통해 assimilation window의 길이가 길어지거나 수평 해상도가 더 높아질 경우, 최소화 문제의 비선형성이 증가하여 QSVA 방법을 적용하는 것이 유리할 것으로 예상된다.

논문의 두 번째 부분에서는 한반도에서 2006년 7월 26일에 발생한 집중호우 사례를 선택하였다. 이 사례에서는 서울을 중심으로 하는 중부 지방에 많은 양의 강수가 집중되었다. 또한 상·하층 바람장, 온도 및 습도 분포 등 종관적인 배경이 중규모 대류계 발달의 호조건을 제공하고 있었다. 레이더 반사도 이미지의 분석을 통해 2006년 7월 26일 18 UTC부터 27일 06 UTC까지 한반도에 영향을 준 중규모 대류계는 TL/AS 타입으로, 그리고 27일 06 UTC 이후에 영향을 준 중규모 대류계는 BB 타입으로 구분할 수 있다. TL/AS 타입의 중규모 대류계가 영향을 준 시기에는 지표면 경계 (상당 온위의 경도가 큰 지역)의 북쪽 지역에서 대류성 강수가 나타나고 그 인접 지역에서는 층운형 강수가 넓게 나타난다. BB 타입 중규모 대류계의 영향을 받는 시기에는 앞선 강수에 의해 생성된 중규모 대류 와도가 연직 방향의 시어와 상호 작용을 하면서 조건부 불안정한 공기를 상승시켜 불안정한 대기 조건을 생성한다.

4차원 변분 자료 동화 방법의 장점을 최대한 유지하면서 4차원 변분

자료 동화 방법의 계산 비용을 줄이기 위하여 ASDA 방법을 제안하였다. ASDA 방법에서는 예보 오차에 대한 경도를 입력 자료로 수반 모형을 적분하여 예보 오차의 초기 조건에 대한 민감도를 계산한다. 이렇게 계산한 민감도의 크기 및 부호는 최적의 크기 조정 인자에 의해 결정된다. 이 때, 최적의 크기 조정 인자는 4차원 변분 자료 동화 방법의 관측 비용 함수를 최소화하여 얻게 되며, 크기 및 부호가 변경된 민감도는 원래의 (배경장에 대한) 최초 예측값에 더해진다. 마지막으로 향상된 최초 예측값과 분석 시각의 관측값을 이용하여 3차원 변분 자료 동화가 수행된다.

레이더 자료를 동화하지 않았거나, 3차원 변분 자료 동화 방법으로 레이더 자료를 동화한 경우, 모의된 강수 분포는 관측에 비해 북동쪽으로 치우쳐 나타났다. 하지만 4차원 변분 자료 동화 방법 혹은 새롭게 제안된 ASDA 방법을 이용하여 레이더 자료를 동화한 경우, 모의된 강수 분포 및 강수 시계열이 관측과 유사하게 나타났다. 강수 모의뿐만 아니라, 동서 방향의 바람, 남북 방향의 바람, 온도, 수증기 혼합비 등 다른 기상 요소에 대한 모의 성능 역시 4차원 변분 자료 동화 방법이나 ASDA 방법을 사용했을 경우 향상되었다.

4DVAR와 ASDA 실험 (ASDA 방법을 사용)에서는 황해에서의 상당온위의 분석 증분이 양과 음의 값이 남북 방향으로 분포하는 형태를 갖는다. 이로 인해 한반도 서쪽에서의 경압 불안정성이 증가하고, 동시에 TL/AS 타입 중규모 대류계의 발달과 연관이 있는 지표면 경계

의 위치가 변화된다. 결론적으로, 4DVAR와 ASDA 실험에서는 레이더 자료 동화를 통해 분석장이 관측에 가깝게 수정되고, 나아가 TL/AS 그리고 BB 타입 중규모 대류계의 발달과 연관된 강수의 모의가 향상되는 모습을 보인다. 반면 CONTROL 실험에서는 TL/AS 타입의 중규모 대류계와 연관된 강수가 관측에 비해 북쪽으로 치우쳐 나타난다. 이러한 강수에 의해 생성된 중규모 대류성 와도와 연직 바람 시어의 상호작용이 한반도 북쪽에서 나타나면서 BB 타입 중규모 대류계의 발달 및 관련된 강수의 모의가 제대로 이루어지지 않는다. 하지만, 4DVAR와 ASDA 실험에서는 TL/AS 타입의 중규모 대류계에 의한 강수가 관측과 유사하게 모의되면서 이어지는 BB 타입 중규모 대류계에 의한 강수도 관측과 가깝게 모의되었다. 또한 ASDA 방법의 계산 비용은 비슷한 성능 (적어도 한 사례에 대해서는)의 4차원 변분 자료 동화 방법에 비해 크게 적으며, 최초 예측값과 관측 사이의 상관관계가 존재하지 않아 자료 동화의 기본 가정에도 위배되지 않는다.

주요어: 레이더 자료 동화, 집중 호우, 4차원 변분 자료 동화, 수반 모형 민감도, QSVA 방법, ASDA 방법

학번: 2006-30788